THE UNIVERSITY OF CHICAGO

NONEQUILIBRIUM STATISTICAL MECHANICS OF ANOMALOUS TRANSPORT IN CHIRAL ACTIVE SYSTEMS

A DISSERTATION SUBMITTED TO
THE FACULTY OF THE DIVISION OF THE PHYSICAL SCIENCES
IN CANDIDACY FOR THE DEGREE OF
DOCTOR OF PHILOSOPHY

DEPARTMENT OF CHEMISTRY

BY
ZHENGHAN LIAO

CHICAGO, ILLINOIS
MARCH 2020

Dedicated to my family and my ancestors

"The aim of science is not things themselves, as the dogmatists in their simplicity imagine, but the relations among things; outside these relations there is no reality knowable."

— Henri Poincare, Science and Hypothesis (1905)

TABLE OF CONTENTS

LIST OF FIGURES viii

ACKNOWLEDGMENTS xiii

ABSTRACT xiv

1 INTRODUCTION 1
1.1 Conventional transport near equilibrium 1
1.2 Rectification of unbiased fluctuations 3
1.2.1 Rectification of motion 3
1.2.2 Rectification of energy 8
1.3 Active matter and chiral active matter 9
1.3.1 Collective motion in active matter 9
1.3.2 Momentum transport in chiral active matter 10
1.4 Organization of this thesis 12

2 ENERGY RECTIFICATION IN ACTIVE GYROSCOPIC NETWORKS 13
2.1 Introduction 13
2.2 Model systems and energy flux 15
2.3 Linear response theory for energy flux 18
2.4 Ingredients required for energy rectification 20
2.4.1 Lorentz force and non-equilibrium activity are necessary for the generation of an energy flux 20
2.4.2 Energy flux can be tuned as a function of lattice geometry 22
2.5 A diagrammatic approach to compute the energy flux 23
2.5.1 Diagrammatic expansion and the path rules 25
2.5.2 Diagrammatic decomposition of the energy flux reveals connections between geometry, activity and rectification, and explains localization of energy flux in certain lattice geometries 27
2.5.3 Generalization of the diagrammatic approach to higher-dimensional networks, generic noise spectrum, and heterogeneous parameters . . . 28
2.6 Energy flux in a passive segment coupled to an active network 29
2.7 Non-reciprocal motions responsible for energy fluxes can be used to generate forces 30
2.7.1 Nonreciprocal motion as a swimming protocol 32
2.7.2 Force generation in a viscous medium using the rectified energy fluxes 34
2.8 Conclusion 35

3 ENERGY RECTIFICATION IN ACTIVE GYROSCOPIC NETWORKS WITH TIME-PERIODIC MODULATIONS 37
3.1 Introduction 37
3.2 Model systems and energy flux 38
3.3 An overview of the theory: a two-step perturbation strategy 41

3.4 Perturbative expansion in modulated B-field: a MSR/JDP approach 43
3.4.1 The MSR/JDP path integral formalism 43
3.4.2 Expansion in modulation and expression of multi-point correlators . . 45
3.4.3 Energy flux: first order in modulation 47
3.4.4 Energy flux: second order in modulation 48
3.5 Further expansion in interactions: a diagrammatic approach 49
3.5.1 Diagrammatic expansion of energy flux 49
3.5.2 Diagrams: first and second order in k 51
3.5.3 Diagrams: third order in k 53
3.6 Comparisons between theory and numerical results 55
3.7 Utilizing local building blocks to create complex patterns of energy transport 58
3.8 Conclusion 59

4 A MECHANISM FOR ANOMALOUS TRANSPORT IN CHIRAL ACTIVE LIQUIDS 60
4.1 Introduction 60
4.2 Stress tensor for chiral active fluids 61
4.3 Extracting transport coefficients from the stress tensor 65
4.3.1 Distortion modes of pair correlation functions in a flow field 65
4.3.2 Anomalous transport coefficients 69
4.4 Numerical simulations of a model active rotor system 73
4.4.1 Perpendicular component of the orientation-averaged force 73
4.4.2 Simulation of rotors under a flow field 75
4.5 Conclusion 80

5 SUMMARY AND OUTLOOK 81

A DERIVATIONS RELATED TO ACTIVE GYROSCOPIC NETWORKS 83
A.1 Derivation of energy flux formula 83
A.2 Linear response theory for energy flux 85
A.2.1 Fourier modes for energy flux 86
A.2.2 Integrating over the Fourier modes 88
A.2.3 Moments of the energy transport 90
A.3 Derivation of Kirchoff's law 91
A.4 A Harada-Sasa relation 92
A.4.1 Fluctuation-response breaking 93
A.4.2 Entropy production rate 94
A.5 Connection of energy flux in active networks to eigenmodes in isolated gyroscopic networks 95
A.5.1 Presentation of the connection and application to honeycomb lattices 95
A.5.2 Derivation of the connection 99
A.6 Formulation of the diagrammatic approach to calculating the energy flux . . 102
A.6.1 Derivation of diagrammatic expansion 103
A.6.2 Path rules and discussions 105
A.6.3 Flux of polygon diagrams 106

A.6.4 Contribution from higher-order diagrams . . . 107
A.6.5 Exact flux for 1D networks . . . 109
A.7 Generalization of the diagrammatic approach to a broader range of systems . 111
A.7.1 Generalization of 2D planar space . . . 111
A.7.2 Generalization of OU color noise . . . 112
A.8 Simulation of active gyroscopic network coupled with a passive segment . . . 114
A.9 Relationship between swimmer's speed and energy flux . . . 116

B DERIVATIONS RELATED TO TIME-MODULATED ACTIVE GYROSCOPIC NETWORKS . . . 118
B.1 Numerical calculation of energy flux from time-dependent covariance matrix 118
B.2 No pumping in the adiabatic limit . . . 119
B.2.1 Review of geometric phase and its application to energy flux . . . 119
B.2.2 Application to time-modulated active gyro system . . . 125
B.3 Perturbative expansion in modulated B-field . . . 127
B.3.1 Correlators that involve the response field . . . 127
B.3.2 Two-point correlators in unmodulated reference system . . . 129
B.3.3 First order perturbation . . . 131
B.3.4 Second order perturbation . . . 134
B.4 Diagrams that consist of only loops . . . 140

REFERENCES . . . 143

LIST OF FIGURES

2.1 The model and the energy flux in example networks. (a) Schematic of the model, a spring-mass network with Lorentz-like force and active bath on each particle. (b-d) Averaged energy flux from numerical calculations for example networks. The flux direction and pattern can be controlled by the network geometry. In these figures, gray lines and dots represent the mechanical equilibrium structure of the network, and the size of arrows is proportional to the magnitude of the flux. The arrows are colored blue if it is counter-clockwise (CCW), red if clockwise (CW), and gray for fluxes not on the boundary. The numerical calculations were performed with all parameters set to 1. 16

2.2 Necessary ingredients for generating nonzero energy fluxes. Both Lorentz-like force and colored noise are needed to generate nonzero fluxes. The role of Lorentz-like force is to provide chiral Fourier modes ($J^{FT}(\omega) \neq 0$). If $B = 0$, $J^{FT}(\omega)$ is zero everywhere. The role of colored noise is to provide weighted excitation $h(\omega) \neq$ const., which makes a non-vanishing averaged flux $\langle J \rangle$ possible. The numerical calculations were performed with $m, k_g, k, \gamma, T_a = 1$. 21

2.3 Illustrations of our diagrammatic technique. (a) Flux from site 1 to 2 can be calculated by summing over diagrams. Each diagram is a closed path, which pictorially represent one term in the small-k expansion. Paths are depicted using green arrows. The magnitude of path of length n is on the order of k^n. (b) Schematic of a polygon path and its outer angles $\theta_1, \theta_2, \ldots, \theta_n$. The flux of this diagram is simply Eq. (2.14). (c) For flux in complex networks, the leading order term is determined by the shortest cycles. Flux in the triangle part has order k^3, and the pre-factor c_3 is the same as that in a standalone triangle network. Likewise for the pentagon part. As a result, the flux in a complex network can be viewed as a combination of fluxes in its constituent cycles. 24

2.4 Driving energy through a passive chain. (a) Conventional energy transport in a passive material (boxed in gray) with temperature differences at two ends. Similarly, the active gyroscopic network can also drive energy flows through a passive segment. (b) Instantaneous energy flux J through bonds in the passive segment from a simulation. Flux through different bonds are colored differently. J is stochastic in general, however, during the period when J is large, J exhibits successive peaks in accordance with the direction of the flux. In the simulation setup, parameters for the active particles are: $m, k_g, \gamma = 0.1, k = 10, B, T_a, \tau = 1$. Passive particles (boxed in gray) are constrained to 1D, and their γ, T_a, k_g are set to 0. 31

2.5 Utilization of non-equilibrium gyroscopic dynamics to power swimming and pumping in low Reynolds number (Re) media. (a) The energy flux in the active gyroscopic network is accompanied by nonreciprocal motions of the particles (i,ii). The nonreciprocal motion is a schematic for illustration purposes, and the real data is much more noisy. Using these nonreciprocal motions as input, a three bead linear object can be made to swim through a low Re medium (iii). Our analytical results in (b) below show that the swim speed V_s is in fact proportional to the energy flux $\langle J \rangle$. (iv) Finally by immersing the passive segment into a low Re fluid, the nonreciprocal motions can be used to pump the fluid. In this manner, the energy fluxes can be rectified for locomotion and force generation. (b) Swim speed V_s is proportional to the energy flux $\langle J \rangle$ in the active network. The proportionality constant is $-k_0/k$, which is independent of the network geometry. The series of dots for each $-k_0/k$ are obtained by varying the labelled angles (by red disk sectors) in pentagon networks or "square+tail" networks. The parameters chosen for the numerical calculations are $m, k_g = 0.1$, $\tau = 1$, $k = 5$ for $k_0/k = 0.04$ and $k = 10$ for $k_0/k = 0.02$. For the active part, $\gamma = 0.1, B, T_a = 1$. For the passive segment, $\gamma, B, T_a = 0$. 33

3.1 The model and energy flux in example networks. (a) Schematic of the model, a spring-mass network where each particle is subject to a time-modulated Lorentz-like force and active bath. (b) Energy transferred during each period, Q_i, for networks with shape V and Y. Positive value corresponds to net energy transferred from the bath to the node. Protocol for B-field modulation is $B(t) = \sin 2\pi t/T$, where T is the period of modulation. (c) Energy flux for disordered network subject to a step function protocol $B(t) = 1$ if $t < T/2$, $B(t) = -1$ if $t \geq T/2$. Numerical calculations were performed with all parameters set to 1. 39

3.2 Scaling of energy flux with respect to (a) ΔB and (b) k in for the disordered network in Figure 3.1b. We have separated the modulation $\Delta B(t)$ into an amplitude part ΔB and a time-dependent part. Each single curve is the scaling for one node. Numerical calculations were performed with all other parameters set to 1. 41

3.3 Diagrams for a two-node network from the order (a) k^1, (b) k^2, (c) k^3. The starting/ending node is labeled by a green dot. The number in circles labels the order of segments in the path. 52

3.4 Second order diagrams for a node in arbitrary networks. LHS denotes the flux on second order. Each diagram equals to that in a trimmed network. 53

3.5 Third order diagrams for a node in arbitrary networks. Diagrams can be classified into three groups. 54

3.6 Comparison between flux from direct numerical calculations and flux from perturbative expansions in (a) small ΔB, (b) both small ΔB and small k. The flux is shown for the middle node in the Y-shaped network in Figure 3.1b, and the protocol is $B(t) = \Delta B \sin 2\pi t/T$. All other parameters are set to 1. 56

3.7 Comparison between flux with combined protocol and combination of flux from individual protocols. The protocols read, for instance, $\Delta B_1(t) = \Delta B \sin 2\pi t/T$. (a) Value of fluxes under individual modulation, $\Delta B_1, \Delta B_2$, under combined modulation ΔB_3, and combined flux under individual modulations. (b) Error of combined flux with respect to flux under combinded modulations. The flux is shown for the middle node in the Y-shaped network in Figure 3.1b. All fluxes are calculated from direct numerical methods. All other parameters are set to 1. 56

3.8 Comparison between flux in the full network and combination of flux in trimmed subnetworks. The error in flux is averaged over all nodes. We used the disordered network in Figure 3.1c. The modulation is a step-function modulation where the period is set to 1. All fluxes are calculated from direct numerical methods. All other parameters are set to 1. 57

3.9 Creating target flux patterns by exploiting the connection between flux in a network and in its local subnetworks. (a) Flux of network with branches. (b) Constructed network and its flux pattern that mimics a grayscaled book. The modulation is a step-function modulation where the period is taken to infinite. All fluxes are calculated from direct numerical methods. All parameters are set to 1 except that $k = 0.05$. 58

4.1 Schematic of the type of system we consider and the emergence of perpendicular averaged force. (a) A chiral active system with interacting rotors experiencing active torques. (b) After averaging over the orientation of rotors, the orientation-averaged intermolecular forces generically contain both an ordinary radial component $\overline{\boldsymbol{F}}_{\parallel}(\boldsymbol{x})$ and a peculiar perpendicular component $\overline{\boldsymbol{F}}_{\perp}(\boldsymbol{x})$. We will show that the anomalous transport coefficients can be expressed in terms of this perpendicular force. 62

4.2 Schematic of the four modes of $g(\boldsymbol{x})$-distortion induced by a velocity gradient $\nabla \boldsymbol{u}$. The first row depicts three types of velocity gradient, dilation, pure shear flow, and vortical flow. The second row shows the corresponding modes of $g(\boldsymbol{x})$-distortion. Dotted circle represent the first peak of the undistorted $g(\boldsymbol{x})$, and the solid circles or ellipses are schematics of the distorted $g(\boldsymbol{x})$. In particular, the pure shear sketched in the middle column can induce two modes of distortion, denoted by m^s and m^a. The third row labels these distortion modes according to Eq. (4.22)-(4.25). 70

4.3 Transverse components in the orientation-averaged intermolecular forces. (a) The inter-rotor potential used in our numerical simulations. Each rotor is simulated by nine beads, which are labeled as red dots. Beads belonging to different rotors interact via a Gaussian potential $V(r) = \epsilon e^{-r^2/2\sigma^2}, \sigma = 0.25a$. The figure plots the superposition of the Gaussian potential from the nine beads. (b) A snapshot of a section of the simulation system. Each rotor is driven in a counter-clockwise direction. (c) Perpendicular component of the averaged inter-rotor forces at different torques. Shaded region around each curve represent 95% confidence interval. τ is the external torque, and $\tau/5\gamma a^2$ is the average angular velocity of rotors under the external torque when the rotors are non-interacting. 74

4.4 Averaged parallel and perpendicular force from simulated rotor systems under a flow field. (a) Profile of applied external force F_y and the measured averaged velocity u_y in y-direction. Data is shown for $\lambda = 0.0444$. Due to periodic boundary condition, u_y close to the boundary $|x| = 30a$ decreases to zero. Calculation of inter-rotor forces only include rotors whose center of masses are inside the shaded region ($|x| < 25a$), where the averaged velocity is linear in x. (b) $\bar{F}_{\parallel}(r)$ and $\bar{F}_{\perp}(r)$ for $\lambda = 0, 0.0222, 0.0444, -0.0444$. $\bar{F}_{\parallel/\perp}(r)$ at different λ's basically overlap, which shows that small applied flow fields do not induce significant changes in $\bar{F}_{\parallel/\perp}(r)$. To avoid overcrowding the plot, legends for colors corresponding to different λ's are not shown. Shaded region around each curve represent 95% confidence interval, which is small compared with the line width. 76

4.5 Distortion of the pair correlation function induced by a simple shear flow field. (a) $g(x, y)$ under a simple shear flow $\partial_x u_y = 0.0444\sqrt{\epsilon/ma^2}$ is distorted to an elliptical shape (i). Apparently, the distortion $\Delta g(x, y)$ (ii) is slightly rotated counter-clockwisely compared with that in ordinary liquids. (iii) plots the mode $(\Delta g(x, y) - \Delta g(x, -y))$, which is proportional to $xym^s(r)$, and is labeled by $xym^s(r)$ for simplicity. The data is rescaled by a factor of 0.5 to accommodate the scale of the colorbar. The other two modes, $(\Delta g(x, y) - \Delta g(y, x)) \propto (-x^2 + y^2)m^a(r)$ and $(\Delta g(x, -y) + \Delta g(y, x)) \propto m^r(r)$ are plotted in (iv) and (v), respectively. The $\Delta g(x, y)$ reconstructed from the fitted $m^{s,a,r}(r)$ (vi) agrees well with $\Delta g(x, y)$ directly computed from simulation (iii). (b) $m^{s,a,r}(r)$ fitted from the data in (a). Shaded region around each curve represent the standard deviation of residues at each r. 77

A.1 Comparison between a boundary-localized eigenmode of the undamped isolated network and the Fourier modes of the damped network at the same frequency. First order dynamics (by setting $m = 0$) are used. Numerical calculations are performed with all other parameters set to 1. (a) Eigenmode of undamped gyroscopic system. For the frequency chosen, the eigenmode is localized on the boundary. Blue disks represent the orbit of particles. (b) The Fourier mode of damped variant of our model at small γ ($\gamma = 0.001$) resembles the eigenmode. (c) The Fourier mode at larger γ ($\gamma = 1$) is no longer close to the eigenmode. . 96

A.2 Using the eigenmode decomposition, we explain how the flux in honeycomb network is CCW, even though its edgemodes contribute to CW fluxes. (a) Network used for calculation, which consists of one row of hexagons (51 unit cells) and has periodic boundary in x direction. Parameters: $k_{g,\tau} = 1, k = 10$, others are 1. (b) Band structure of the network (marked with different colors). The yellow/green band contains CW flux localized on the top/bottom edge (an example mode is shown in (d)/(e)). The blue band contains bulk modes with CCW flux (also see (f)). (c) Weighted flux $J^{eig}_{\omega_e}$ from 1 to 2 (marked in (a)) of the four bands. Total flux in the green band with CW edge modes and the blue band with CCW bulk modes are -0.106 and 0.115, respectively. As a result, the net flux is CCW. . . 98

A.3 Higher-order diagrams in a tailed-square network. (a) Direction of flux can be controlled by the orientation of the side-chain. (b) From diagrammatic approach, the flux of the lowest-order diagram (square) vanishes, and the first non-vanishing diagram is affected by the side-chain. 108
A.4 Decay of fluxes away from the boundary of honeycomb networks, and explanation using the diagrammatic technique. (a) Schematic of a honeycomb network which is periodic in the x direction. Layers from the boundary are indexed as n_l. (b) Semi-log plot of flux $\langle J \rangle$ at layer n_l. The flux starting from layer $n_l = 1$ shows exponential decay, with decay length d_l. Parameters used for numerical calculations are $\theta = \pi/6, k/k_0 = 0.01, \alpha = \pi/4$. (c) Decay length d_l changes with the network angle θ non-monotonically, and the curve has a cusp at $\theta = \alpha = \pi/4$. At small k/k_0, perturbation theory results agree with numerical calculations. (d) The first non-vanishing diagram pair for $n_l = 1$ has length 7. The two diagrams do not cancel, because the loop in the bulk and at the boundary have different values. 108
A.5 One example of $\langle J^s_{31} \rangle$ diagram (red) and $\langle J^s_{12} \rangle$ diagram (blue). Passive particles are boxed in gray, and the active ones are boxed in red. 116

ACKNOWLEDGMENTS

I would like to thank my advisor Prof. Suriyanarayanan Vaikuntanathan for his great academic and financial support throughout my graduate life. I first met Suri in his statistical thermodynamics class. I was interested by his teaching style, and I later joined his group. It is amazing to see how diverse the research topics have been in the group. Suri constantly come up with new ideas, which often times try to connect seemingly disparate topics. The research process may be filled with frustrations in the beginning, but in the end it became extremely rewarding. Suri is very supportive of attending conferences and meeting with scientists outside our department. He gave lots of useful advices of how to best present the work to the target audience. I was among the first members of the Suri group, along with two other classmates, Clara and Nick. It has been privileged to see how the group started from scratch and evolved to a medium-sized team. I look forward to hearing more good news from the group.

Besides Suri, I would also like to thank my other committee members, Prof. Aaron Dinner and Prof. William Irvine. They have been very supportive of serving on my dissertation committee. Aaron graciously listened to my presentation of research progress back in summer 2019, which was not well structured at the time. William and Suri used their humor to help me relieve my anxiety before the defense. Tom kindly agreed to sit in my defense due to the emergency of another committee member, which made my defense a smooth experience.

I would like to thank my academic collaborators, Prof. William Irvine, Prof. Vincenzo Vitelli, Dr. Michel Fruchart and Dr. Ming Han. We had many interesting discussions, from which I have learnt a lot in terms of scientific knowledge as well as different styles to do science. They have also been extremely helpful in manuscript writing.

Finally, I would like to thank my friends and my family who have enriched my life.

ABSTRACT

Conventional transport processes are driven by biases, e.g., diffusion is driven by concentration biases, heat flow is driven by temperature biases. Anomalous transport, although rarely seen in our daily lives, is also important. For instance, intracellular transport cannot only rely on diffusion, rather, cargoes are transported through directed motion of molecular motors along microtubules. Compared with the anomalous transport of mass, the transport of energy and momentum are much less well studied. In this thesis, we describe these two types of anomalous transport in a few classes of chiral active systems. The first class is active gyroscopic networks, which we construct by subjecting spring-mass networks to unbiased nonequilibrium fluctuations and Lorentz forces. We numerically demonstrate the emergence of energy rectification, in other words energy transport in the absence of temperature biases, between nodes for unmodulated networks, and between nodes and baths in time-modulated networks. We develop analytical diagrammatic theories that allow us to understand and control the rectification in arbitrary complex networks in terms of local properties. The second class is chiral active liquids. Previous studies have shown the existence of anomalous transport coefficients such as the so-called odd viscosity in these systems. Extending the Irving-Kirkwood theory for conventional fluids, we develop a theory for anomalous transport in chiral active liquids. We show how the transport coefficients can be connected to local molecular properties, specifically the averaged intermolecular forces and distortions of pair correlation functions. Taken together, we have contributed to the topic of anomalous transport of energy and momentum. Our analytic theories have provided frameworks to understand complex transport processes in terms of relatively simple local properties.

CHAPTER 1

INTRODUCTION

Our main focus in the thesis will be on developing strategies to achieve and understand anomalous transport of energy and momentum in microscopic systems. Before discussing anomalous transport, in this introduction we first review conventional diffusive transport and introduce the statistical mechanics frameworks that describe conventional transport processes in Sec. 1.1. Then we review one class of anomalous transport called rectification in Sec. 1.2. Rectification has been widely studied in the context of directed motion, but a few efforts have also investigated rectification of energy. In Sec. 1.3 we review anomalous momentum transport in chiral active fluids, following a review of the field of active matter physics. Finally in Sec. 1.4 we outline the organization of the remainder of this thesis.

1.1 Conventional transport near equilibrium

Transport phenomena are commonly seen from our daily experience, heat flows from hot to cold, smells of food diffuse in the air, water flows in pipes. Such transport phenomena are driven by biases in temperature, concentration, or pressure. These biases can in principle be arbitrarily large, but for the purpose of reviewing statistical mechanical frameworks, we consider cases with small biases, or conditions near equilibrium.

Early efforts to describe such transport gave rise to phenomenological laws such as Fourier's law for heat conduction (in 1822 [1]) and Fick's law for diffusion (in 1855 [2]). Fick's law, for instance, states that the current of particles $\mathbf{J}$ is proportional to the negative concentration gradient $-\nabla c$ by a factor called diffusion constant, D,

$$\mathbf{J} = -D\nabla c. \tag{1.1}$$

These phenomenological laws formulated more than 150 years ago are highly successful in describing transport in a wide range of systems. Efforts in recent decades have also found

systems that violate these laws, which led to investigations of anomalous diffusion [3] and heat conduction in low dimensional systems [4].

Later developments showed that these transport coefficients are not mere phenomenological factors. These near-equilibrium coefficients are actually related to properties in equilibrium. Einstein (in 1905 [5]) found the relation between diffusion constant D and mobility μ (ratio between forcing and drift velocity),

$$D = \mu k_B T, \tag{1.2}$$

where k_B is the Boltzmann's constant and T is the temperature. By expressing the diffusion constant in terms of mean-squared displacements, a relation can be obtained between the response to external forcing and the fluctuations under equilibrium,

$$\mu = \frac{1}{k_B T} \int_0^\infty \mathrm{d}t \, \langle v(0) v(t) \rangle_{eq} \,, \tag{1.3}$$

where $v(t)$ is the velocity, and the average $\langle \cdot \rangle_{eq}$ is performed under equilibrium conditions.

The relation between response near equilibrium and fluctuations in equilibrium was formulated systematically by the fluctuation-dissipation theorem (alternative names in the literature include Green-Kubo relation and linear response theory). The fluctuation-dissipation theorem can be formulated as follows [6]. Consider a system governed by Hamiltonian H, now add a time dependent perturbation $-AK(t)$ to the original Hamiltonian, then ask how an observable $B(t)$ changes due to the perturbation. Such change is characterized by a response function $\phi_{BA}(t)$ through

$$\langle \Delta B(t) \rangle = \int^t \mathrm{d}t' \, K(t') \phi_{BA}(t - t'). \tag{1.4}$$

The fluctuation-dissipation theorem states that the Fourier transform of the response func-

tion (susceptibility) is related to the fluctuation in equilibrium through

$$\xi_{BA}(\omega) = \frac{1}{k_B T} \, \mathrm{d}t \left\langle \dot{A}(0) B(t) \right\rangle e^{-i\omega t}, \tag{1.5}$$

$$\xi_{BA}(\omega) = \int \mathrm{d}t \, \phi_{BA}(t) e^{-i\omega t}. \tag{1.6}$$

The response function can be instantiated as shear viscosity, thermal conductivity, or other transport coefficients [6, 7]. When there are multiple biases or fields, the relation between thermodynamic fluxes J_i (e.g. heat flux) and thermodynamic forces X_i (e.g. temperature gradient, $-(\partial_x T)/T$) can be approximated as a linear relation,

$$J_1 = R_{11} X_1 + R_{12} X_2, \tag{1.7}$$

$$J_2 = R_{21} X_1 + R_{22} X_2. \tag{1.8}$$

For systems with time-reversal symmetry, the Onsager reciprocal relations states that the coefficients are reciprocal, $R_{12} = R_{21}$ [8, 9, 10]. The Onsager relations have implications on, e.g., controlling heat transport using electric field, which can be utilized to build refrigerator with no moving parts [11].

From this brief review of transport processes and nonequilibrium thermodynamics, we see that conventional transport are driven by biases and can be described by transport coefficients. These coefficients are note merely phenomenological factors, but rather they satisfy Green-Kubo relations and Onsager reciprocal relations.

1.2 Rectification of unbiased fluctuations

1.2.1 Rectification of motion

Transport driven by gradients is ineffective, for instance, when it comes to cargo transport inside cells. Due to the complexity of intracellular environment, cargo transport relies on

directed motion of motor proteins on microtubules or actin filaments [12]. Note that the directed motion of motor proteins is not driven by concentration gradient. Understanding the physics of such directed motion has become one important inspiration for studies under names of rectification, Brownian ratchet or Brownian motors [13].

Historically, interests in generating directed transport through rectification of unbiased fluctuations started long before the discovery of molecular motors. As pointed out by the comprehensive review Ref. [14], studies on rectification have actually started from several different directions and have experienced rediscoveries in different contexts. Review here picks the branch of directed motion first analyzed by Smoluchowski [15, 16] in 1912 and then popularized by Feynman in 1962 [17, 16].

Feynman in his famous lectures [17] described a ratchet and pawl model which at the first sight may violate the second law of thermodynamics. In this model, there is a vane immersed in a box of gas at some temperature. The gas molecules collide with the vane and cause the vane to rotate, but since the collisions are random, the probability of rotating in both directions are the same, where no directed motion can happen. Now connect the vane through an axle to a ratchet and pawl combination. At the first glance, the pawl only allows the ratchet to rotate in its forward direction, and the directed motion can be utilized to lift a cargo, seemingly violating the second law of thermodynamics (absorbing heat from a single reservoir and perform work). This naive analysis, however, neglects that the pawl itself is subject to thermal motions. When the temperature of the vane and the ratchet and pawl are identical, Boltzmann distribution states that the probability of the ratchet rotating forward is the same as it rotating backward due to the thermal excitation of the pawl. As a result, the second law is not violated. An isothermal ratchet and pawl model does not rule out the possibility of directed motion when the model is placed under nonequilibrium conditions by immersing the vane and the ratchet and pawl in different temperatures. For instance, if the temperature of ratchet and pawl is zero, then the pawl would not disengage from the ratchet, allowing unidirectional rotation. Ref. [18] detailed how rectification works

by analyzing an exactly solvable model that captures essential ingredients of the ratchet and pawl model. Recently the ratchet and pawl model was realized in experiment [19].

As mentioned in the beginning of this subsection, intracellular transport by molecular motors have been an inspiration for research on rectification. A number of studies have analyzed the possibility of Brownian ratchet being a mechanism for directed motion of the molecular motors [13, 20, 21]. With more advanced experiments and detailed atomistic simulations, a recent review compared the Brownian ratchet mechanism with another candidate named power stroke, and they conclude that power stroke seems to be the main contribution whereas Brownian ratchet is also complementary during some stages of the cargo transport [22].

Among the various types of Brownian ratchet [14], rectification utilizing colored noise [23, 24, 25] is particularly relevant to our work. Here we review a theoretical framework to treat the colored noise which is exponentially-correlated in time. Such colored noise is also called Ornstein-Uhlenbeck (OU) noise because it can be generated through an OU process [26]. The OU colored noise breaks fluctuation-dissipation relation, thus driving the system out of equilibrium [27]. Compared with the original ratchet and pawl model where the nonequilibrium effect is transmitted through an axle and the load can only move in one direction, the OU noise is directly acting on the particle, thus can allow the particle to navigate a potential landscape beyond 1D [28]. An efficient theoretical framework to deal with the OU noise is the unified colored-noise approximation (UCNA) [29, 26]. Following Ref. [29], we consider a particle subject to OU noise moving in a 1D potential landscape,

$$\dot{x} = f(x) + \eta(t), \tag{1.9}$$

$$\langle \eta(t)\eta(t') \rangle = \frac{D}{\tau} e^{-|t-t'|/\tau}, \tag{1.10}$$

where $f(x)$ is the force on the particle, $\eta(t)$ is the OU noise, D is the diffusion constant, and τ is the correlation time. UCNA aims to find an approximation for the dynamics of OU

particle that works in both small τ and large τ regime. Such exponentially-correlated noise correlation can be produced by an OU process,

$$\tau\dot{\eta} = -\eta + \sqrt{D}\xi(t), \tag{1.11}$$

$$\left\langle \xi(t)\xi(t')\right\rangle = 2\delta(t-t'), \tag{1.12}$$

where $\xi(t)$ is a Gaussian white noise. From either Eq. (1.10) or Eq. (1.11), we see that if the correlation time $\tau \to 0$, the OU noise reduces to a Gaussian white noise. Eliminating the colored noise η in Eq. (1.9) using Eq. (1.11) yields a second order stochastic equation for x but subject to a white noise ξ. Rescaling the time t to $s = t/\sqrt{\tau}$, then the first order term in the equation in s has a prefactor that is large when $\tau \to 0$ or $\tau \to \infty$, so that the second order term can be omitted. The resulting UCNA approximation reads

$$\dot{x} = \frac{f(x)}{\gamma(x,\tau)} + \frac{D^{1/2}\tau^{-1/4}}{\gamma(x,\tau)}\xi(s), \tag{1.13}$$

$$\gamma(x,\tau) = \tau^{-1/2} - f'(x)\tau^{1/2}. \tag{1.14}$$

An important feature of UCNA is that the effective diffusion in Eq. (1.13) now depends on x, or in other words, the diffusion is state-dependent. UCNA can be generalized to systems with more than one degree of freedom [30, 31]. The state-dependent diffusion can be viewed a state-dependent effective temperature. Consider the situation that the effective temperature is low where the ratchet potential is steep, then the particle can hardly move over the steep side, thus resulting in a directed transport through the less-steep direction [32]. In another approach to understand the Brownian ratchet with OU particles, Ref. [33] considers the motion of state in an extended space $\{x, \eta\}$. Directed transport of OU particle in a ratchet landscape has been realized in experiment in recent years [28], where the particles are micrometer-sized colloids, OU noise is provided by a bath with bacteria [34, 35], and ratchet landscape is built through nanofabrication.

The state-dependent diffusion itself is a useful and widely-studied concept. It has been used to construct another type of Brownian ratchet, the Buttiker-Landauer ratchet [36, 37], where the setup consists of potential landscape and state-dependent temperature. Ref. [36] showed that this combination can produce a tilted effective potential landscape, thus driving the directed motion. The effective potential can be tuned to generate transport with low randomness [38], which means that if we repeat the stochastic process multiple times, the variance between trajectories is small. State-dependent diffusion has also been used to study a symmetric Brownian ratchet model [39]. In this model, the original dynamics consists of additive noise, but a transform of variables used to understand the rectification results in dynamics with state-dependent diffusion.

Most Brownian ratchets reviewed above require asymmetric potentials, with the Buttiker-Landauer ratchet one exception [36, 37]. There are other ratchet models that can operate in symmetric potentials, such as utilizing correlations between noises [40] or the space-time symmetry breaking [41]. Whereas most Brownian ratchets are on a single-particle basis, studies of collective effect is also important for understanding, e.g., intracellular transport of cargos by a collection of molecular motors [13, 42].

Apart from theoretical and computational studies of Brownian motors, recent decades has also seen a collection of experimental studies of Brownian ratchets using colloids and/or bacteria [43, 44, 45, 46]. These applications are made possible with more understandings of behavior of microswimmers [47, 48] and advance in nanofabrication technologies. In an early work, Ref. [49] in 2007 constructs a funnel wall that separates a chamber into left and right half. The ratchet-shaped wall is able to concentrate self-propelling bacteria into one have of the chamber. Ref. [50] used bacteria to drive the rotation of gears with size tens of micrometers. These examples, along with many others [46], have enriched our toolbox for constructing artificial motors and understanding of their behaviors.

1.2.2 Rectification of energy

Inspired by Brownian ratchet for rectifying motion, a few studies in 2002 asked how to rectify energy using unbiased fluctuations [51, 52]. The resulting phenomena are energy fluxes in the absence of temperature biases.

We note that in the literature, the terminology "energy rectification" has also been used to describe diode effects [53, 54, 55], which is different from our usage of "energy rectification" in this thesis. These two usages of energy rectification, however, are not totally unrelated. Ref. [56] exploited a thermal diode model to achieve energy rectification in our sense by modulating the temperature of one reservoir in a time-periodic manner. Ref. [57] took a step further to modulate the temperature of both reservoirs while keeping the two temperatures identical, achieving energy rectification under "strict zero thermal bias" in their words.

Examples of rectification mentioned above [52, 57] require nonlinearity in the material, which hinders theoretical approaches. There exists other rectification strategies that allows for more analytical approaches. Examples include applying reservoirs with non-Gaussian fluctuations [58, 59, 60] or utilizing geometric phases generated in adiabatic modulations [61]. Interestingly, the later case [61] adapted a previous method for geometric phase in stochastic pumping [62, 63, 64] to study contributions to energy transport from geometric phases. The method in Ref. [61] yields analytic expressions for energy flux in their model with two particles connected by a linear spring [61]. This method can also apply to energy flux in more general systems in order to understand, for instance, why rectification vanishes in the adiabatic limit in Ref. [57].

Despite these pioneering studies, rectification of energy is much less well explored compared with rectification of motion. In particular, most studies for energy rectification focus on transport in a 1D material. It is unclear how these strategies can be generalized to higher dimensions. One motivation for such generalization is that the supported geometries will be much richer, in contrast to the restriction of linear layout in 1D. One rare example of transport in 2D, though not exactly aligning with our sense of energy rectification, is the

radiative heat transfer among magneto-optical nanoparticles [65, 66, 67].

1.3 Active matter and chiral active matter

1.3.1 Collective motion in active matter

Studies of Brownian motor driven by colored noises [28, 46], as we reviewed in Sec. 1.2.1, intersect with another field called active matter physics. Particles subject to colored noise are "active" in the sense that there is energy injection into the particles which breaks detailed balance [68]. There are other ways to make particles active [69].

Active matter physics studies collective behaviors resulting from active constituents and their interactions [70]. Early studies of active matter were motivated by the phenomenon of bird flocking, or more generally, collective motion of a group of animals such as birds, fish, ants, etc. In the flocking behavior, a group of birds fly in a synchronized direction, at the same time they also change the direction constantly. Directed motion in flocking is different from the conventional transport because there is no external bias applied to the bird flock.

Reynolds was fascinated by the flocking phenomena and simulated such phenomena for the purpose of creating computer animations in 1987 [71]. Ref. [71] constructed a boid model to simulate the flocking behavior with three simple rules, namely collision avoidance, velocity matching, and flock centering (trying to fly close to nearby birds). Collective behavior such as flocking also attracted physicists' attention to perform more quantitative investigations. Vicsek in 1995 [72] proposed a qualitatively similar agent-based model and studied the phase transition from the disordered state to the flocking state. The Vicsek model consists of agents moving in 2D space where each agent's speed is fixed but its angle θ is updated according to

$$\theta(t + \Delta t) = \langle \theta(t) \rangle_r + \Delta\theta, \tag{1.15}$$

where $\langle \theta(t) \rangle_r$ denotes the average angle of neighboring particles within a radius r, and $\Delta\theta$

is a random perturbation. Toner and Tu in 1995 [73, 74] introduced a continuum theory to describe a large class of dynamical models. The Toner-Tu field equation reads [74]

$$\begin{aligned}\partial_t \boldsymbol{v} + \lambda_1(\boldsymbol{v}\cdot\nabla)\boldsymbol{v} + \lambda_2(\nabla\cdot\boldsymbol{v})\boldsymbol{v} + \lambda_3\nabla(|\boldsymbol{v}|^2) = \\ \alpha\boldsymbol{v} - \beta|\boldsymbol{v}|^2\boldsymbol{v} - \nabla P + D_B\nabla(\nabla\cdot\boldsymbol{v}) + D_T\nabla^2\boldsymbol{v} + D_2(\boldsymbol{v}\cdot\nabla)^2\boldsymbol{v} + \boldsymbol{f},\end{aligned} \tag{1.16}$$

where $\boldsymbol{v}$ is the velocity and $\boldsymbol{f}$ is the fluctuating force. The Toner-Tu equation is a Navier-Stokes equation modified by additional terms that are allowed by symmetries [74]. A connection between the discrete Vicsek model and the continuous Toner-Tu model was made by Ref. [75]. From a physicist's view, the phase transition to flocking was surprising because the Mermin-Wagner theorem forbids long-range order in equilibrium systems with continuous symmetry [76]. The flocking phenomenon clearly is a nonequilibrium behavior, nevertheless, some concepts originated in equilibrium statistical mechanics can be adapted to active systems. One example is the concept of universality class [77, 78, 79], which can lead to classification of collective motion in various systems [80, 81].

Started from these early studies [72, 73, 74], general features for active matter was later extracted. Unlike conventional nonequilibrium systems that are driven by boundary, active matter systems break equilibrium by injecting energy to each individual constituent. One widely-studied type of active species is self-propelling particles, which can lead to phenomena such as collective motion [70, 80, 82, 83, 84, 85] or phase separation [86, 87]. These active species can be realized experimentally using chemical [88] or biological [46] approaches. Tools from active matter physics has also been applied to study biological processes such as cell division [89], tissue mechanics [90, 91], and biological materials [92, 93].

1.3.2 Momentum transport in chiral active matter

Chiral active matter is a class of active matter where the energy injection to each agent takes place at the rotational degree of freedom. Long-wavelength motion of chiral active matter can be well described by hydrodynamic theories. Compared with the familiar Navier-Stokes

equation for ordinary fluids, the hydrodynamic description of chiral active fluids requires additional terms. These additional terms and coefficients, such as "odd" viscosity, encode anomalous transport of momentum.

An interesting work in 2005 [94] and a few related works [95, 96] showed that although angular momentum is injected at the individual level, the system can exhibit large-scale transport of particles that is localized at the boundary of the system. The edge current can be explained by hydrodynamic theory of chiral active matter. The equation for momentum g and angular momentum l read [94]

$$\partial_t g_i = -\partial_j(g_i v_j) - \partial_i p + \eta\nabla^2 v_i - \Gamma^v v_i + \frac{1}{2}\epsilon_{ij}\partial_j\Gamma(\Omega-\omega), \tag{1.17}$$

$$\partial_t l = -\partial_j(l v_j) - \Gamma^\Omega\Omega - \Gamma(\Omega-\omega) + D_\Omega\nabla^2\Omega + \tau. \tag{1.18}$$

This set of equations is an extension of Navier-Stokes equation. Due to the presence of chiral active agents, the hydrodynamic equations need to include angular momentum l, spin Ω and vorticity ω [97, 94]. In particular, the term $\Gamma(\Omega-\omega)$ couples spin and vorticity and produce an odd component in the stress tensor. The analysis of the steady state solution of the hydrodynamic equations shows a boundary-localized current [94, 95].

A more recent study in 2017 [98] argued that the above hydrodynamic equation is incomplete, there should be an additional term from the so-called odd viscosity, although the contribution from this term may be negligible for some systems. The odd viscosity term was proposed in 1998 for generic time-reversal breaking systems [99]. Viscosity tensor describes the constitutive relation between stress tensor and velocity gradients. When a pure shear is applied, the shear viscosity produces a parallel response in the stress tensor, whereas the odd viscosity produces a response in the transverse direction. The odd viscosity was later measured in an experimental system with rotating colloids [100]. The odd stress and/or odd viscosity was also investigated in combination with ideas from topological mechanics [101, 102].

One question the hydrodynamic approach cannot directly answer is the microscopic origin of the phenomenological coefficients that appear in the hydrodynamic equations. Such connection calls for statistical mechanical studies. There has been a few studies on statistical mechanics of rotating dimers [103] or efforts to derive Green-Kubo relations for time-reversal breaking systems [104].

1.4 Organization of this thesis

From the preceding introductory sections, we have seen that the anomalous transport of energy and momentum is in general much less well explored compared with the transport of motion. In this thesis, we explore principles for energy rectification and statistical mechanics of the anomalous transport in chiral active fluids. In Chapter 2, using a model nonequilibrium parity-breaking spring-mass network we show how energy rectification beyond 1D can be achieved. We develop an analytic diagrammatic approach to understand and control the rectification in complex networks in terms of local structures. This energy rectification have further implications on swimming in or pumping of low Reynolds number fluids. In Chapter 3, using a time-modulated variant of the spring-mass model we show how energy rectification can mimic temperature inhomogeneities. We provide a theoretical framework to understand such rectification using a combination of path integral formalism and a diagrammatic approach. In Chapter 4, we develop a statistical mechanical mechanism for anomalous transport in chiral active fluids. The approach is an extension of the Irving-Kirkwood method [105] and it relates the hydrodynamic coefficients to distortions of pair correlation functions and averaged intermolecular forces. Taken together, our central results provide theoretical frameworks to understand seemingly complex transport properties in terms of relatively simple local properties.

CHAPTER 2

ENERGY RECTIFICATION IN ACTIVE GYROSCOPIC NETWORKS

This chapter is reproduced and adapted from the preprint: Liao, Zhenghan, William T. M. Irvine, and Suriyanarayanan Vaikuntanathan. 2019. "Rectification of Energy and Motion in Non-Equilibrium Parity Violating Metamaterials." arXiv:1907.05938 [106].

2.1 Introduction

Identifying mechanisms that rectify stochastic fluctuations is a longstanding problem in non-equilibrium statistical mechanics with many biological, chemical and physical applications [107, 20, 13, 14, 46]. For instance, the Feynman ratchet and pawl model [17] and its associated extensions have elucidated how systems can rectify stochastic fluctuations and act as microscopic engines that perform work and exert forces [14, 13]. Indeed such models have provided a framework to understand how biological molecular motors can convert the energy derived from the hydrolysis of energy rich molecules into mechanical work [20, 43, 108, 109, 46, 22]. These ideas have also inspired studies exploring strategies to enable directed energy transport in the absence of any temperature biases [51, 52, 56, 57, 61, 110, 58, 59, 60]. Compared with directed motion whose basic mechanism can be understood in the single-body basis [14], directed transport of energy by definition is a many-body effect. However, strategies to achieve such energy rectification have been rarely explored beyond one-dimensional (1D) setups [65, 66, 67] and it remains to be seen if opportunities provided by richer geometries and higher dimensions can be exploited.

In this chapter, we explore an opportunity provided by a class of spring-mass networks that are subject to non-equilibrium forcing and possess parity violating dynamics, to uncover new many-body principles for rectification of energy and motion in meta-materials with arbitrarily complex geometries and connectivity. Non-equilibrium forcing is an essential

requirement for rectification [14]. Here, we achieve non-equilibrium forcing by coupling our metamaterial to an active bath [26, 23, 111]. Rectification also requires additional broken symmetries [14]. Here we use meta-materials with parity violating dynamics [112, 113, 114]. Our central analytical results, compactly represented as a diagrammatic expansion for the energy fluxes in the non-equilibrium meta-material, show how meta-materials with parity violating dynamics –such dynamics were recently exploited to generate chiral topological eigenmodes in gyroscopic meta-materials[112, 113, 115, 114]–are able to rectify energy and motion when allowed to interact with a bath of active particles.

Our central analytical results, in particular, the aforementioned intuitive diagrammatic approach, allow us construct arbitrarily complex non-equilibrium parity violating metamaterial networks that generically support a directed flux of energy between their nodes. The diagrammatic approach also illustrates how a hierarchy of fluctuations are responsible for the energy transport, starting from lowest-order diagrams that only depend on local structures of the network, to higher-order diagrams that involve more and more non-local structures. Importantly, the leading-order diagrams describe the many-body effect in a compact analytic form, Eq. (2.14), that elucidates how a simple interplay between the geometry, activity, parity violation enable rectification. The diagrammatic expansion, even at lowest order, hence provides concrete design principles for controlling the rectification of energy by our metamaterials.

Unlike conventional energy flows, our energy flow does not require a temperature gradient. This flux can be routed through an otherwise isolated elastic object with the active network acting as a current source. Finally, we show that the microscopic mechanisms responsible for this energy flow can also potentially allow the elastic object to swim in and exert forces on a viscous fluid. Taken together, our results establish a new mechanism for rectification of energy and motion in non-equilibrium parity violating metamaterials. Unlike existing prescriptions, our mechanism exploits inherent asymmetries in the nonequilibrium fluctuations of the active bath, parity-violating dynamics and network geometry to achieve

rectification.

The remainder of this chapter is organized as follows. In Sec. 2.2, we introduce our model parity violating metamaterial and provide a microscopic definition for the energy flux. In Sec. 2.3-2.5 we analytically identify the ingredients for rectification of energy fluxes and construct a diagrammatic approach that reveals a relationship between energy flux and network geometries. Finally in Sec. 2.6-2.7 we show that when the particles transmitting the energy flux are allowed to interact with a viscous low Reynolds number fluid, the nonreciprocal motions responsible for the energy flux can be utilized to pump the viscous fluid.

2.2 Model systems and energy flux

Our model is a tethered spring-mass network in which each particle is additionally subject to stochastic forcing from an active bath and a Lorentz-like force (Figure 2.1a). The linearized equation of motion is

$$m\dot{v}_i = -k_g z_i + \sum_j F_{ji} - BA_1 v_i - \gamma v_i + \eta_i. \tag{2.1}$$

$z_i \equiv \begin{pmatrix} x_i & y_i \end{pmatrix}^T$ is a column vector that denotes the displacement of particle i from its mechanical equilibrium position, and similarly v_i and η_i describe the $2D$ velocity of and noise on each particle. $-k_g z_i$ is the on-site tethering force used to maintain the shape of the network. $F_{ji} = k(e_{ij}^T z_i + e_{ji}^T z_j)(-e_{ij})$ is the linearized spring force from j to i, where e_{ij} is the unit vector that points from the equilibrium position of i to that of j. $-BA_1 v_i = -B \begin{pmatrix} v_{i,y} & -v_{i,x} \end{pmatrix}^T$ is the Lorentz-like force, with $A_1 \equiv \begin{pmatrix} 0 & 1 \\ -1 & 0 \end{pmatrix}$, and the Lorentz-force's customary electric charge-like factor is absorbed in B. The construction of our model system is motivated by the recently constructed topological gyroscopic metamaterials [112] and in the linearized regime, the equations of our model system are equivalent to the equations of motion of the gyroscopic metamaterials [115].

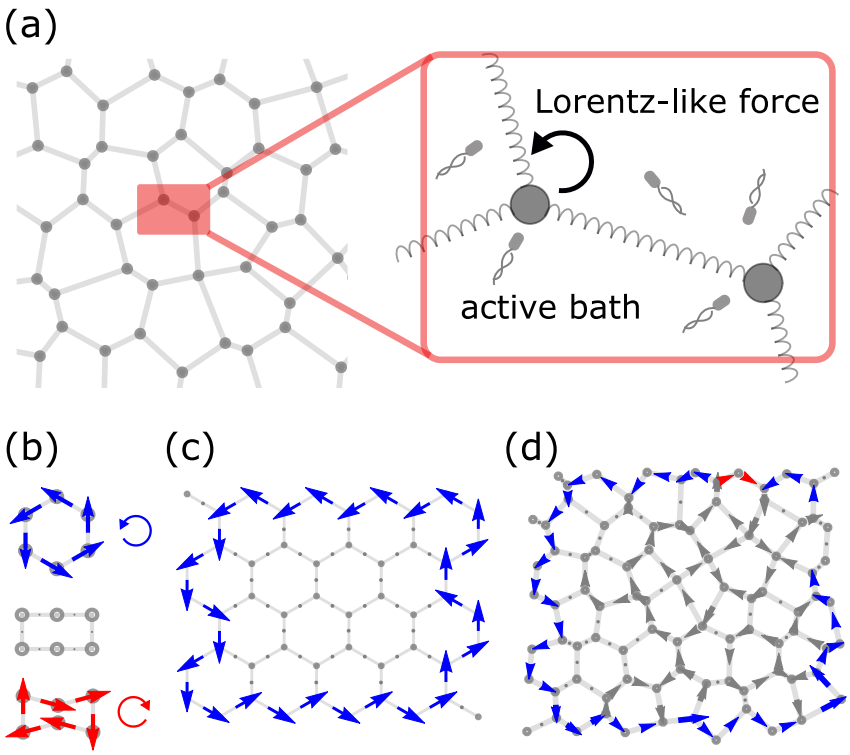

Figure 2.1: The model and the energy flux in example networks. (a) Schematic of the model, a spring-mass network with Lorentz-like force and active bath on each particle. (b-d) Averaged energy flux from numerical calculations for example networks. The flux direction and pattern can be controlled by the network geometry. In these figures, gray lines and dots represent the mechanical equilibrium structure of the network, and the size of arrows is proportional to the magnitude of the flux. The arrows are colored blue if it is counter-clockwise (CCW), red if clockwise (CW), and gray for fluxes not on the boundary. The numerical calculations were performed with all parameters set to 1.

The last two terms describe the active bath, which consists of friction $-\gamma v_i$ and an Ornstein-Uhlenbeck (OU) colored noise η_i [26]. The colored noise has finite correlation time τ with statistics

$$\left\langle \eta_i(t)\eta_j^T(t') \right\rangle = I\delta_{ij}\frac{\gamma T_a}{\tau}e^{-\frac{|t-t'|}{\tau}}, \tag{2.2}$$

where, for fixed τ, the parameter T_a controls the variance of the colored noise, and I is the identity matrix with appropriate dimensions. The time evolution of the OU noise can be described according to the following equation [26],

$$\tau\dot{\eta}_i = -\eta_i + \sqrt{2\gamma T_a}\xi_i, \tag{2.3}$$

where ξ_i is a delta function correlated white noise with unit variance. The friction $-\gamma v_i$ and OU noise η_i break fluctuation-dissipation relation, thus driving the system out of equilibrium. The active bath reduces to a thermal equilibrium bath in the $\tau \to 0$ limit.

Since the particles in our model are tethered to their lattice sites, rectification of fluctuations, if any, does not result in any particle flows. Rather, rectified fluctuations can affect the transport of energy. To study such phenomena, the observable we mainly focus on is the time-averaged energy flux between particles at steady state. For a system with pairwise interactions and on-site potentials, the energy flux $\left\langle J_{ij} \right\rangle$ from particle i to j reads

$$\left\langle J_{ij} \right\rangle = \left\langle \frac{1}{2}(v_j^T F_{ij} - v_i^T F_{ji}) \right\rangle = \left\langle v_j^T F_{ij} \right\rangle. \tag{2.4}$$

To arrive at this formula, we first define the energy of a particle as the sum of its kinetic energy, on-site potential energy, and one half of the bond energies [4]. Then we write down the energy balance relations using stochastic energetics [116]. Finally we identify the energy exchanged due to particle-particle interactions as the energy flux $\left\langle J_{ij} \right\rangle$ (derived in detail in Appendix A.1). We note that the energy flux can simply be interpreted as the rate at which work is done on particle j by particle i. Since this microscopic work is due to

particles' stochastic motions, rather than due to an external control, the energy flux can also be interpreted as a heat flux [116, 4]. The averaged energy fluxes Eq. (2.4) are identically equal to zero for a system at equilibrium with Boltzmann distribution.

Starting from the linear equations Eq. (2.1), (2.3), the energy fluxes can be solved numerically using methods introduced in Ref. [117, 118] (Appendix A.1). A collection of numerical results are shown in Figure 2.1b-d. We see nonzero energy rectification or energy fluxes can be generated in our chiral active system, and the flux direction or pattern changes with the network geometry. Using a linear response theory, we now develop analytical expressions for the energy flux that reveal how a combination of chirality, non-equilibrium activity, and network geometry is responsible for generating energy fluxes.

2.3 Linear response theory for energy flux

We begin by writing the equations of motion, Eq. (2.1), in frequency space,

$$\tilde{z}(\omega) = G^{+}(\omega)\tilde{\eta}(\omega), \tag{2.5}$$

$$G^{+}(\omega) \equiv [K + i\omega(\gamma I + BA) - m\omega^2 I]^{-1}\,. \tag{2.6}$$

Here, we have represented the displacement of all N particles using a $2N$-dimensional column vector $z = \sum_i |i\rangle \otimes z_i$, with $|i\rangle$ denoting the $2D$ subspace corresponding to particle i. $\tilde{z}(\omega)$ and $\tilde{\eta}(\omega)$ denote the Fourier transform of z and the OU noise η, respectively. G^{+} is the response matrix, in which matrix K encodes all on-site and spring forces F according to $F = -Kz$, and A is an antisymmetric matrix $A = \sum_i |i\rangle\langle i| \otimes A_1$. Eq. (2.5) describes how the displacement responds to the noise.

Following the procedure in Ref. [119], the flux defined in Eq. (2.4) can be expressed using

G^+ as a spectral integral (Appendix A.2)

$$\langle J\rangle = \int_{-\infty}^{\infty} \mathrm{d}\omega\, h(\omega) J^{FT}(\omega), \tag{2.7}$$

$$J^{FT}(\omega) \equiv -\frac{T_a k}{2\pi} \operatorname{Re}\operatorname{tr} G^+(\omega) A^{as}, \tag{2.8}$$

$$h(\omega) = \frac{1}{1+\omega^2\tau^2}, \tag{2.9}$$

where A^{as} is an antisymmetric matrix $A^{as} = -|i\rangle\langle j| \otimes e_{ij}e_{ji}^T + |j\rangle\langle i| \otimes e_{ji}e_{ij}^T$. The response function $G^+(\omega)$ has no pole in the lower-half complex plane, but the colored noise introduces one pole at $\omega = -i/\tau$. Using the residue theorem we get a compact expression for the energy flux (Appendix A.2)

$$\frac{\langle J\rangle}{T_a/\tau} = -\frac{k}{2}\operatorname{tr} G^+(-\frac{i}{\tau}) A^{as}. \tag{2.10}$$

Higher-order moments of the (integrated) energy flux can also be calculated, which we present in Appendix A.2.3.

Eq. (2.7) and (2.10) will serve as our starting point to understand the energy flux. While they contain all the information required to compute energy fluxes, they have limited utility as design principles. Indeed, as written down, they require that the flux be recomputed de novo for each new network geometry and non-equilibrium bath activity. In the next two sections, we show that it is possible to expand Eq. (2.7) and (2.10) in forms that reveals design principles for controlling energy fluxes.

As an aside, one important property that can be directly obtained from a similar linear response analysis is that the energy fluxes satisfy Kirchoff's law, $\sum_i \langle J_{ij}\rangle = 0$. The Kirchoff's law shows that on average there is no energy exchange between particles and the active bath. To derive the Kirchoff's law, we calculate the average heat exchange between particle i and the active bath $\left\langle v_i^T \eta_i - \gamma v_i^T v_i \right\rangle$, and following procedures in Ref. [119], this heat exchange can be shown to be zero (Appendix A.3). The Kirchoff's law puts a strong constraint on possible energy flux patterns between particles, and some corollaries immediately follow, such

as networks with no cycles cannot have nonzero flux, and fluxes of all bonds in a polygon network (as in Figure 2.1b) are equal.

Finally we note that Eq. (2.7) is distinct from a Harada-Sasa like relation [120] that connects the entropy production rate to the extent of violation of the fluctuation dissipation theorem. Indeed, when the B-field is turned off, the energy flux vanishes while the entropy production rate does not on account of the non-equilibrium active bath. For completeness, in Appendix A.4, we present a Harada-Sasa relation for our system.

2.4 Ingredients required for energy rectification

Compared with an ordinary thermal spring-mass network, which supports no energy fluxes in its equilibrium state, our active gyroscopic network contains two extra components, the Lorentz force and the correlation in the noise. We now show that these two components provide two necessary ingredients required to ensure energy rectification in our model. Next, we clarify the role played by the geometry of the network in controlling the energy flux.

2.4.1 Lorentz force and non-equilibrium activity are necessary for the generation of an energy flux

We begin with Eq. (2.7) that represents the averaged flux in terms of functions $J^{FT}(\omega), h(\omega)$. In particular, we note that the function $J^{FT}(\omega)$ is proportional to the energy flux at Fourier frequency ω in an isolated damped variant of our network while the function $h(\omega)$ is proportional to the the noise spectrum, $\left\langle \tilde{\eta}(\omega)\tilde{\eta}(\omega)^{*,T} \right\rangle = 2\gamma T_a I h(\omega)/t$.

To generate a nonzero flux, or equivalently make the integral nonzero in Eq. (2.7), we need two requirements (Figure 2.2). Firstly, $J^{FT}(\omega)$ should not be zero everywhere. In the absence of a magnetic field, $B = 0$, it can be easily shown that $J^{FT}(\omega) = 0$. Indeed, the response function G^{+} is symmetric or reciprocal when B is absent, and since A^{as} is antisymmetric, the trace $\mathrm{tr}\, G^{+}(\omega)A^{as} = 0$ at all values of ω. We note that the chirality of

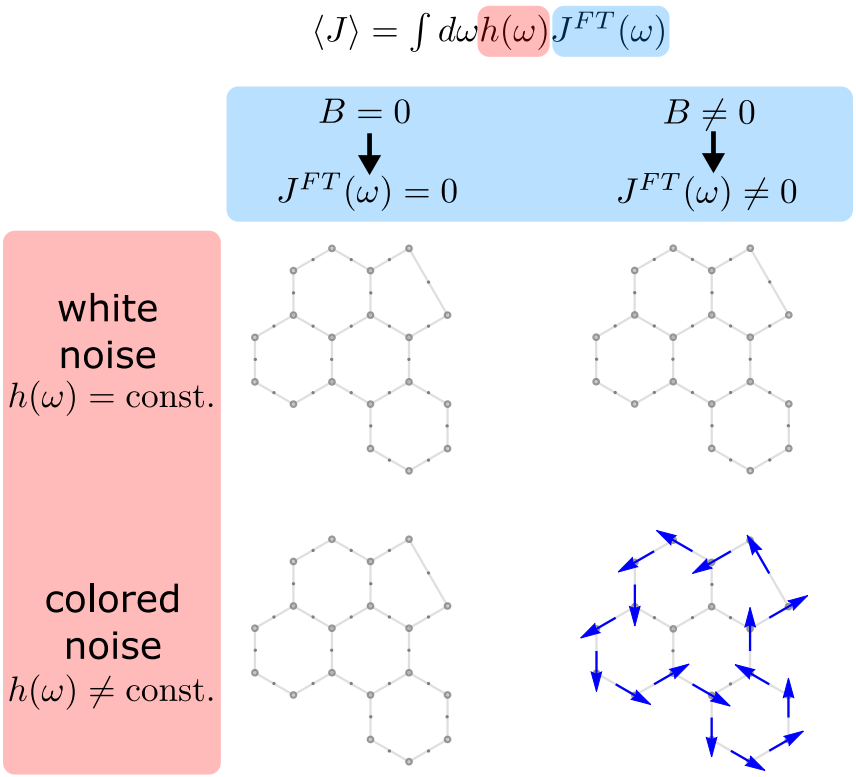

Figure 2.2: Necessary ingredients for generating nonzero energy fluxes. Both Lorentz-like force and colored noise are needed to generate nonzero fluxes. The role of Lorentz-like force is to provide chiral Fourier modes ($J^{FT}(\omega) \neq 0$). If $B = 0$, $J^{FT}(\omega)$ is zero everywhere. The role of colored noise is to provide weighted excitation $h(\omega) \neq$ const., which makes a non-vanishing averaged flux $\langle J \rangle$ possible. The numerical calculations were performed with $m, k_g, k, \gamma, T_a = 1$.

network geometry does not affect the reciprocity of the response matrix, i.e. chiral networks without B-field also leads to $J^{FT}(\omega) = 0$. Nonzero B breaks the reciprocity of G^{+}, and can thus generate a nonzero $J^{FT}(\omega)$.

Nonzero $J^{FT}(\omega)$ alone does not ensure a nonzero averaged energy flux, we further require that $h(\omega)$ not be constant. Indeed, noise characterized by a constant $h(\omega)$ function corresponds to fluctuation dissipation preserving white noise. In such cases, our model system would be in equilibrium even in the presence of a magnetic field according to the Bohr-van Leeuwen theorem [121]. Mathematically, if $h(\omega)$ is constant, the integrand in Eq. (2.7) has no poles in the lower-half ω-plane, because $G^{+}(\omega)$ is a linear response function, which satisfies causality. The absence of poles ensures that the flux integral vanish. A non-constant $h(\omega)$ function corresponding to a colored noise source can support a nonzero average energy flux through its introduction of poles. In this chapter, we focus on a specific choice of the colored noise, namely the OU colored noise. The spectrum of OU noise is a Lorentzian, $h(\omega) = 1/(1 + \omega^2\tau^2)$, which excites lower frequency modes with larger weights.

In summary, we see that B-field and a colored noise are two necessary ingredients to generate energy fluxes in our model chiral system. The role of the B-field is to break the reciprocity of response and generate Fourier modes such that $J^{FT}(\omega) \neq 0$. The role of the colored noise is to excite these modes in a weighted manner.

2.4.2 Energy flux can be tuned as a function of lattice geometry

Apart from the these two ingredients, the geometry of the network also plays an important role. Indeed the connection between the geometry and flux can be clearly seen in the small γ regime and with gyroscopic lattices that support chiral topological edge modes [112, 114]. In such systems, a non-zero value of $J^{FT}(\omega) \neq 0$ can be heuristically explained by exploiting the connection between the slightly damped isolated variants of our system and the undamped isolated gyroscopic metamaterials [112, 114]. Specifically, the slightly damped variant resonate near the eigen-frequencies of the undamped metamaterials, and hence ex-

hibit Fourier modes that are close to the eigenmodes of the undamped system. Consequently, non-zero values of the flux, $J^{FT}(\omega) \neq 0$ are possible as the corresponding eigenmodes in the undamped variant are chiral. As discussed in Ref. [112], the geometry of the network plays a crucial role in generating the chiral eigenmodes.

At larger γ's, the Fourier modes of our damped isolated variant are no longer close to the chiral eigenmodes of gyroscopic metamaterial. However, an emergent connection can still be built between energy fluxes in the active system and all the eigenmodes of a reference isolated system (Appendix A.5).

We end this section by noting that while the presence (or absence) of chiral topological edge modes in the underlying gyroscopic lattice can in some cases provide intuition for the energy flux, this connection cannot be used in general to predict or control the energy flux in our non-equilibrium system. The breakdown in correspondence is mainly due to the friction imposed in our dynamics and the broad excitation of modes by the active noise. In the next section, we address the issue of predicting and controlling fluxes in arbitrarily complex non-equilibrium networks. To this end, we show that the above derived (seemingly non-local) expressions for the energy flux can be rewritten using a diagrammatic expansion.

2.5 A diagrammatic approach to compute the energy flux

In this section, we develop a diagrammatic technique which provides a simple intuitive method to compute energy fluxes and elucidates the relationship between flux and network geometry. The diagrammatic technique is constructed by expanding the expressions for the energy flux Eq. (2.10) in small-k regime and shows how the energy flux across a bond can be expressed as a sum over paths traversed along the network (Eq. (2.11)). Our perturbation theory assigns a geometry dependent pre-factor for each path, thus elucidating the role played by network geometry in ensuring rectified energy fluxes (Eq. (2.14)). Together, the central results of this section, summarized in Eq. (2.11), (2.14), provide compact expressions that elucidate how geometry, B-field, and correlation time τ of the colored noise can combine to

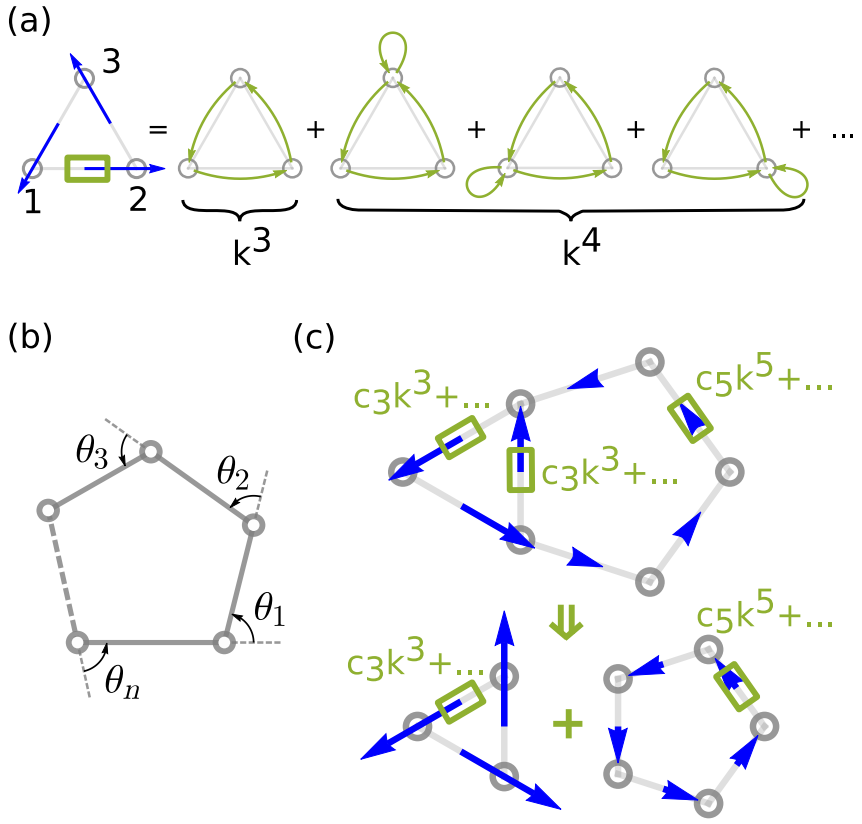

Figure 2.3: Illustrations of our diagrammatic technique. (a) Flux from site 1 to 2 can be calculated by summing over diagrams. Each diagram is a closed path, which pictorially represent one term in the small-k expansion. Paths are depicted using green arrows. The magnitude of path of length n is on the order of k^n. (b) Schematic of a polygon path and its outer angles $\theta_1, \theta_2, \ldots, \theta_n$. The flux of this diagram is simply Eq. (2.14). (c) For flux in complex networks, the leading order term is determined by the shortest cycles. Flux in the triangle part has order k^3, and the pre-factor c_3 is the same as that in a standalone triangle network. Likewise for the pentagon part. As a result, the flux in a complex network can be viewed as a combination of fluxes in its constituent cycles.

generate energy flows in networks with arbitrarily complex geometry and topologies. The lowest order expansion in Eq. (2.14) demonstrates for instance how the parameter α that captures compactly the combined effect of activity, the B-field, couples with the geometry of the lattice to power the flow of energy. The diagrammatic expansion, even at the lowest order, hence results in a concrete design principle for controlling the rectification of the energy by our metamaterial.

2.5.1 Diagrammatic expansion and the path rules

The starting point of the diagrammatic approach is the flux formula Eq. (2.10). First we expand matrix $G^+(-i/\tau)$ to different orders in the spring constant k, then the block-matrix structure of each term in the expansion enables further decomposition into paths, and the structure of matrix A^{as} closes these paths into cycles (Appendix A.6.1). In the final result, we write the total flux as a sum over the flux of closed paths (Figure 2.3a),

$$\frac{\langle J\rangle}{T_a/\tau} = \sum_l J_l^{\text{path}} = \sum_l \frac{1}{2}(S_l - S_{-l}), \tag{2.11}$$

$$S_l = (\frac{k}{k_0})^n \operatorname{tr} R_\alpha(-K_s)_{il_n} \cdots R_\alpha(-K_s)_{l_3 j} R_\alpha(-K_s)_{ji}. \tag{2.12}$$

Valid paths for flux from site i to j are $l : i \to j \to l_3 \to l_4 \to \cdots \to l_n \to i$, where l_a and l_b either has to be bonded or $l_a = l_b$. Paths that contain equal numbers of $i \to j$ and $j \to i$ do not contribute (e.g. path $i \to j \to i$), because either the path itself vanishes or it cancels with another valid path. As a consequence, paths are closed cycles (details in Appendix A.6.2).

The other terms in Eq. (2.12) are explained as follows. For each path l, we need to calculate the expression S_l as defined in Eq. (2.12). In this definition, $k_0 \equiv \sqrt{(k_g + \frac{\gamma}{\tau} + \frac{m}{\tau^2})^2 + (\frac{B}{\tau})^2}$ sets a characteristic scale for spring constant k. $R_\alpha \equiv \begin{pmatrix} \cos\alpha & -\sin\alpha \\ \sin\alpha & \cos\alpha \end{pmatrix}$ is a rotation matrix,

where the angle α is defined as

$$\alpha \equiv \arcsin \frac{B/\tau}{k_0}. \tag{2.13}$$

We note that this single angle α encodes information from all the parameters, $m, k_g, k, B, \gamma, \tau$, (except for T_a which simply sets the energy scale) in a condensed manner. The matrix $(K_s)_{l_b l_a} \equiv \langle l_b | (K - k_g I) | l_a \rangle / k$ is a 2×2 submatrix for calculating the non-dimensionalized spring force on particle l_b due to the displacement of l_a. $-l$ means l in the reverse order. The interval of convergence depends on the geometry of the whole network as well as the condensed parameter α. The values of the upper bound of k/k_0 for many networks range between 0.3 and 0.6 (details in Appendix A.6.2).

The paths can be pictorially represented by diagrams, from which the flux J_l^{path} can be calculated easily. For instance, the first diagram in Figure 2.3a represents the path $1 \to 2 \to 3 \to 1$. To calculate S_l, one writes down $(-K_s)_{l_b l_a}$ for each arrow $l_a \to l_b$, R_α for each node l_a, then multiply these matrices in the reverse order, and calculate the trace, e.g. $S_{1\to2\to3\to1} = (k/k_0)^3 \operatorname{tr} R_\alpha(-K_s)_{13} R_\alpha(-K_s)_{32} R_\alpha(-K_s)_{21}$. To get S_{-l}, one takes the result of S_l and replace α by $-\alpha$ (Appendix A.6.2). Finally, J_l^{path} can be calculated from the difference between S_l and S_{-l}.

Without explicit calculation of the diagrams, we can immediately see one useful property from Eq. (2.12) and the form of $(-K_s)_{ji}$ (Appendix A.6.1). If a diagram contains no loops (e.g. $l_a \to l_a$) on a node, then the diagram can be simplified by removing the node's all other neighbors which do not form arrows with the node. Taken together with the scaling factor $(k/k_0)^n$, the diagrammatic expansion hence reveals a hierarchical structure of the energy transport, starting from lowest-order diagrams that only depend on local structures of the network (non-local nodes are removed in simplified diagrams), to higher-order diagrams that involve more and more non-local structures.

2.5.2 Diagrammatic decomposition of the energy flux reveals connections between geometry, activity and rectification, and explains localization of energy flux in certain lattice geometries

To illustrate how the diagrams clarify the connection between geometry, activity and rectification, we consider the generic dominant lowest-order diagrams, which are polygonal cycles with no loops. The flux from Eq. (2.11) for these polygon paths reduces to a simple form (Appendix A.6.3)

$$J^{\text{path}}_{\text{polygon}} = \frac{1}{2}(\frac{k}{k_0})^n(\prod_i \cos(\theta_i - \alpha) - \prod_i \cos(\theta_i + \alpha)), \tag{2.14}$$

where α is defined in Eq. (2.13), n is the number of nodes and θ_i's are outer angles of the polygon (Figure 2.3b). Eq. (2.14) illustrates how the flux results from a combination of the geometry of the network, as characterized by angles θ_i, together with the condensed parameter α that encodes the nonreciprocity due to B-field and the violation of fluctuation dissipation due to the colored noise. It is surprising to see that the many-body effect can be expressed in such a compact manner. As a consistency check, the flux from Eq. (2.14) should vanish in the limit of zero τ, to be consistent with the expected equilibrium behavior. If m is finite, as τ tends to zero, the parameter $\alpha \to 0$, consequently $\langle J \rangle \to 0$. If we take $m \to 0$ first, as τ reduces to zero, α remains finite. However, we still get $\langle J \rangle \to 0$ due to its vanishing pre-factor, $\langle J \rangle \propto 1/\tau k_0^n \sim \tau^{n-1}$.

For complex networks (e.g. Figure 2.1c-d), Eq. (2.14) implies that its lowest-order flux can be viewed as a result of combining the flux of its constituent polygons, as illustrated in Figure 2.3c. From the property stated at the end of the last subsection or from Eq. (2.14), polygon diagrams are not affected by any side chains on its nodes, thus $J^{\text{path}}_{\text{polygon}}$ for a polygon in a complex network is the same as $J^{\text{path}}_{\text{polygon}}$ for the polygon when standalone.

The diagrammatic approach when applied to complex networks can explain the various emergent flux patterns seen in numerical calculations. In the example of ordered honeycomb

networks (Figure 2.1c), fluxes are localized at the boundary of the network, which can be explained as follows. The lowest-order diagram for a bond at the boundary is one hexagon path, which contribute a flux on the order of k^6. In contrast, the lowest-order diagrams for a bond in the bulk are two paths each traverses the hexagon on one side of the bond. The contribution from these two diagrams cancel each other, thus the flux on the order of k^6 is zero. Contributions from higher order diagrams persist however and show that the flux exhibits an exponential decay into the bulk. The decay length can be expressed analytically in the small-k limit using the diagrammatic approach (Appendix A.6.4). We clarify that such localization is not a general feature for all crystalline networks. As a counter-example, the kagome lattice supports fluxes also in its bulk in the triangle units.

In the example of disordered networks (Figure 2.1d), fluxes are generated throughout the network. This is because each unit polygon is different, and there is no cancellation of diagrams. The non-cancellation effect is stronger when neighboring polygon units have different number of sides, which would contribute to diagrams on different orders in k.

If one is able to sum over all the diagrams to all orders, an exact result can be obtained. This result holds beyond the small-k regime due to analytic continuation. One example is the $1D$ network, where we can show that all diagrams vanish in Appendix A.6.5. Another example is shown in Sec. 2.7.1.

2.5.3 Generalization of the diagrammatic approach to higher-dimensional networks, generic noise spectrum, and heterogeneous parameters

We have seen how the diagrammatic approach reveals a hierarchical picture of the energy transport (Eq. (2.11)) and elucidates how the Lorentz force and activity, operating through the condensed parameter α, interact with the geometry to enable rectification (Eq. (2.14)). Together these results make possible the control of energy fluxes in arbitrarily complex networks.

We now show that the diagrammatic approach can enable control in a wider variety of

systems. Our results can immediately be generalized to networks on $2D$ curved surfaces or to $3D$ networks. For $2D$ curved surface, the same diagrammatic expressions Eq. (2.11)-(2.14) can be readily applied. Curvature simply modifies the relation between outer angles θ_i and the number of sides n in a polygon path. For $3D$ networks, the same diagrammatic approach applies, but the expression would be modified by the additional spatial dimension. Examples of networks on $2D$ curved surface or in $3D$ space are shown in Appendix A.7.1.

The OU noise can also be generalized to noises with spectrum $\left\langle \tilde{\eta}(\omega)\tilde{\eta}(\omega)^{*,T} \right\rangle = 2\gamma T_a I h(\omega)/t$. The diagrammatic approach still applies, except now the real matrix $G^+(\omega = -i/\tau)$ is replaced by the complex matrix $G^+(\omega)$. As a result, the path rules remain unchanged, but the mathematical expression corresponding to the diagrams are modified. In Appendix A.7.2, we show a diagrammatic expansion of $J^{FT}(\omega)$. Consequently the flux can be expressed as weighted diagrams integrated over ω or evaluated at the poles.

The diagrammatic approach also be extended to predict energy fluxes in heterogeneous networks where all parameters except for those related to the colored noise, i.e. T_a and τ, can be modulated as a function of the position of nodes. In this case, the only modifications to the polygon diagram Eq. (2.14) are replacing k^n with $\prod_i k_i$ and replacing $\prod_i \cos(\theta_i - \alpha)$ with $\prod_i \cos(\theta_i - \alpha_i)$. Similar replacements can be performed for general diagrams Eq. (2.12).

2.6 Energy flux in a passive segment coupled to an active network

A canonical setup for the study of energy transport is a passive material bar placed between tho heat reservoirs held at constant temperature (Figure 2.4a). The generic result is that energy flows from the 'hot' reservoir to the 'cold' reservoir, and in the absence of a temperature difference there can be no net energy flux through the bar.

Placing a passive material bar—in this case three masses not influenced by any magnetic fields and connected by springs in a linear geometry—across a gap in our activated meta-

material, as illustrated in Figure 2.4a, reveals a very different behavior: despite the absence of temperature gradients a persistent energy flux is measured through the passive material bar. From numerical calculations (method is described in Appendix A.8), the magnitude of the energy flux decays exponentially with the bar length. In the small k limit, the flux in a bar with n sites can be evaluated using the diagrammatic techniques developed in the previous section, which yields $\langle J \rangle_n = \langle J \rangle_1 \left(k/(k_g + m/\tau^2)\right)^{(n-1)}$. Using numerical simulations, we plot the instantaneous flux transmitted across the bonds on the passive segment in Figure 2.4b. The instantaneous flux exhibits stochastic fluctuations. Large values of the instantaneous flux are transmitted across bonds sequentially in a wave-like manner (Figure 2.4b). This is reflected in the successive peaks in the instantaneous flux profile across the bonds of the passive segment. The spacing between the peaks matches the sound speed in the passive chain.

This result, in combination with the results of the previous sections, shows how one design active gyroscopic metamaterials that can act as energy pumps and support energy transport in passive materials even in the absence of any temperature gradients. Crucially, these results demonstrate how gyroscopic metamaterials can rectify non-equilibrium fluctuations. In the following section, we consider whether these rectified fluctuations when placed in contact with a viscous fluid, can act as low Re swimmers or fluid pumps [122, 123, 124].

2.7 Non-reciprocal motions responsible for energy fluxes can be used to generate forces

The rectification of energy has been our main focus so far. In this section, we show that it is possible to exploit the energy flux to rectify motions when our model systems are allowed to interact with a viscous fluid (Figure 2.5a). We begin by considering the motion of the three masses in the passive material bar discussed in the previous section and in particular, consider the effect that their motion would have on a viscous fluid. We first do so by taking

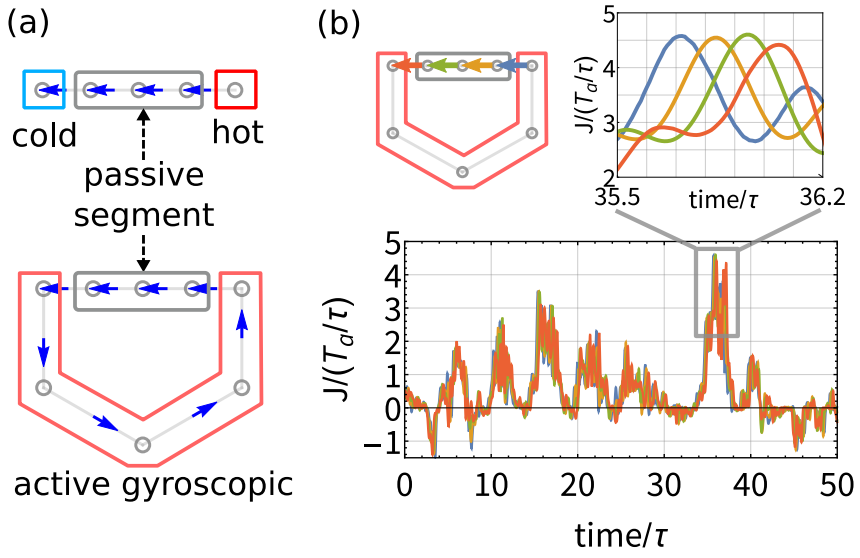

Figure 2.4: Driving energy through a passive chain. (a) Conventional energy transport in a passive material (boxed in gray) with temperature differences at two ends. Similarly, the active gyroscopic network can also drive energy flows through a passive segment. (b) Instantaneous energy flux J through bonds in the passive segment from a simulation. Flux through different bonds are colored differently. J is stochastic in general, however, during the period when J is large, J exhibits successive peaks in accordance with the direction of the flux. In the simulation setup, parameters for the active particles are: $m, k_g, \gamma = 0.1, k = 10, B, T_a, \tau = 1$. Passive particles (boxed in gray) are constrained to 1D, and their γ, T_a, k_g are set to 0.

their recorded trajectories and asking whether three particles following these trajectories would 'swim' in an external fluid.This calculation ignores any back action from the fluid on the dynamics of the segment. We then consider the effect of these forces in Sec. 2.7.2 and discuss regimes in which our energy conducting passive segment can generate forces when immersed in a viscous fluid. Together, these results demonstrate how a gyroscopic active metamaterial can be manipulated to exert forces and power motion in nanoscale materials.

2.7.1 Nonreciprocal motion as a swimming protocol

In this section we consider a system of three spheres arranged in a linear configuration [124] (Figure 2.5a(iii)), placed in a viscous fluid. This system is a minimal model for low Reynolds number swimming/pumping action. If the lengths of the two springs connecting the spheres, $L_1(t) = L + \Delta L_1(t), L_2(t) = L + \Delta L_2(t)$ are varied according to some prescribed protocol, the time-averaged swim speed is (Eq. (12) in Ref. [124])

$$V_s = \frac{7a}{24L^2}\left\langle \Delta L_1 \frac{\mathrm{d}\Delta L_2}{\mathrm{d}t} - \frac{\mathrm{d}\Delta L_1}{\mathrm{d}t}\Delta L_2 \right\rangle, \tag{2.15}$$

where a is the radius of the bead. Assumptions for this equation are $a/L \ll 1, \Delta L_i/L \ll 1$, and total external force on the swimmer is zero.

We now imagine recording the motions of the passive segment when it is connected to our active gyroscopic metamaterial as in Sec. 2.6(Figure 2.5a) and not coupled to a viscous fluid. This recorded motion can be used a protocol for modulating the configuration of an equivalent *swimmer* passive segment that is placed in a viscous fluid. We compute the swim speed of the swimmer using Eq. (2.15) and find that it is in fact proportional to the energy flux conducted through the passive segment when it is coupled to the chiral active network (Figure 2.5b). The nonreciprocal motions that is responsible for energy fluxes can also be used as a protocol to generate motion in a low Re fluid. The proportionality constant between the swim speed V_s and the energy flux $\langle J \rangle$ can be calculated using a modified diagrammatic

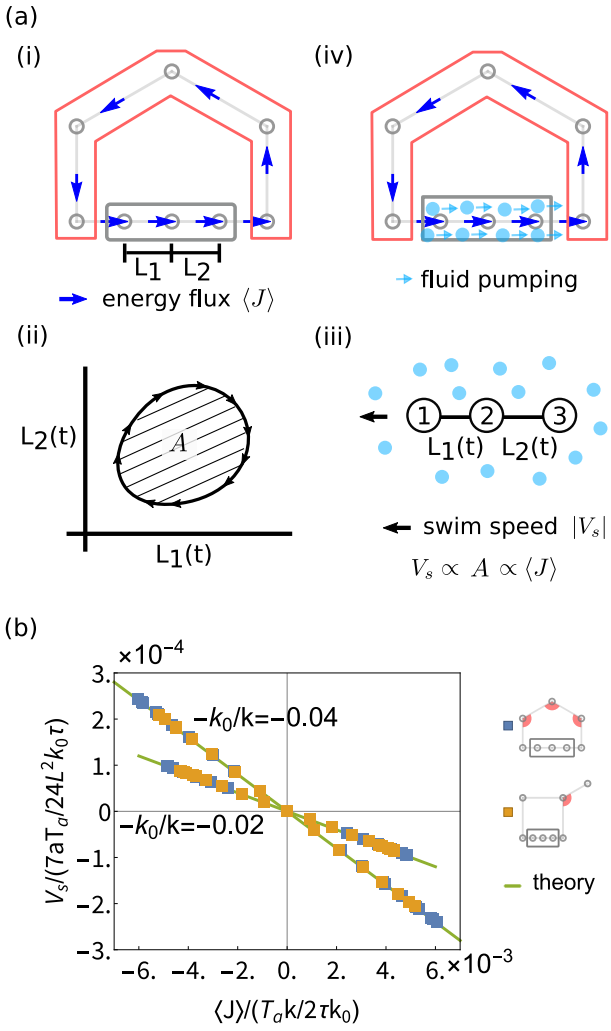

Figure 2.5: Utilization of non-equilibrium gyroscopic dynamics to power swimming and pumping in low Reynolds number (Re) media. (a) The energy flux in the active gyroscopic network is accompanied by nonreciprocal motions of the particles (i,ii). The nonreciprocal motion is a schematic for illustration purposes, and the real data is much more noisy. Using these nonreciprocal motions as input, a three bead linear object can be made to swim through a low Re medium (iii). Our analytical results in (b) below show that the swim speed V_s is in fact proportional to the energy flux $\langle J \rangle$. (iv) Finally by immersing the passive segment into a low Re fluid, the nonreciprocal motions can be used to pump the fluid. In this manner, the energy fluxes can be rectified for locomotion and force generation. (b) Swim speed V_s is proportional to the energy flux $\langle J \rangle$ in the active network. The proportionality constant is $-k_0/k$, which is independent of the network geometry. The series of dots for each $-k_0/k$ are obtained by varying the labelled angles (by red disk sectors) in pentagon networks or "square+tail" networks. The parameters chosen for the numerical calculations are $m, k_g = 0.1$, $\tau = 1$, $k = 5$ for $k_0/k = 0.04$ and $k = 10$ for $k_0/k = 0.02$. For the active part, $\gamma = 0.1, B, T_a = 1$. For the passive segment, $\gamma, B, T_a = 0$.

technique (Appendix A.9),

$$\frac{V_s}{7a/24L^2} = -\frac{k_0}{k}\frac{\langle J\rangle}{k/2}, \tag{2.16}$$

where $k_0 = k_g + m/\tau^2$ ($B, \gamma = 0$ for the passive segment). This result Eq. (2.16) holds beyond small-k regime because all orders of diagrams are considered. Figure 2.5b and Eq. (2.16) together establish that one can relate the swim speed to the flux of energy in the gyroscopic metamaterial. Similar proportionality between V_s and $\langle J\rangle$ can be expected for other types of three-sphere swimmers, such as one where one sphere is much larger than the other two [125]. This is because the swim speed is generically proportional to the area enclosed in the ΔL_i space [126]. This area is also proportional to the energy flux $\langle J\rangle$ (Appendix A.9).

2.7.2 Force generation in a viscous medium using the rectified energy fluxes

Finally, we now consider the scenario where the passive segment, which is connected to the active network, is immersed in a fluid (Figure 2.5a(iv)). Since the passive segment is tethered due to k_g and its connection to the active network, it cannot swim indefinitely. However, a stalled swimmer can potentially pump the fluid [127]. We now analyse the regime for parameters where this pumping is possible. In order to utilize the connection between the swim speed and energy flux, we require that the fluid minimally perturbs the dynamics of the passive segment. Such a regime requires the dissipation rate due to the viscous fluid to be much smaller than the energy flux through the segment. This condition can be expressed as $\eta_f a v^2 \ll J$, where v is the characteristic velocity of a bead in the passive segment, η_f is the dynamic viscosity of the fluid, and J is the energy flux in the absence of the fluid. In addition, the constraint of low Reynolds number requires that $Re = \rho_f a v/\eta_f \ll 1$, where ρ_f is fluid's density. Writing these two conditions together, the requirement reads $J \gg \eta_f a v^2 \gg \rho_f a^2 v^3$. Here, we have ignored the effect of hydrodynamic interactions between the beads to their dynamics generated from springs, because it is a perturbation on the order of a/L.

As a numerical example, these conditions can be satisfied by setting $k = 10^{-5} kg/s^2, k_g =$

$10^{-6}kg/s^2$ for springs (values of optical traps [127]), $a = 10^{-6}m$ for all Silica beads (size used in Ref. [127]), $T_a = 10^{-18}J, \tau = 1s$ for the active bath [34], $\rho_f = 10^3 kg/m^3, \eta_f = 10^{-3}kg/(m{\cdot}s)$ for liquid (water), and $B = 2{\times}10^{-6}kg/s$ for the B-field (note that our notation of B has absorbed the charge factor). For these parameters, we obtain $v = 6{\times}10^{-7}m/s$, and the three relevant scales $J = 4 \times 10^{-20}J/s, \eta_f a v^2 = 4 \times 10^{-22}J/s, a^2 v^3 \rho_f = 2 \times 10^{-28}J/s$, which indeed satisfy $J \gg \eta_f a v^2 \gg \rho_f a^2 v^3$. If the separation between beads is $L = 10a$, the swim speed calculated from Eq. (2.16) is $2 \times 10^{-12}m/s$. The swim speed can provide an estimate of the potential speed at which the fluid can be pumped due to the energy fluxes. This speed can be potentially scaled up by increasing T_a or tuning other parameters. We note the extremely high value of the B-field required to generate a sizable averaged flux $\langle J \rangle$. To make practical use of this model, we anticipate that it will become necessary to instead consider models with interacting gyroscopes [112] or Coriolis forces [128]. Large B-field or Lorentz force analogues are easier to achieve in these cases.

The results of this section show that the energy fluxes generated by our active gyroscopic metamaterial can be used to rectify motion and generate forces on the nanoscale. Our calculations also show how the forces generated by our metamaterial are in fact proportional to the energy fluxes. Hence, together with the results from the previous sections that show how energy fluxes in arbitrarily complex active metamaterial networks can be controlled, our results provide a broad framework to generate and modulate forces using active gyroscopic metamaterials.

2.8 Conclusion

In conclusion, we have established a general set of design principles for rectifying energy and motion in non-equilibrium parity violating metamaterials. In particular, our central results show how a combination of time reversal symmetry violation due to the geometry, interactions and Lorentz forces in the metamaterial, and due to the non-equilibrium fluctuations of the active bath, can result in a general strategy for rectification of energy and

motion. Extending these ideas to non-equilibrium parity violating metamaterials with non-linear interactions or materials composed of active chiral particles can potentially lead to new strategies for the construction of synthetic molecular motor analogues. These ideas will be considered in future work. The applications we have shown in the last two sections are based on the conventional picture of transport between two terminals. However, since our setup places all nodes on a equal footing [65, 66, 67] and enables complex transport patterns in many-body networks, we can expect applications beyond the two-terminal picture.

CHAPTER 3

ENERGY RECTIFICATION IN ACTIVE GYROSCOPIC NETWORKS WITH TIME-PERIODIC MODULATIONS

3.1 Introduction

Pioneering studies on energy rectification have shown how energy fluxes can be generated in the absence of temperature biases [51, 52, 56, 57, 61, 55, 110, 58, 59, 60, 65, 66, 67]. Such principles can potentially be applied to build nanoscale energetic rectifiers [55]. From a theoretical perspective, energy transport is usually associated with phonons, but these collective excitations are more difficult to manipulate compared with single particles [55, 14]. Previous studies have exploited opportunities provided by nonlinear interactions [57], athermal baths [52] or geometric phases from adiabatic modulations [61]. In this chapter, we uncover new rectification principles provided by a combination of parity-breaking metamaterials, nonequilibrium forcing and time-periodic modulations. Unlike many previous studies that focused on transport between two terminals which are linked directly [57] or through an asymmetry segment [52, 56, 57], our setup places all nodes and their connections on a equal footing [65, 66, 67], thus providing the possibility of rectification in networks with complex geometries.

Our model system is a class of spring-mass networks where each mass is subject to Lorentz force [112, 114] with a time-periodic B-field, and is immersed in an active bath [26]. The unmodulated invariant of this model was discussed in Chapter 2, which is able to rectify energy fluxes between nodes but unable to generate net transport between nodes and the bath. In this chapter, we modulate the B-field in a time-periodic manner. Using numerical calculations, we show that the time-modulated system is able to rectify energy fluxes between nodes and the bath. In other words, despite the absence of temperature biases, there is energy pumping from some nodes to the others.

We capture the numerical results by developing an analytic framework to understand the

energy rectification in time-modulated complex networks. We first expand the energy transport with respect to the modulation amplitude using the Martin–Siggia–Rose / Janssen–De Dominicis–Peliti (MSR/JDP) path integral formalism [129, 130, 131], which reveals a coupling between different Fourier modes of the flux induced by the time-periodic modulation. We further perform a diagrammatic expansion using techniques we developed in Chapter 2. Taken together, our theoretical results provide a connection between rectification in complex networks and the structures of local subnetworks. The rectification principle can potentially be applied to control energy transport in complex environment. Note that "energy flux" in this chapter refers to energy transferred between the node and the bath during each modulation period, which is distinct from the energy flux between two nodes as explored in Chapter 2.

The remainder of this chapter is organized as follows. In Sec. 3.2, we introduce our time-modulated active gyroscopic model, provide a microscopic definition for the energy flux, and present numerical results. In Sec. 3.3-3.5 we develop a theoretical framework for the energy flux that combines path integral formalism and a diagrammatic approach. In Sec. 3.6 we compare theory with numerical results. In Sec. 3.7 we utilize the rectification principle to create flux patterns.

3.2 Model systems and energy flux

Our model gyroscopic network is a tethered spring-mass network in which each particle is subject to a Lorentz-like force and stochastic forcing from an active bath (Figure 3.1a). The equations of motion are

$$m\dot{v}_i = -k_g z_i + \sum_j F_{ji} - B(t)A_1 v_i - \gamma v_i + \eta_i, \tag{3.1}$$

$$\left\langle \eta_i(t)\eta_j^T(t') \right\rangle = I\delta_{ij}\frac{\gamma T_a}{\tau}e^{-\frac{|t-t'|}{\tau}}, \tag{3.2}$$

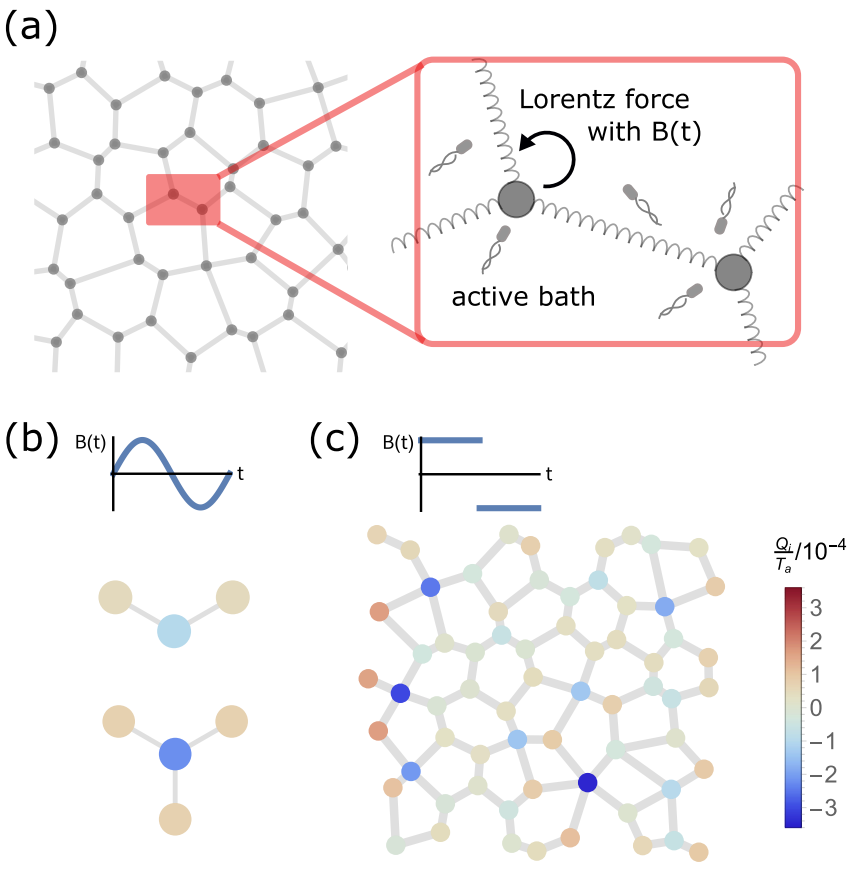

Figure 3.1: The model and energy flux in example networks. (a) Schematic of the model, a spring-mass network where each particle is subject to a time-modulated Lorentz-like force and active bath. (b) Energy transferred during each period, Q_i, for networks with shape V and Y. Positive value corresponds to net energy transferred from the bath to the node. Protocol for B-field modulation is $B(t) = \sin 2\pi t/T$, where T is the period of modulation. (c) Energy flux for disordered network subject to a step function protocol $B(t) = 1$ if $t < T/2$, $B(t) = -1$ if $t \geq T/2$. Numerical calculations were performed with all parameters set to 1.

where all symbols adopt the same meanings as those in Chapter 2, introduced below Eq. (2.1). Compared with the active gyroscopic network model introduced in Chapter 2, this model allows the B-field to be time-dependent, more specifically time-periodic. As a result of the periodically modulated B-field, the system would reach a time-periodic steady state.

The observable we focus on is the energy transport between particles and baths at the time-periodic steady state. For a system with pairwise interactions and on-site potentials, the energy transferred from bath to particle i accumulated in each period T, averaged over noise realizations, reads

$$Q_i = \int_0^T \mathrm{d}t \left\langle -\gamma v_i^T v_i + v_i^T \eta_i \right\rangle . \tag{3.3}$$

The first term on the RHS measures the energy loss from the particle to the bath due to friction or dissipation. The second term measures the the energy gain for the particle due to fluctuating forcing from the bath. A detailed procedure for deriving Eq. (3.3) is provided in Appendix A.1 using stochastic energetics [132, 116]. We note that Appendix A.1 was developed for the case with constant B-field, however the same procedure also applies to the time-dependent situation. The reason is because the Lorentz force, whether time-dependent or not, does not perform work on the system, thus it does not directly affect the energy or energy transport.

Under the time-periodic modulation, the system would reach a time-periodic asymptotic or steady state. The immediate consequence of such time-periodicity is that the total energy transfer during each period is zero, $\sum_{i=1}^{N} Q_i = 0$, where N is the number of particles in the system. In nonequilibrium conditions, there seems to be no further constraint on the value of each Q_i, thus there is possibility that individual Q_i's are nonzero. Nonzero Q_i's mean that energy is rectified or pumped from some sites to the others.

Starting from the linear equations for particles Eq. (3.1) and for the Ornstein-Uhlenbeck (OU) noise Eq. (2.3), we numerically solve the time-dependent covariance matrix, from which we calculate Q_i [117, 118] (Appendix B.1). Figure 3.1b shows a collection of numerical results for small and larger networks under two example protocols for $B(t)$, a sinusoidal function

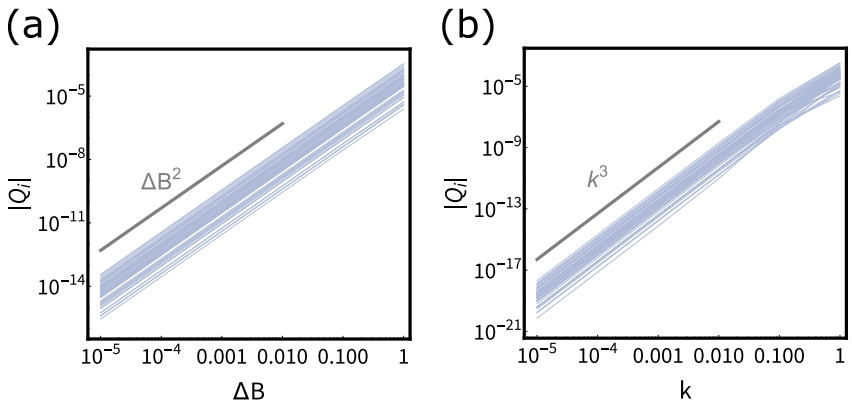

Figure 3.2: Scaling of energy flux with respect to (a) ΔB and (b) k in for the disordered network in Figure 3.1b. We have separated the modulation $\Delta B(t)$ into an amplitude part ΔB and a time-dependent part. Each single curve is the scaling for one node. Numerical calculations were performed with all other parameters set to 1.

and a step function. We see that nonzero energy is pumped from some sites to the others. A more detailed description of the average (but not dynamical) picture is as follows, energy is transferred from bath to particles with $Q_i > 0$, transmitted through the network and released from particles with $Q_i < 0$ to their surrounding baths. If we were to view this phenomenon from the perspective of conventional temperature-driven transport, we see that although all particles experience the same bath or environment, some sites appear *as if* they were hotter ($Q_i > 0$) or colder ($Q_i < 0$).

In the next three sections we develop a perturbation theory to understand the energy pumping mechanism and how the energy pumping depends on the local structure of the network.

3.3 An overview of the theory: a two-step perturbation strategy

We would like to utilize the diagrammatic approach developed in Chapter 2 for its explanation power. However, the central quantity for the diagrammatic approach, the response matrix, does not directly apply to the time-dependent case discussed in this chapter. To overcome this obstacle, we develop a two-step perturbative expansion. In the first step, we

write the time-modulated B-field as $B(t) = B + \Delta B(t)$, where B is a time-independent reference field and $\Delta B(t)$ is a time-periodic modulation with a perturbative amplitude. Using the Martin–Siggia–Rose/Janssen–De Dominicis–Peliti (MSR/JDP) path integral formalism [129, 130, 131], correlators under time-periodic system can be expressed in terms of correlators under a time-invariant reference system. We will see in Eq. (3.24) that the response matrix at different Fourier frequencies are coupled, whereas the modulation $\Delta B(t)$ at different modes in Fourier series do not couple. In the second step, we perform an expansion with respect to interactions or the spring constant. Using a diagrammatic approach, we are able to express the energy transfer as intuitive diagrams, which then reveals how the energy flux in complex networks can be related to properties of local subnetworks.

Numerical results in Figure 3.2 show that the lowest order scaling of Q_i with respect to $\Delta B(t)$ and k is $Q_i \propto \Delta B(t)^2 k^3$. These observations suggest a goal for analytical efforts, which is to develop an expression to the order of $\Delta B(t)^2 k^3$, explore properties of energy pumping on this order, as well as explain why lower order terms vanish. We also observed higher orders in $\Delta B(t)$ or in k for nodes in networks with specific symmetries. These observations are special cases and thus are not our focus.

In the literature, there exists other theoretical approaches to time-periodic systems, notably the geometric phase formulation for adiabatic processes [62, 63, 64, 133, 61], and the Floquet formalism [134, 135, 136]. These methods are less appropriate for our system for the following reasons. Our energy pumping is not an adiabatic process, because the modulation is not slow, thus the geometric phase formulation cannot be applied. In the adiabatic limit, a nonzero pumping requires time-modulation of at least two parameters [62, 61], whereas we only modulate one, the B-field. In Appendix B.2 we show that the energy pumping indeed vanishes in the adiabatic limit. The Floquet formalism generally requires solving eigenvalue problems, thus does not meet our goal to develop analytic results. A rare case where analytic results can be obtained is the OU processes with additive modulations [134], which does not apply to our case with multiplicative modulation (through $B(t)v_i$).

3.4 Perturbative expansion in modulated B-field: a MSR/JDP approach

In this section, we first review the MSR/JDP formalism, apply it to our system, and arrive at an expression that relates correlators in the time-modulated system to correlators in the reference system with constant B-field (Eq. (3.9)). Next we assume weak modulations and expand around small amplitude of $\Delta B(t)$ to its second order. We will show that the first order term vanishes. Finally we come to the central result of this section, the expression for energy flux on the order of ΔB^2 (Eq. (3.24)).

3.4.1 The MSR/JDP path integral formalism

The Martin–Siggia–Rose/Janssen–De Dominicis–Peliti (MSR/JDP) path integral formalism [129, 130, 131] is a powerful framework for studying statistical properties of a stochastic trajectory when compared to another trajectory. In our case, these two trajectories are one with modulated B-field, and one with constant B-field. As another example, in stochastic thermodynamics, the evaluation of entropy production involves the ratio between the forward and the reverse trajectory [107]. By introducing an auxiliary response field, the MSR/JDP framework expresses observable in forms of polynomials under the reference trajectory, which is then ready for perturbative treatments.

To distinguish between notations of observable O averaged under modulated systems and under unmodulated system, we denote the former as $\langle O \rangle_{B_t}$ and the latter as $\langle O \rangle$. We express the N-particle system with $2N$-dimensional column vectors. The notation has been introduced below Eq. (2.6).

The probability of a trajectory $\{z, v, \eta\}$ under $B(t)$ reads

$$\mathcal{P}_{B_t}[z, v, \eta] = \mathcal{N} \prod_t \delta(\dot{z} - v)\delta(m\dot{v} + Kz + \gamma v + B(t)Av - \eta)\mathcal{P}[\eta], \tag{3.4}$$

where $\mathcal{N}$ is a normalization constant and $\mathcal{P}[\eta]$ is the probability for the noise.

Introducing a response field $iu = \sum_i |i\rangle \otimes iu_i$ through $\delta(x) \propto \int \mathrm{d}u\, e^{-iu\cdot x}$ (explained in more detail in Appendix B.3.1), the probability is rewritten as

$$\mathcal{P}_{B_t}[z, v, \eta] = \mathcal{N} \int \mathcal{D}u \prod_t \delta(\dot{z} - v) e^{-\int \mathrm{d}t iu^T (m\dot{v} + Kz + \gamma v + BAv - \eta)} e^{-\int \mathrm{d}t iu^T \Delta B_t Av} \mathcal{P}[\eta], \quad (3.5)$$

where the integration limits range from $-\infty$ to ∞ when unspecified.

With this expression for probability, the average of an observable O in the time-modulated system can be written as

$$\begin{aligned} \langle O \rangle_{B_t} &= \int \mathcal{D}z\mathcal{D}v\mathcal{D}\eta\ O\mathcal{P}_{B_t}[z, v, \eta] && (3.6) \\ &= \int \mathcal{D}z\mathcal{D}v\mathcal{D}\eta\mathcal{D}u\ Oe^{-\int \mathrm{d}t iu^T \Delta B_t Av} \mathcal{N} \prod_t \delta(\dot{z} - v) e^{-\int \mathrm{d}t iu^T (m\dot{v} + Kz + \gamma v + BAv - \eta)} \mathcal{P}[\eta]. && (3.7) \end{aligned}$$

The observable averaged under the reference dynamics can be similarly expressed as (simply by setting $\Delta B_t = 0$),

$$\langle O \rangle = \int \mathcal{D}z\mathcal{D}v\mathcal{D}\eta\mathcal{D}u\ O\mathcal{N} \prod_t \delta(\dot{z} - v) e^{-\int \mathrm{d}t iu^T (m\dot{v} + Kz + \gamma v + BAv - \eta)} \mathcal{P}[\eta]. \quad (3.8)$$

Comparing the expression for $\langle O \rangle_{B_t}$ and for $\langle O \rangle$, we obtain

$$\langle O \rangle_{B_t} = \left\langle O e^{-\int \mathrm{d}t \Delta B_t iu^T Av} \right\rangle. \quad (3.9)$$

In the small $\Delta B(t)$ regime, an expansion can be performed,

$$e^{-\int \mathrm{d}s \Delta B_s iu^T Av} = 1 - \int \mathrm{d}s\, \Delta B_s iu_s^T Av_s + \frac{1}{2} \int \mathrm{d}s\, \mathrm{d}s'\, (\Delta B_s iu_s^T Av_s)(\Delta B_{s'} iu_{s'}^T Av_{s'}) - \ldots \quad (3.10)$$

The last two expressions connects averages under modulated $B(t)$ to averages under constant B. The latter can be calculated with our knowledge with the reference system from Chapter 2.

3.4.2 Expansion in modulation and expression of multi-point correlators

The observable we are interested in is the energy absorbed on site i, Eq. (3.3). Here we rewrite the energy flux using a projection operator P_i,

$$P_i = |i\rangle\langle i| \otimes \begin{pmatrix} 1 & 0 \\ 0 & 1 \end{pmatrix}, \tag{3.11}$$

as

$$Q_i = \int_0^T \mathrm{d}t\, q_i(t), \quad q_i(t) = -\gamma (P_i v_t)^T P_i v_t + (P_i v_t)^T P_i \eta_t. \tag{3.12}$$

The projection operator conveniently separates the step of calculating correlators with full-dimensional ($2N$) vectors and the step of picking out the subspace for particle i.

Combining (3.12) with the expansion Eq. (3.9)-(3.10), the pumped energy can be expanded to the second order in ΔB as

$$\left\langle Q_i^{(0)} \right\rangle_{B_t} = \int_0^T \mathrm{d}t \left\langle q_i(t) \right\rangle, \tag{3.13}$$

$$\left\langle Q_i^{(1)} \right\rangle_{B_t} = -\int_0^T \mathrm{d}t\, \mathrm{d}s \left\langle q_i(t) \Delta B_s i u_s^T A v_s \right\rangle, \tag{3.14}$$

$$\left\langle Q_i^{(2)} \right\rangle_{B_t} = \frac{1}{2} \int_0^T \mathrm{d}t\, \mathrm{d}s\, \mathrm{d}s' \left\langle q_i(t) (\Delta B_s i u_s^T A v_s)(\Delta B_{s'} i u_{s'}^T A v_{s'}) \right\rangle. \tag{3.15}$$

The zeroth order $\left\langle Q_i^{(0)} \right\rangle_{B_t}$ vanishes from our previous derivation for Kirchoff's law under

constant-B cases in Appendix A.3,

$$\left\langle Q_i^{(0)} \right\rangle_{B_t} = \int_0^T \mathrm{d}t \, \langle q_i(t) \rangle = 0. \tag{3.16}$$

In calculations of $\left\langle Q_i^{(1)} \right\rangle_{B_t}$ and $\left\langle Q_i^{(2)} \right\rangle_{B_t}$, we will encounter multi-point correlators. These multi-point correlators for multivariate Gaussian distributions, which our reference system satisfies due to its linearity, can be expressed in terms of combinations of two-point correlators. For instance, the four-point correlator reduces to

$$\left\langle a^T b c^T d \right\rangle = \mathrm{tr} \left\langle a b^T \right\rangle \mathrm{tr} \left\langle c d^T \right\rangle + \mathrm{tr} \left\langle a c^T \right\rangle \left\langle d b^T \right\rangle + \mathrm{tr} \left\langle a d^T \right\rangle \left\langle c b^T \right\rangle. \tag{3.17}$$

In the physics literature, the reduction of multi-point correlators (especially in quantum systems) is often called Wick's theorem [137].

The two-point correlators can then be expressed in terms of Fourier transforms $\tilde{f}(\omega) = \int_{-\infty}^{\infty} \mathrm{d}t \, f(t) e^{-i\omega t}$ and the response function for the reference system (Eq. (2.6)),

$$G^{\pm}(\omega) = [K \pm i\omega(\gamma I + BA) - m\omega^2 I]^{-1}. \tag{3.18}$$

Explicit expressions for these two-point correlators are derived and displayed in Appendix B.3.2.

Now we summarize the procedure for perturbative expansion in modulated B-field. In the first step, we use MSR/JDP formalism to express the observable under weakly-modulated B-field in terms of averages under the unmodulated reference system, Eq. (3.9)-(3.10). In the second step, we express the multi-point correlators encountered in the expansion in terms of two-point correlators. In the last step, we plug in expressions for two-point correlators, and reach a simplified formula for $\left\langle Q_i^{(1)} \right\rangle_{B_t}$ and $\left\langle Q_i^{(2)} \right\rangle_{B_t}$.

3.4.3 Energy flux: first order in modulation

Starting from the expression Eq. (3.14) and performing the second and the third step outlined in the procedure above, we arrive at the energy flux from the order $(\Delta B)^1$

$$\left\langle Q_i^{(1)} \right\rangle_{B_t} = 2\gamma T_a T \int \frac{\mathrm{d}\omega}{2\pi} \Delta\tilde{B}_0 h(\omega)(i\omega)^2 \,\mathrm{tr}\Big[P_i G^+(\omega) A G^+(\omega)^T\Big]. \tag{3.19}$$

In the above expression, we have introduced $h(\omega)$ to describe a general noise spectrum

$$\left\langle \tilde{\eta}(\omega)\tilde{\eta}(\omega')^T \right\rangle = 2\gamma T_a h(\omega) 2\pi\delta(\omega+\omega'), \tag{3.20}$$

and Fourier series expansion of $\Delta B(t)$ with coefficients $\Delta\tilde{B}_n$,

$$\Delta B(t) = \sum_{n=-\infty}^{\infty} \Delta\tilde{B}_n e^{i\omega_n t}, \quad \omega_n = \frac{2\pi n}{T}, \tag{3.21}$$

with the property $\Delta\tilde{B}_n = \Delta\tilde{B}^*_{-n}$.

Eq. (3.19) shows that the only contribute to the first order energy flux is the zero-frequency mode of $\Delta B(t)$, which corresponds to a constant B-field. We have shown in Chapter 2 that energy flux between particles and baths is zero for constant B-field. As a result, $\left\langle Q_i^{(1)} \right\rangle_{B_t}$ should vanish. Indeed, since $G^+(\omega)^T P_i G^+(\omega)$ is a symmetric matrix and A is an antisymmetric matrix, the trace vanishes,

$$\mathrm{tr}\Big[P_i G^+(\omega) A G^+(\omega)^T\Big] = \mathrm{tr}\Big[A(G^+(\omega)^T P_i G^+(\omega))\Big] = 0. \tag{3.22}$$

We conclude that the energy flux from the first order of ΔB is zero,

$$\left\langle Q_i^{(1)} \right\rangle_{B_t} = 0. \tag{3.23}$$

3.4.4 Energy flux: second order in modulation

Starting from the expression Eq. (3.15) and performing the second and the third step outlined in the procedure above, we arrive at the energy flux from the order $(\Delta B)^2$,

$$\left\langle Q_i^{(2)} \right\rangle_{B_t} = 4\gamma T_a T \sum_{n=1}^{\infty} |\Delta \tilde{B}_n|^2 \int \frac{\mathrm{d}\omega}{2\pi} \Big\{ \omega^2(\omega+\omega_n)(h(\omega+\omega_n)-h(\omega)) \\ \mathrm{Re}[i \,\mathrm{tr}\, P_i G^+(\omega) A G^+(\omega+\omega_n) A G^+(-\omega)^T] \Big\}. \tag{3.24}$$

This expression is the main result of this section. As sanity checks, $\left\langle Q_i^{(2)} \right\rangle_{B_t}$ does satisfy energy balance, $\sum_i \left\langle Q_i^{(2)} \right\rangle_{B_t} = 0$, and if $\Delta B(t)$ is constant, $\left\langle Q_i^{(2)} \right\rangle_{B_t}$ does vanish. Derivations are detailed in Appendix B.3.4.

Eq. (3.24) illustrates a coupling between modes of G^+ and a decoupling between modes of ΔB. For the response function G^+, a coupling of its Fourier modes at frequency $\omega, -\omega, \omega + \omega_n$, as written in the integrand, is induced by the modulation of B-field. This is in contrast with the unmodulated case where $G^+(\omega)$ at different frequencies are uncoupled (Appendix A.3 Eq. (A.50)). The coupling between response functions opens the possibility of net energy transfer between nodes and baths.

For the modulation $\Delta B(t)$, different modes $\Delta \tilde{B}_n$ are decoupled in the summation. Such decoupling greatly simplifies the discussion on modulation protocols. For instance, the energy flux induced by protocol $\Delta B(t) = c_1 \sin 2\pi t/T + c_2 \sin 4\pi t/T$ with small but arbitrary coefficients $\{c_1, c_2\}$ can be obtained simply as a weighted summation of the energy flux with $\Delta B(t) = \sin 2\pi t/T$ and that with $\Delta B(t) = \sin 4\pi t/T$.

The role of activity takes effect through the factor $(h(\omega+\omega_n) - h(\omega))$. If the noise spectrum $h(\omega)$ is constant, which corresponds to a white noise, this factor vanishes. Only colored noise with nonconstant spectrums can generate a nonzero $\left\langle Q_i^{(2)} \right\rangle_{B_t}$.

3.5 Further expansion in interactions: a diagrammatic approach

3.5.1 Diagrammatic expansion of energy flux

To reveal the relationship between the energy flux and the structure of networks, we further expand the expression Eq. (3.24) with respect to the spring constant in the small-k regime.

Applying the diagrammatic approach described in Appendix A.6.1, we expand $G^+(\omega)$ with respect to k, then decompose each term to paths. We obtain an expression of $\left\langle Q_i^{(2)} \right\rangle_{B_t}$ as sum over paths,

$$\frac{\left\langle Q_i^{(2)} \right\rangle_{B_t}}{T_a} = \sum_{n=1}^{\infty} T|\Delta \tilde{B}_n|^2 \sum_l k^{|l|} f_{i,n;l}. \tag{3.25}$$

Path l with length $|l|$ is $i = l_0 \to l_1 \to \cdots \to l_{|l|-1} \to l_{|l|} = i$, where l_a and l_b either has to be bonded or $l_a = l_b$. $f_{i,n;l}$ denotes the expression for path l. Eq. (3.25) is the major result of the diagrammatic approach. This expression connects the energy flux to lowest-order local paths, which allows for understanding arbitrary networks through its local structures. Using this diagrammatic expansion, as well as the expression for $f_{i,n;l}$ introduced below, we will show that the lowest-order diagrams appear at $|l| = 3$, then write down the explicit connection between energy flux and local paths on the order of $|l| = 3$.

Due to the appearance of three G^+'s in Eq. (3.24), path l needs to be partitioned into three segments with lengths $\{|l|_1, |l|_2, |l|_3\}$ ($|l|_1 + |l|_2 + |l|_3 = |l|$), and each segment sets how each G^+ is expanded. The expression for path l, $f_{i,n;l}$, is then a sum over all partitions,

$$f_{i,n;l} = \sum_{|l|_1+|l|_2+|l|_3=|l|} f_{i,n;l;|l|_1,|l|_2,|l|_3}. \tag{3.26}$$

Each partition reads

$$f_{i,n;l;|l|_1,|l|_2,|l|_3} = 2\,\mathrm{Re}\int \frac{\mathrm{d}\omega}{2\pi}\omega(\omega+\omega_n)(h(\omega+\omega_n)-h(\omega))\,\mathrm{tr}\Big\{M[(-K_s)g^+(\omega)]_{l_{|l|_1+|l|_2}\to\cdots i}$$
$$AM[g^+(\omega+\omega_n)(-K_s)]_{l_{|l|_1}\to\cdots l_{|l|_1+|l|_2}}g^+(\omega+\omega_n)$$
$$AM[g^+(-\omega)^T(-K_s)]_{i\to\cdots l_{|l|_1}}(g^+(-\omega)^T-g^+(\omega))\Big\}. \tag{3.27}$$

Here $g^+(\omega)$ is the response function for a single noninteracting node (Appendix A.7.2), which is mathematically equal to a rotation matrix of a complex angle α_ω,

$$g^+(\omega) = \frac{1}{k_{0,\omega}}(I\cos\alpha_\omega - A_1\sin\alpha_\omega), \tag{3.28}$$
$$k_{0,\omega} = \sqrt{(k_g+i\omega\gamma-m\omega^2)^2-(\omega B)^2}, \tag{3.29}$$
$$\cos\alpha_\omega = \frac{1}{k_{0,\omega}}(k_g+i\omega\gamma-m\omega^2), \tag{3.30}$$
$$\sin\alpha_\omega = \frac{1}{k_{0,\omega}}i\omega B. \tag{3.31}$$

$(-K_s)$ is the matrix that denotes interactions, where $(-K_s)_{ji}z_i$ equals the force from particle i to j when i is displaced by z_i. Using e_{ij} to denote the unit vector that points from the equilibrium position of i to that of j, the 2×2 matrix block $(-K_s)_{ji}$ reads

$$(-K_s)_{ii} = \sum_{j,j\neq i}(-e_{ij}e_{ij}^T), \tag{3.32}$$
$$(-K_s)_{ji} = e_{ij}e_{ij}^T. \tag{3.33}$$

Symbol $M[\cdot]$ is defined as

$$M[(-K_s)g^+(\omega)]_{l_0\to l_1\to\cdots\to l_n} = (-K_s)_{l_n,l_{n-1}}g^+(\omega)\cdots(-K_s)_{l_2,l_1}g^+(\omega)(-K_s)_{l_1,l_0}g^+(\omega), \tag{3.34}$$

$$M[g^+(\omega)(-K_s)]_{l_0\to l_1\to\cdots\to l_n} = g^+(\omega)(-K_s)_{l_n,l_{n-1}}\cdots g^+(\omega)(-K_s)_{l_2,l_1}g^+(\omega)(-K_s)_{l_1,l_0}. \tag{3.35}$$

From Eq. (3.25),(3.26),(3.27), we conclude the procedure to write down energy flux at site i on the order of $k^{|l|}$ as follows. Firstly, draw all possible closed paths with length $|l|$ that starts from node i, iteratively navigates to its bonded neighbors or to itself for $|l|$ steps, and ends at node i. Secondly, for each path l, find all partitions $\{|l|_1, |l|_2, |l|_3\}$, and calculate $f_{i,n;l;|l|_1,|l|_2,|l|_3}$ according to Eq. (3.27). Finally, sum up contributions from all partitions to get $f_{i,n;l}$ (Eq. (3.26)), then sum up all paths to obtain $\left\langle Q_i^{(2)}\right\rangle$ on $k^{|l|}$ order (Eq. (3.25)).

Path l and its corresponding mathematical expression $f_{i,n;l}$ can be presented as diagrams. An arrow $i \to j$ in the diagram corresponds to $(-K_s)_{ji}$, and as a result, if $i \neq j$, the contribution from this arrow is independent of the other neighbors of i or j (Eq. (3.33)). If $i = j$, however, neighbors of i cannot be removed because they do affect the value of $i \to i$ through $(-K_s)_{ii}$ (Eq. (3.32)). As a result, if a diagram contains no loops on some node j, the diagram is equal to a trimmed diagram where we remove all neighbors of j except for those that appear in the path. This basic property helps to simplify the diagrams without explicit calculations of $f_{i,n;l}$.

3.5.2 Diagrams: first and second order in k

We have already seen from numerical calculations that k^1, k^2 order fluxes vanish (Figure 3.2). Our first practice of the diagrammatic approach is then to show that $f_{i,n;l} = 0$ for $|l| = 1, 2$ in any networks. We proceed by showing that the first and second order diagrams vanish firstly for a two-node network, secondly for degree-1 node in arbitrary networks, and finally

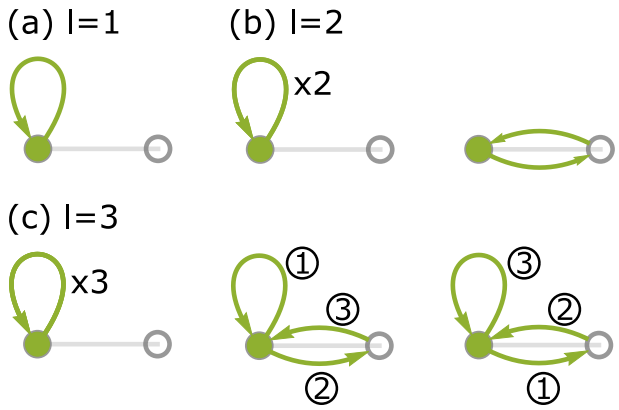

Figure 3.3: Diagrams for a two-node network from the order (a) k^1, (b) k^2, (c) k^3. The starting/ending node is labeled by a green dot. The number in circles labels the order of segments in the path.

for degree-d node in arbitrary networks. We index the focused node as i and its neighbors as j's.

Two-node networks satisfies $C2$-symmetry, consequently its flux as well as flux in any order vanish. On the first order, there is only one path, $i \to i$ (Figure 3.3a), so $f_{i,n;i\to i} = 0$. On the second order, there are two paths, $i \to i \to i$ and $i \to j \to i$ (Figure 3.3b), so their sum equals zero. The mathematical form of $f_{i,n;l}$ for these two paths read

$$f_{i,n;i\to i\to i} = \sum \mathrm{tr} \cdots (-K_s)_{ii} \cdots (-K_s)_{ii} \cdots , \tag{3.36}$$

$$f_{i,n;i\to j\to i} = \sum \mathrm{tr} \cdots (-K_s)_{ij} \cdots (-K_s)_{ji} \cdots . \tag{3.37}$$

For degree-1 nodes, $(-K_s)_{ii} = -e_{ij}e_{ij}^T = -(-K_s)_{ji} = -(-K_s)_{ij}$, which gives $f_{i,n;i\to i\to i} = f_{i,n;i\to j\to i}$. Taken together, we show that the two $|l| = 2$ diagrams vanish.

$$f_{i,n;i\to i\to i} = f_{i,n;i\to j\to i} = 0. \tag{3.38}$$

Similar arguments show that the three $|l| = 3$ diagrams also vanish (Figure 3.3c),

$$f_{i,n;i\to i\to i\to i} = f_{i,n;i\to i\to j\to i} = f_{i,n;i\to j\to i\to i} = 0. \tag{3.39}$$

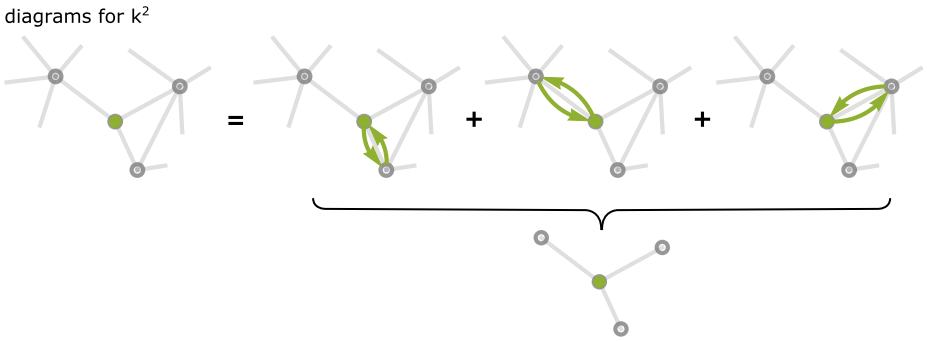

Figure 3.4: Second order diagrams for a node in arbitrary networks. LHS denotes the flux on second order. Each diagram equals to that in a trimmed network.

For a degree-1 node in arbitrary networks, its $|l| = 1, 2$ paths cannot contain loops on the neighbor j, thus the diagrams are equal to those where other neighbors of j are removed, which simply results in a two-node network. As shown in the previous paragraph, all $|l| = 1, 2$ diagrams vanish.

For a degree-d node in arbitrary networks, its $|l| = 1, 2$ diagrams equal to those in a trimmed network, where all non-nearest neighboring vertices and all bonds except for ones connecting with i are removed (Figure 3.4). As a result, the flux as a sum of all diagrams also equals to that in a trimmed one. Applying the energy balance property to the trimmed network, we have

$$\left\langle Q_i^{(1,2)} \right\rangle = -\sum_{j \neq i} \left\langle Q_j^{(1,2)} \right\rangle = 0. \tag{3.40}$$

RHS vanishes because node j's are degree-1.

3.5.3 Diagrams: third order in k

Having shown that the first and second order always vanish, we now discuss the third order diagrams. The third order diagrams do not vanish in general, making them the main contribution to energy fluxes in the network. In Figure 3.5, we write down all diagrams for a node in arbitrary networks. The network fragment in Figure 3.5 is representative of all possible

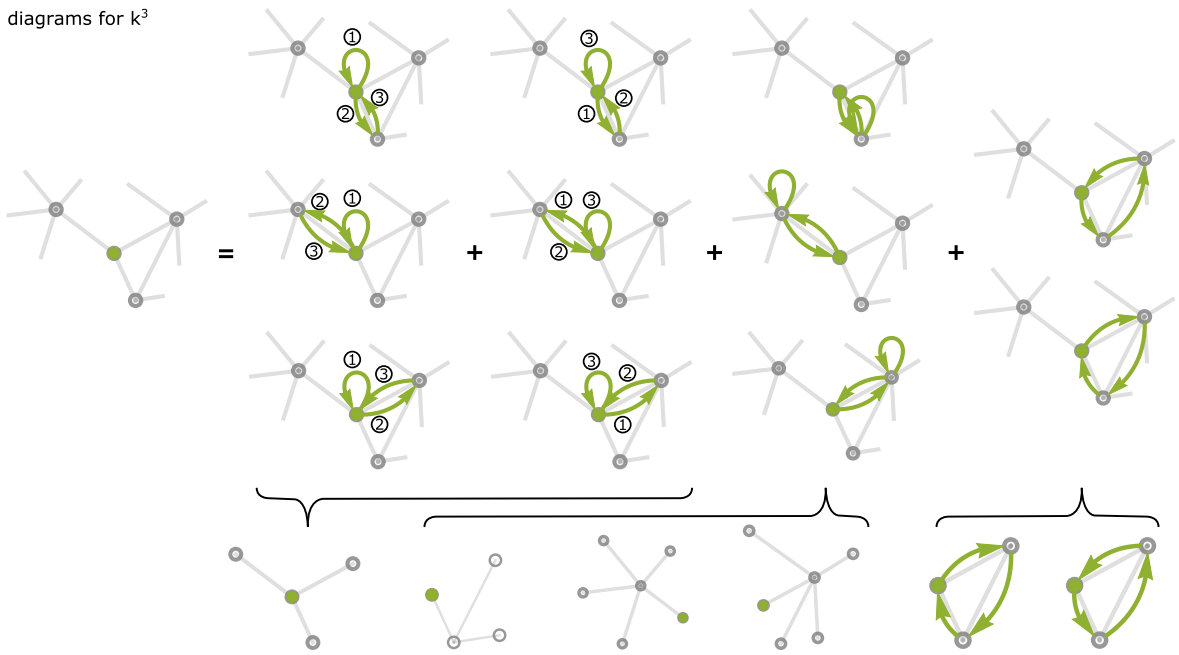

Figure 3.5: Third order diagrams for a node in arbitrary networks. Diagrams can be classified into three groups.

connections surrounding a node i, which include bondings between i and its neighbors j's, bondings between two of the neighbors, and bondings between neighbors and other nodes in the network. The flux on the generic node i from the third order equals to the sum of all diagrams with $|l| = 3$. These diagrams can be divided in to three classes, (i) diagrams containing a loop on i, such as $i \to i \to j \to i$, $i \to j \to i \to i$, (ii) diagrams containing a loop on j, $i \to j \to j \to i$, (iii) diagrams containing arrows between j's if they are bonded, $i \to j_1 \to j_2 \to i$. Note that the diagram with only loops ($i \to i \to i \to i$) vanish (shown in Appendix B.4), thus it is not included in the summation.

The presentation can be simplified by replacing the sum of diagrams in class (i) or each diagram in class (ii) to their equivalents. All class (i) diagrams contain no loops on j, thus other neighbors of j can be trimmed. The sum of all class (i) diagrams is then equal to the third order flux of node i in a trimmed subnetwork where all neighbors of j and all connections between j's are removed. Class (ii) diagrams contain no loops on i but a loop on j, thus other neighbors of i can be trimmed. Each class (ii) diagram is equal to the flux of

node i in a trimmed subnetwork centered on j. Class (iii) diagrams, however, do not equal to flux in any subnetworks.

Taken together, we obtain a connection of energy flux on a node in arbitrary networks to its local network structures. The connection reads that the third order flux of a node i in arbitrary networks equals to a sum of (i) flux of i in a trimmed subnetwork centered at i, (ii) flux of i in trimmed subnetworks each centered on a neighbor j, (iii) triangle diagrams of the form $i \to j_1 \to j_2 \to i$. This is the major result derived from the diagrammatic expression written in Eq. (3.25). If a network does not contain any triangular connections, then its flux simply equals to the sum of flux of trimmed subnetworks described in (i),(ii), which means that we can reconstruct the flux in a large-scale network from fluxes in small subnetworks.

3.6 Comparisons between theory and numerical results

In this section, we compare our theory with numerical results, and show good agreement in the perturbative regime. From the perturbation theory, we also obtained two properties of the flux, namely the decoupling between different modes of modulation, and the ability to reconstruct fluxes from subnetworks. Using direct numerical calculations, we show that the applicability of these derived properties goes beyond the regime where the perturbative theories themselves have small errors.

In Figure 3.6, we show comparisons between flux from perturbative theories and flux from direct numerical calculations in regimes of small ΔB and k. The flux is shown for the middle node in the Y-shaped network in Figure 3.1b, and the modulation protocol is $B(t) = \Delta B \sin 2\pi t/T$. Figure 3.6a is calculated from the perturbative theory in ΔB, Eq. (3.24). The difference is less than 5% in small ΔB regime and, unsurprisingly, small and large k regime. Figure 3.6b is calculated from the perturbative theory in both ΔB and k, Eq. (3.25). The difference is less than 20% in small ΔB and small k regime. We see good agreements between theoretical results and numerical results in the perturbative regime, as expected.

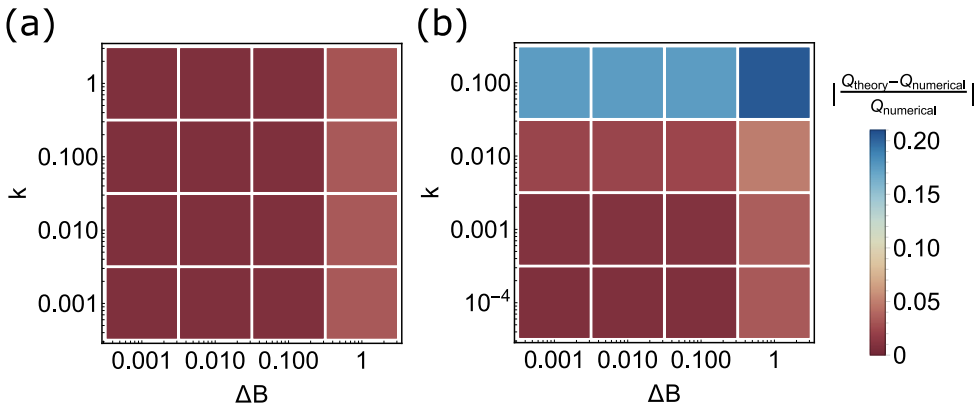

Figure 3.6: Comparison between flux from direct numerical calculations and flux from perturbative expansions in (a) small ΔB, (b) both small ΔB and small k. The flux is shown for the middle node in the Y-shaped network in Figure 3.1b, and the protocol is $B(t) = \Delta B \sin 2\pi t/T$. All other parameters are set to 1.

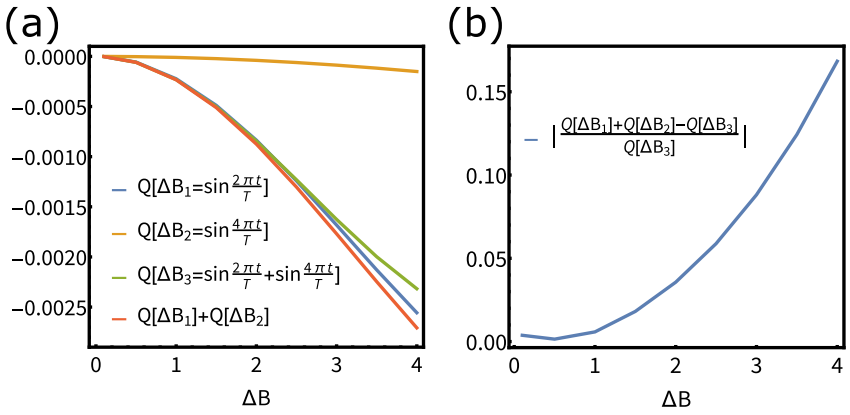

Figure 3.7: Comparison between flux with combined protocol and combination of flux from individual protocols. The protocols read, for instance, $\Delta B_1(t) = \Delta B \sin 2\pi t/T$. (a) Value of fluxes under individual modulation, $\Delta B_1, \Delta B_2$, under combined modulation ΔB_3, and combined flux under individual modulations. (b) Error of combined flux with respect to flux under combinded modulations. The flux is shown for the middle node in the Y-shaped network in Figure 3.1b. All fluxes are calculated from direct numerical methods. All other parameters are set to 1.

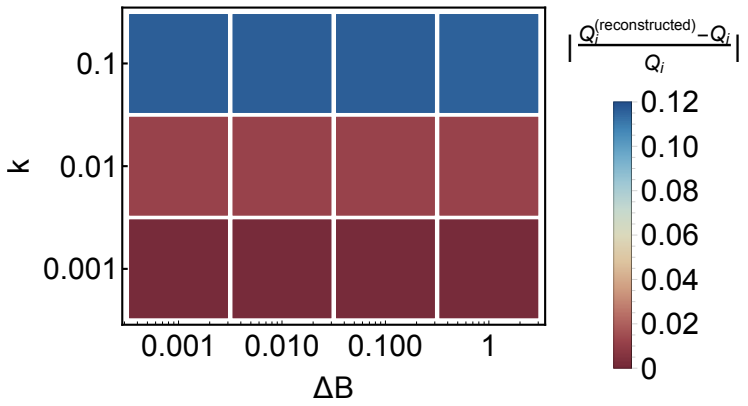

Figure 3.8: Comparison between flux in the full network and combination of flux in trimmed subnetworks. The error in flux is averaged over all nodes. We used the disordered network in Figure 3.1c. The modulation is a step-function modulation where the period is set to 1. All fluxes are calculated from direct numerical methods. All other parameters are set to 1.

From the perturbative theory on weak modulations, we have seen in Eq. (3.24) that the contribution to energy flux from different modes of modulation are decoupled. In Figure 3.7, we test how well this decoupling property holds for a range of ΔB. All fluxes are calculated from direct numerical methods, so as to exclude errors from perturbative theories in regimes beyond small ΔB's. As shown in Figure 3.7, the error of mode decoupling at $\Delta B = 1$ is 0.6%, whereas the error of perturbative theory shown in Figure 3.6 is 3%. This comparison shows that the property of mode decoupling, although derived in the small ΔB regime, remains a good approximation even when ΔB is not relatively small.

From the diagrammatic approach, we have shown in Sec. 3.5.3 that flux in a full network can be reconstructed as a sum of flux in trimmed subnetworks. Here we have assumed that the network do not contain triangular connections, so that the triangle diagrams can be ignored. In Figure 3.8, we test how well this reconstruction relation holds for a range of ΔB and k. All fluxes are calculated from direct numerical methods in order to exclude errors from perturbative theories in regimes beyond small ΔB and small k. We see that the error of the reconstruction relation is small in small k regime, as expected from the diagrammatic theory. Interestingly, the error remains small at relatively large ΔB's, despite that the theory assumed both ΔB and k to be small.

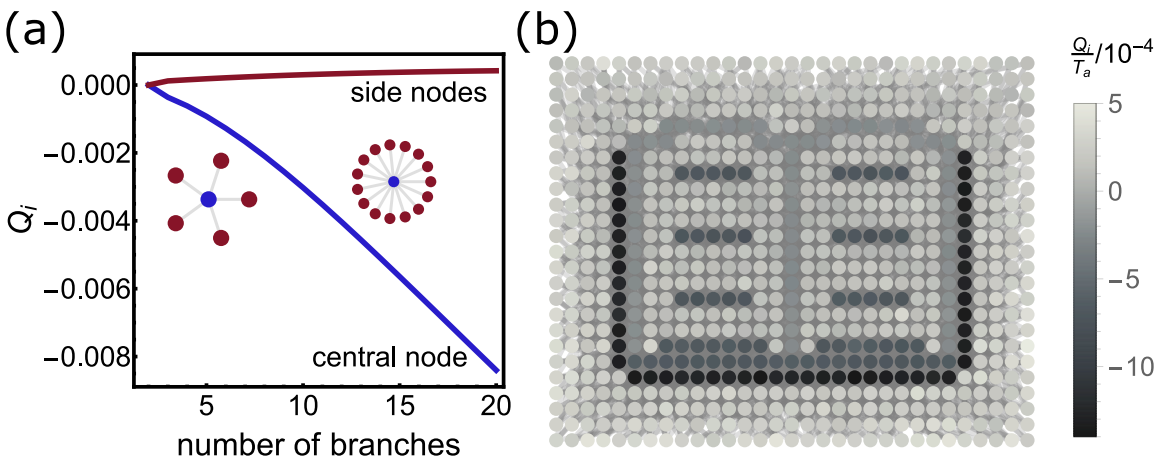

Figure 3.9: Creating target flux patterns by exploiting the connection between flux in a network and in its local subnetworks. (a) Flux of network with branches. (b) Constructed network and its flux pattern that mimics a grayscaled book. The modulation is a step-function modulation where the period is taken to infinite. All fluxes are calculated from direct numerical methods. All parameters are set to 1 except that $k = 0.05$.

3.7 Utilizing local building blocks to create complex patterns of energy transport

The connection between flux in a network and in its local subnetworks can be exploited to create complex patterns of energy transport. If we assume that the energy in the bath diffuses slowly, the energy fluxes then can lead to changes in temperature, which means that our setup could potentially engineer temperature inhomogeneities using homogeneous modulations.

The objective can be posed as follows, given a grid of unconnected nodes and a target pattern, design connections among the nodes such that the flux pattern of the connected network matches a target one. Given the connection between flux in complex networks and its local structures as shown in Sec. 3.5.3, we can inversely use the local subnetworks as building blocks to construct a flux pattern. The building blocks are networks with one central node and a number of evenly-separated branches. Figure 3.9a shows that the flux of the central node increases in its magnitude as the number of branches increases. Based on the observed

relation between the flux and the number of branches, we can create connections simply by considering the difference between the degree of a node and degrees of its neighbors. Consider a target pattern that consists of white background and darker lines, we first highlight nodes corresponding to darker pixels in the pattern. Then we create connections between the highlighted nodes and the nonhighlighted ones. The degree of a highlighted node is set by the darkness of its corresponding pixel in the target pattern. Connections to nonhighlighted nodes are not controlled, but their average degree is smaller than that of the highlighted ones. We avoid connections between highlighted nodes or between unhighlighted nodes, in order to avoid effects from triangle diagrams. Note that the connections built from this strategy can be long-ranged in space. In Figure 3.9b we demonstrate the pattern of a grayscaled book constructed through the above strategy. With more carefully designed strategy, it is possible to achieve a broader range of patterns and/or avoid long-ranged connections.

3.8 Conclusion

In conclusion, we have constructed an active gyroscopic network model where the B-field is modulated in a time-periodic manner. We numerically demonstrated that our model is able to rectify energy transport between nodes and baths in the absence of any temperature biases. Importantly, by combining the MSR/JDP formalism and our diagrammatic approach, we find a connection between the flux in complex networks and properties of local subnetworks. Such connection enables us to understand and control rectification in arbitrary networks. The combined MSR/JDP and diagrammatic approach can in principle apply to calculate generic correlators for perturbed linear networks.

CHAPTER 4

A MECHANISM FOR ANOMALOUS TRANSPORT IN CHIRAL ACTIVE LIQUIDS

This chapter is reproduced and adapted from the publication: Liao, Zhenghan, Ming Han, Michel Fruchart, Vincenzo Vitelli, and Suriyanarayanan Vaikuntanathan. 2019. "A Mechanism for Anomalous Transport in Chiral Active Liquids." The Journal of Chemical Physics 151 (19): 194108. https://doi.org/10.1063/1.5126962 [138].

4.1 Introduction

Recent work on active and driven matter systems have significantly advanced our understanding of how non-equilibrium forces can be used to modulate properties of soft matter systems and materials [70, 139, 45, 84, 109]. In this chapter, we focus on a particular class of active matter systems, namely, chiral active liquids [140, 98, 141]. In these systems a non-equilibrium steady state is sustained through a steady injection of energy into the rotational degrees of freedom of each constituent molecule or rotor. Studies of such chiral active fluids in recent years have discovered a variety of interesting phenomena, including rich phase behavior [95, 142], non-equilibrium self-assembly [143, 144, 145], ordered phase stabilization [146], and localized mass currents at a boundary or an interface [94, 96, 95]. Importantly, various studies have shown how the transport properties of chiral active systems are influenced by anomalous coefficients such as the so-called "odd" or Hall viscosity [98, 102, 100]. Unlike the conventional shear viscosity which leads to a resistance parallel to the direction of a velocity gradient, the odd/Hall viscosity is responsible for an anomalous response in the transverse direction. Odd viscosity was postulated to be a generic feature of parity symmetry-breaking fluids [99], and it has been studied for systems like gases under Lorentz-like forces [147, 102]. However, until recently [98], this term has not typically been included in hydrodynamic descriptions of chiral active fluids, possibly because its importance was not clear in many

previously studied systems [94, 140, 95]. An understanding of odd viscosity from a molecular perspective, in particular the role played by activity, will be beneficial and aid in building a connection between the microscopic structure and the macroscopic transport properties of active chiral liquids [103, 104].

In this chapter, we provide a mechanism for how odd viscosity and other anomalous transport coefficients can emerge due to non-equilibrium activity in chiral active liquids. Our approach is motivated by Irving and Kirkwood's seminal work on the statistical mechanical theory of transport properties [105, 148, 149]. Specifically, we adapt Irving and Kirkwood's techniques[150, 151, 152, 103] and show that the stress tensor of a chiral liquid can be expressed in terms of orientation-averaged intermolecular forces and pair correlation functions computed using the center of mass locations of the chiral active molecules. Our central results then show how anomalous transport coefficients can naturally emerge due to the presence of a transverse component in the orientation-averaged force and anomalous modes in the distortion of the pair correlation function induced by flows. Features such as a transverse component in the orientation-averaged force can be sustained due to the non-equilibrium activity in the chiral liquid.

The rest of this chapter is organized as follows. In Sec. 4.2, we review the Irving-Kirkwood method and adapt this technique to compute the stress tensor for chiral active fluids. In Sec. 4.3, we extract transport coefficients from the stress tensor, and show how anomalous transport coefficients can naturally emerge in chiral active systems. Central theoretical results for transport coefficients are formulated in Eq. (4.28)-(4.37). In Sec. 4.4, we describe results from numerical simulations of an active rotor systems that support our theoretical predictions.

4.2 Stress tensor for chiral active fluids

In this section, we review and adapt the Irving-Kirkwood technique [105] to construct a stress tensor for chiral active liquids. Irving-Kirkwood-type stress tensors generally consist

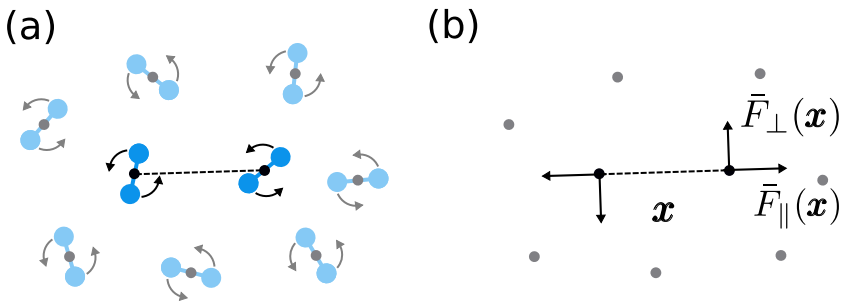

Figure 4.1: Schematic of the type of system we consider and the emergence of perpendicular averaged force. (a) A chiral active system with interacting rotors experiencing active torques. (b) After averaging over the orientation of rotors, the orientation-averaged intermolecular forces generically contain both an ordinary radial component $\overline{\boldsymbol{F}}_\parallel(\boldsymbol{x})$ and a peculiar perpendicular component $\overline{\boldsymbol{F}}_\perp(\boldsymbol{x})$. We will show that the anomalous transport coefficients can be expressed in terms of this perpendicular force.

of a kinetic part and a potential part. In this work we only focus on the potential part, which is the dominant contribution for liquids [105, 153]. We do not consider the kinetic part, which becomes important for dilute gas-like systems [105, 153]. The potential part of the stress tensor will be expressed in terms of the orientation-averaged intermolecular forces and the pair correlation function of the center of mass of each molecule. We will show in subsequent sections how these two factors can be modified due to chiral activity, and how the modifications combine to produce anomalous transport properties. The chiral active liquids are assumed to be two-dimensional (2D) or quasi-2D, single-component and homogeneous.

The starting point for our derivation is the mechanical definition of the stress tensor $\boldsymbol{\sigma}$ as $\boldsymbol{\sigma}\cdot\mathrm{d}\boldsymbol{S}$ = "force across $\mathrm{d}\boldsymbol{S}$", where $\mathrm{d}\boldsymbol{S}$ is the normal vector of a line segment in the 2D plane and points from the inside to the outside. The homogeneity assumption can be justified by placing the line segment, for instance, well inside a large finite sample, or inside an infinite system simulated via periodic boundary conditions. Here, "Across" means that the vector $\boldsymbol{x}$, which connects the center of mass of a molecule inside of $\mathrm{d}\boldsymbol{S}$ to one outside, intersects

with $\mathrm{d}\boldsymbol{S}$ at position $\boldsymbol{X}$. The force across $\mathrm{d}\boldsymbol{S}$ acting on the inside of $\mathrm{d}\boldsymbol{S}$ can be written as

$$\begin{aligned}\boldsymbol{\sigma}\cdot\mathrm{d}\boldsymbol{S} = -\int \mathrm{d}\boldsymbol{\theta} \int\limits_{\boldsymbol{x}\cdot\mathrm{d}\boldsymbol{S}>0} \mathrm{d}\boldsymbol{x} \int_0^1 \mathrm{d}\alpha\, \boldsymbol{F}(\boldsymbol{x};\boldsymbol{\theta}) \\ \rho^{(2)}(\boldsymbol{X}-\alpha\boldsymbol{x}, \boldsymbol{X}+(1-\alpha)\boldsymbol{x};\boldsymbol{\theta})\boldsymbol{x}\cdot\mathrm{d}\boldsymbol{S}\,.\end{aligned} \tag{4.1}$$

In this expression, $\boldsymbol{\theta} = \{\theta_1, \theta_2\}$ denotes the orientation of the two molecules with respect to fixed x-axis in the $2D$-plane, $\boldsymbol{F}(\boldsymbol{x};\boldsymbol{\theta})$ is the intermolecular force, $\rho^{(2)}(\boldsymbol{X}-\alpha\boldsymbol{x}, \boldsymbol{X}+(1-\alpha)\boldsymbol{x})$ is the two-body density, and $\rho^{(2)}(\boldsymbol{X}-\alpha\boldsymbol{x}, \boldsymbol{X}+(1-\alpha)\boldsymbol{x};\boldsymbol{\theta})\,\mathrm{d}\boldsymbol{S}\cdot\boldsymbol{x}\,\mathrm{d}\alpha\,\mathrm{d}\boldsymbol{x}$ describes the probability of finding one molecule around $\boldsymbol{X}-\alpha\boldsymbol{x}$ with orientation θ_1 and another around $\boldsymbol{X}+(1-\alpha)\boldsymbol{x}$ with orientation θ_2, where $\alpha\in[0,1]$ is a parametrization of the location of the molecule pair. From the expression for $\boldsymbol{\sigma}\cdot\mathrm{d}\boldsymbol{S}$, the stress tensor $\boldsymbol{\sigma}$ can be identified.

The expression for the stress tensor can be simplified using the homogeneity of the system. Due to homogeneity or translational invariance, the two-body density $\rho^{(2)}(\boldsymbol{X}-\alpha\boldsymbol{x}, \boldsymbol{X}+(1-\alpha)\boldsymbol{x};\boldsymbol{\theta})$ reduces to $\rho^{(2)}(\boldsymbol{x};\boldsymbol{\theta})$, where the relative positions of the two molecules $\boldsymbol{x}$ replaced their absolute positions $\boldsymbol{X}-\alpha\boldsymbol{x}, \boldsymbol{X}+(1-\alpha)\boldsymbol{x}$. Next we express the two-body density in terms of conditional probabilities and the pair correlation function,

$$\rho^{(2)}(\boldsymbol{x};\boldsymbol{\theta}) = p(\boldsymbol{\theta}|\boldsymbol{x})\rho^{(2)}(\boldsymbol{x}) = p(\boldsymbol{\theta}|\boldsymbol{x})\rho^2 g(\boldsymbol{x}). \tag{4.2}$$

Here $p(\boldsymbol{\theta}|\boldsymbol{x})$ denotes the probability density of the orientation of the molecule pair conditioned on their positions. $\rho^{(2)}(\boldsymbol{x})$ denotes the two-body density regardless of molecular orientations, which equals to the product of density ρ squared and the pair correlation function regardless of orientations, $g(\boldsymbol{x})$. Plugging Eq. (4.2) into Eq. (4.1), the stress tensor becomes

$$\boldsymbol{\sigma} = -\int \mathrm{d}\boldsymbol{x}\,\mathrm{d}\boldsymbol{\theta}\,\frac{1}{2}\boldsymbol{F}(\boldsymbol{x};\boldsymbol{\theta})\boldsymbol{x}p(\boldsymbol{\theta}|\boldsymbol{x})\rho^2 g(\boldsymbol{x}), \tag{4.3}$$

where the integral over the whole space $\int \mathrm{d}\boldsymbol{x}\,/2$ is converted from $\int_{\boldsymbol{x}\cdot\mathrm{d}\boldsymbol{S}>0}\mathrm{d}\boldsymbol{x}$. This expres-

sion can be further simplified by defining an orientation-averaged intermolecular force,

$$\bar{\boldsymbol{F}}(\boldsymbol{x}) = \int \mathrm{d}\boldsymbol{\theta}\, \boldsymbol{F}(\boldsymbol{x};\boldsymbol{\theta}) p(\boldsymbol{\theta}|\boldsymbol{x}). \tag{4.4}$$

The Irving-Kirkwood-type stress tensor now reads

$$\boldsymbol{\sigma} = -\int \mathrm{d}\boldsymbol{x}\, \frac{1}{2} \bar{\boldsymbol{F}}(\boldsymbol{x}) \boldsymbol{x} \rho^2 g(\boldsymbol{x}). \tag{4.5}$$

Starting with Eq. (4.5), we demonstrate in Sec. 4.3 how expressions for various transport coefficients can be extracted.

Under conditions of equilibrium, the orientation-averaged force between two molecules in a chiral fluid will only contain a radial component. For chiral fluids out of equilibrium, however, the averaged force can contain a component that is perpendicular to $\boldsymbol{x}$ (sketched in Figure 4.1). We denote this perpendicular force as $\bar{\boldsymbol{F}}_\perp(\boldsymbol{x})$. The emergence of $\bar{\boldsymbol{F}}_\perp(\boldsymbol{x})$ can be motivated by a thought experiment using a system composed of a dilute gas of rotors interacting according to a repulsive potential (Figure 4.1). At equilibrium, the system obeys parity symmetry, which constrains $\bar{\boldsymbol{F}}_\perp(\boldsymbol{x})$ between rotors to be zero. When driven out of equilibrium by driving each rotor with an active torque, the system violates parity symmetry, which can allow for a nonzero $\bar{\boldsymbol{F}}_\perp(\boldsymbol{x})$. Mechanistically, when the arms of the two rotors rotate toward each other, rotors' rotation would be hindered due to repulsive interactions, thus more time would be spent on this configuration. As a result, this configuration gains more statistical weight and biases $\bar{\boldsymbol{F}}_\perp(\boldsymbol{x})$ towards a nonzero value. This simple argument becomes intractable for dense liquid systems with many interacting rotors. In Sec. 4.4.1, we use numerical simulations to study how a transverse component in the orientation-averaged force can emerge due to non-equilibrium activity.

We note debates in literature concerning the uniqueness of the Irving-Kirkwood stress tensor [105, 154, 155, 156, 157]. However, most of these issues emerge due to the presence of inhomogeneities, such as due to the presence of surfaces or interfaces and are not important

for the kind of homogeneous systems considered in this work.

4.3 Extracting transport coefficients from the stress tensor

Transport coefficients are linear response coefficients of the stress tensor under a velocity gradient. To extract transport coefficients from the stress tensor in Eq. (4.5), we investigate how Eq. (4.5) changes in the presence of a flow field using a method motivated by Ref. [149, 99]. Upon an application of such a velocity gradient or flow field, the stress tensor can respond due to a change in either the pair correlation function $g(\boldsymbol{x})$, or the orientation-averaged force $\bar{\boldsymbol{F}}(\boldsymbol{x})$. In this work, we only consider the distortion of the pair correlation function induced by the flow field in order to extract the transport coefficients [149, 158]. Consequently, the expressions we derive for the various transport coefficients are only accurate when the orientation-averaged force remains unaffected by the application on an external flow field. Formally, we anticipate that this will happen in cases where the timescales of the rotational and translational motions are sufficiently separated and the dynamics of the chiral active system can effectively be simulated using point particles interacting via orientation-averaged forces. In practice we find that even in cases without a dramatic separation of timescales, the orientation-averaged force can be insensitive to the presence of an applied flow field in practice. We provide numerical evidence for one such example in Sec. 4.4.2.

4.3.1 Distortion modes of pair correlation functions in a flow field

We now derive expressions for the distortion modes of the pair correlation function $g(\boldsymbol{x})$ induced by an applied flow field. Our derivation, motivated by work in Ref. [149, 99], relies extensively on symmetry considerations. The symmetry argument in Ref. [99] is applied at the level of the viscosity tensor. In contrast, our symmetry argument is applied at the level of $g(\boldsymbol{x})$, which provides more microscopic details. Similar symmetry considerations were also used extensively in studies of distortions in $g(\boldsymbol{x})$ due to shear flows [158, 159, 160, 161].

Unlike these early studies which focused mainly on conventional fluids, we focus on terms that can emerge due to chirality and activity. The central results of this section show that the distortions of the pair correlation function due to the imposition of a flow field can be captured in terms of four modes as described in Eq. (4.21)-(4.25) and sketched in Figure 4.2.

We begin by considering the pair correlation function in the absence of any imposed flows, $g_0(\boldsymbol{x}) = g_0(r)$, and impose perturbative velocity gradients $\partial_k u_l$, where u_l is the l'th component of the velocity. We then expand $g(\boldsymbol{x})$ to first order in $\partial_k u_l$ and to second order in x_i ($x_1 \equiv x, x_2 \equiv y$) as

$$g(\boldsymbol{x}) = g_0(r) + M^{(2)}_{kl}(r)\partial_k u_l + M^{(4)}_{ijkl}(r)x_i x_j \partial_k u_l + \ldots, \tag{4.6}$$

where we have used Einstein's summation convention. The coefficients $M(r)$ describe the radial dependence, and factors $x_i x_j$ describe the angular dependence [160]. Higher orders of angular dependence, e.g. $x_i x_j x_k x_l$, are omitted here.

Isotropy requires that when the flow field $\boldsymbol{\nabla u}$ is rotated by an angle θ, the $g(\boldsymbol{x})$ is also rotated by θ, but its shape remains unchanged. This constraint of isotropy dramatically reduces the number of allowed variations in Eq. (4.6). Now we illustrate this constraint by taking the term $M^{(4)}_{ijkl}(r)x_i x_j \partial_k u_l$ as an example. We denote a rotation operation by angle θ as T,

$$T = \begin{pmatrix} \cos\theta & -\sin\theta \\ \sin\theta & \cos\theta \end{pmatrix}. \tag{4.7}$$

A rotated flow field $T_{k'k}\partial_k T_{l'l} u_l$ transforms the $M^{(4)}$ term to $M^{(4)}_{ijk'l'}(r)x_i x_j T_{k'k}\partial_k T_{l'l} u_l$. The value of this transformed term at point $T\boldsymbol{x}$ should equal the value of the original one at $\boldsymbol{x}$, which gives

$$M^{(4)}_{i'j'k'l'}(r)T_{i'i}x_i T_{j'j}x_j T_{k'k}\partial_k T_{l'l}u_l = M^{(4)}_{ijkl}(r)x_i x_j \partial_k u_l. \tag{4.8}$$

Since Eq. (4.8) holds for any $x_i, x_j, \partial_k u_l$, we conclude that isotropy requires that $M^{(4)}_{ijkl}$, and

from similar arguments $M_{ij}^{(2)}$, satisfy

$$M_{ij}^{(2)} = M_{i'j'}^{(2)} T_{i'i} T_{j'j}, \tag{4.9}$$

$$M_{ijkl}^{(4)} = M_{i'j'k'l'}^{(4)} T_{i'i} T_{j'j} T_{k'k} T_{l'l}. \tag{4.10}$$

In addition to isotropy, $M_{ijkl}^{(4)}$ should also satisfy a symmetry requirement that $M_{ijkl}^{(4)}$ is invariant under the exchange of i and j, which results from the expression $M_{ijkl}^{(4)}(r) x_i x_j \partial_k u_l$.

The requirements of isotropy and additional symmetry are easier to address if we express $M^{(2,4)}$ in a Pauli-like basis [99],

$$\begin{aligned} P^I &= \begin{pmatrix} 1 & 0 \\ 0 & 1 \end{pmatrix}, \quad P^X = \begin{pmatrix} 0 & 1 \\ 1 & 0 \end{pmatrix}, \\ P^Y &= \begin{pmatrix} 0 & 1 \\ -1 & 0 \end{pmatrix}, \quad P^Z = \begin{pmatrix} 1 & 0 \\ 0 & -1 \end{pmatrix}. \end{aligned} \tag{4.11}$$

Using the Pauli-like basis, $M^{(2,4)}$ are expanded as

$$M_{ij}^{(2)} = m^{(2)a} P_{ij}^a, a = I, X, Y, Z \tag{4.12}$$

$$M_{ijkl}^{(4)} = m^{(4)ab} P_{ij}^a P_{kl}^b, a = I, X, Z, b = I, X, Y, Z. \tag{4.13}$$

Eq. (4.9)-(4.10) now read

$$(T_{i'i} T_{j'j} - \delta_{i'i} \delta_{j'j}) P_{i'j'}^a m^{(2)a} = 0, \tag{4.14}$$

$$(T_{i'i} T_{j'j} T_{k'k} T_{l'l} - \delta_{i'i} \delta_{j'j} \delta_{k'k} \delta_{l'l}) P_{i'j'}^a P_{k'l'}^b m^{(4)ab} = 0. \tag{4.15}$$

Solving the above linear equations for $m^{(2)a}, m^{(4)ab}$, we get the allowed forms of $M^{(2,4)}$,

$$M^{(2)}_{kl} = m^{(2)s} P^I_{kl} + m^{(2)r} P^Y_{kl}, \tag{4.16}$$

$$M^{(4)}_{ijkl} = m^{(4)I} P^I_{ij} P^I_{kl} + m^{(4)s} (P^X_{ij} P^X_{kl} + P^Z_{ij} P^Z_{kl}) + \tag{4.17}$$

$$m^{(4)a} (P^X_{ij} P^Z_{kl} - P^Z_{ij} P^X_{kl}) + m^{(4)r} P^I_{ij} P^Y_{kl}, \tag{4.18}$$

where $m^{(2)s}, m^{(2)r}$, etc. are arbitrary functions of r.

Plugging the expressions for $M^{(2,4)}$ into the expansion of $g(\boldsymbol{x})$ Eq. (4.6) and grouping terms, we obtain the allowed distortions of $g(\boldsymbol{x})$. These distortions are responses to the strain rate ν_{kl} and vorticity ω, defined as

$$\nu_{kl} = \frac{1}{2}(\partial_k u_l + \partial_l u_k), \tag{4.19}$$

$$\omega = \frac{1}{2}(\partial_x u_y - \partial_y u_x). \tag{4.20}$$

The distorted $g(\boldsymbol{x})$ consists of, in addition to the unperturbed $g_0(r)$, four distortion modes,

$$g(\boldsymbol{x}) = g_0(r) + g^b(\boldsymbol{x}) + g^s(\boldsymbol{x}) + g^a(\boldsymbol{x}) + g^r(\boldsymbol{x}). \tag{4.21}$$

Each mode reads

$$g^b(\boldsymbol{x}) = m^b(r)(\nu_{xx} + \nu_{yy}), \tag{4.22}$$

$$g^s(\boldsymbol{x}) = m^s(r) \begin{pmatrix} x & y \end{pmatrix} \begin{pmatrix} \nu_{xx} - \nu_{yy} & 2\nu_{xy} \\ 2\nu_{yx} & \nu_{yy} - \nu_{xx} \end{pmatrix} \begin{pmatrix} x \\ y \end{pmatrix}, \tag{4.23}$$

$$g^a(\boldsymbol{x}) = m^a(r) \begin{pmatrix} x & y \end{pmatrix} \begin{pmatrix} -(\nu_{xy} + \nu_{yx}) & \nu_{xx} - \nu_{yy} \\ \nu_{xx} - \nu_{yy} & \nu_{xy} + \nu_{yx} \end{pmatrix} \begin{pmatrix} x \\ y \end{pmatrix}, \tag{4.24}$$

$$g^r(\boldsymbol{x}) = m^r(r)\omega, \tag{4.25}$$

where m^b, m^s, m^a, m^r are undetermined functions that depend only on the scalar r. The original functions like $m^{(2)s}$ are grouped into these new functions through, for example, $m^b = m^{(2)s} + m^{(4)I} r^2$. Determining the functions $m^{b,s,a,r}(r)$ requires theories starting from a given microscopic equation of motion or simulations of specific systems. To keep our discussion general, we retain these undetermined functions $m^{b,s,a,r}(r)$.

The modes of distortion in Eq. (4.22)-Eq. (4.25) can be interpreted as follows. The term g^b describes the distortion of the pair correlation function induced by dilation, while the terms g^s and g^a describe distortions induced by shear strain, and the term g^r describes a distortion induced by vortical flows. The four modes of distortion are illustrated graphically in Figure 4.2. For ordinary liquids with parity symmetry, the pair correlation function computed in the presence of a pure shear should be invariant under the exchange of x and y. Hence the distortion in the pair correlation function will not have a mode corresponding to the term g^a. Similar considerations in the presence of vortical flows allow us to rule out the distortion mode g^r. Thus from ordinary liquids with parity symmetry, the only allowed modes of distortion are g^b and g^s. For chiral fluids, however, there are no *a priori* constraints on these modes of distortion, so all four distortions g^b, g^s, g^a, g^r are possible. It should be noted that these constraints are based on the ansatz of $g(\boldsymbol{x})$, Eq. (4.6), where $\partial_k u_l$ is expanded to its first order and x_i is expanded to its second order. These constraints can break even for ordinary fluids when higher-order contributions are considered [159, 160, 161].

4.3.2 Anomalous transport coefficients

Using Eq. (4.22)-(4.25) and the expression for the stress tensor in Eq. (4.5), we can now extract the transport coefficients. The final results, displayed in Eq. (4.28)-(4.37), are combinations of the averaged forces $\bar{F}_{\parallel/\perp}$ and the modes in Eq. (4.21).

For ease of notations, we write the parallel(perpendicular) force as the gradient of a

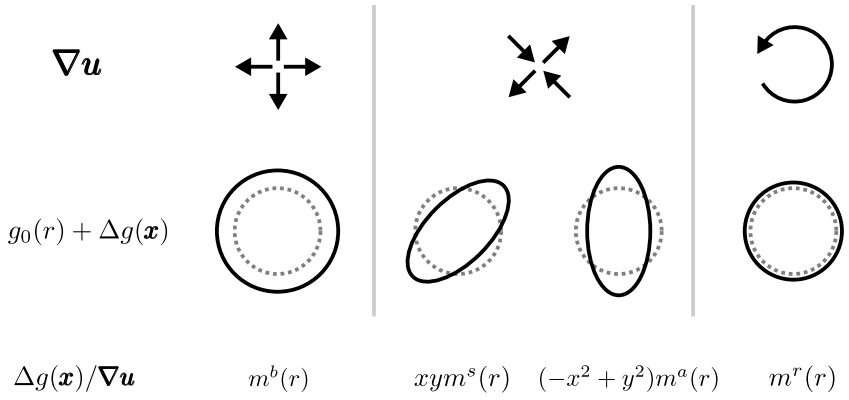

Figure 4.2: Schematic of the four modes of $g(\boldsymbol{x})$-distortion induced by a velocity gradient $\nabla \boldsymbol{u}$. The first row depicts three types of velocity gradient, dilation, pure shear flow, and vortical flow. The second row shows the corresponding modes of $g(\boldsymbol{x})$-distortion. Dotted circle represent the first peak of the undistorted $g(\boldsymbol{x})$, and the solid circles or ellipses are schematics of the distorted $g(\boldsymbol{x})$. In particular, the pure shear sketched in the middle column can induce two modes of distortion, denoted by m^s and m^a. The third row labels these distortion modes according to Eq. (4.22)-(4.25).

formal parallel(perpendicular) potential, $V'_{\parallel}(r)(V'_{\perp}(r))$.

$$\bar{\boldsymbol{F}}(\boldsymbol{x}) = -\frac{V'_{\parallel}(r)}{r}\begin{pmatrix} x \\ y \end{pmatrix} - \frac{V'_{\perp}(r)}{r}\begin{pmatrix} -y \\ x \end{pmatrix}. \tag{4.26}$$

We also introduce a notation for the average

$$\langle A \rangle_{\parallel/\perp} = \int_0^\infty \mathrm{d}r \, \frac{V'_{\parallel/\perp}(r)\rho^2}{2} \pi r^2 A(r). \tag{4.27}$$

After straightforward calculations, the final stress tensor can be written as,

$$\begin{aligned} \boldsymbol{\sigma} =& \boldsymbol{\sigma}_{e,0} + \boldsymbol{\sigma}_{e,r} + \boldsymbol{\sigma}_{e,b} + \boldsymbol{\sigma}_{e,s} + \boldsymbol{\sigma}_{e,a} + \\ & \boldsymbol{\sigma}_{o,0} + \boldsymbol{\sigma}_{o,r} + \boldsymbol{\sigma}_{o,b} \end{aligned} \tag{4.28}$$

where the subscript $e(o)$ indicate that the term is symmetric(antisymmetric). Terms in Eq. (4.28) are defined as follows:

The component $\boldsymbol{\sigma}_{e,0}$ is an ordinary pressure-like term. Using I to denote the identity matrix, $\boldsymbol{\sigma}_{e,0}$ reads

$$\boldsymbol{\sigma}_{e,0} = \langle g_0 \rangle_{\parallel} I. \tag{4.29}$$

The component $\boldsymbol{\sigma}_{e,b}$ describes a symmetric stress induced by dilation, from which bulk viscosity is extracted as $\left\langle m^b \right\rangle_{\parallel}$.

$$\boldsymbol{\sigma}_{e,b} = \left\langle m^b \right\rangle_{\parallel} (\nu_{xx} + \nu_{yy}) I. \tag{4.30}$$

The component $\boldsymbol{\sigma}_{e,s}$ describes the stress from shear viscosity η_s,

$$\boldsymbol{\sigma}_{e,s} = \eta_{\mathrm{s}} \begin{pmatrix} \nu_{xx} - \nu_{yy} & 2\nu_{xy} \\ 2\nu_{yx} & \nu_{yy} - \nu_{xx} \end{pmatrix}, \tag{4.31}$$

$$\eta_s \equiv \left\langle r^2 m^s/2 \right\rangle_{\parallel} - \left\langle r^2 m^a/2 \right\rangle_{\perp}. \tag{4.32}$$

The component $\boldsymbol{\sigma}_{e,a}$ describes the stress from odd viscosity η_a,

$$\boldsymbol{\sigma}_{e,a} = \eta_a \begin{pmatrix} -(\nu_{xy} + \nu_{yx}) & \nu_{xx} - \nu_{yy} \\ \nu_{xx} - \nu_{yy} & \nu_{xy} + \nu_{yx} \end{pmatrix}, \tag{4.33}$$

$$\eta_a \equiv \left\langle r^2 m^s/2 \right\rangle_{\perp} + \left\langle r^2 m^a/2 \right\rangle_{\parallel}. \tag{4.34}$$

The odd viscosity is so-called because its tensor form η_{ijkl}, which relates the even part of stress and strain rate through $\sigma_{e,ij} = \eta_{ijkl}\nu_{kl}$, is antisymmetric $\eta_{ijkl} = -\eta_{klij}$ [99]. For isotropic systems, the antisymmetric tensor has only one independent component [99], which we simply call the odd viscosity coefficient. This odd viscosity, unlike the conventional shear viscosity, does not lead to dissipation [98]. The existence of odd viscosity is associated with the notion of time-reversal symmetry breaking [99, 104]. In the chiral active fluids considered here, which are isotropic and achiral when not driven, time-reversal acts by changing the

sign of the torque applied to each rotor. Under this operation, $\bar{F}_{\parallel}$ and m^s remain unchanged, while $\bar{F}_{\perp}$ and m^a change sign. Hence, odd viscosity η_a from Eq. (4.34) is odd under time-reversal, whereas shear viscosity η_s from Eq. (4.32) is even.

The terms $\boldsymbol{\sigma}_{o,0}$ and $\boldsymbol{\sigma}_{o,r}$ describe two antisymmetric components of the stress tensor, one is static and one reflects a response to vortical flows,

$$\boldsymbol{\sigma}_{o,0} + \boldsymbol{\sigma}_{o,r} = \left(\langle g_0 \rangle_{\perp} + \langle m^r \rangle_{\perp} \omega\right) \begin{pmatrix} 0 & -1 \\ 1 & 0 \end{pmatrix}. \tag{4.35}$$

The component $\boldsymbol{\sigma}_{e,r}$ describes a diagonal stress that responds to vortical flows,

$$\boldsymbol{\sigma}_{e,r} = \langle m^r \rangle_{\parallel} \omega I. \tag{4.36}$$

Finally, the component $\boldsymbol{\sigma}_{o,b}$ describes another antisymmetric part of the stress tensor, which responds to dilations,

$$\boldsymbol{\sigma}_{o,b} = \left\langle m^b \right\rangle_{\perp} (\nu_{xx} + \nu_{yy}) \begin{pmatrix} 0 & -1 \\ 1 & 0 \end{pmatrix}. \tag{4.37}$$

Note that terms containing m^b, m^s or $\langle \cdot \rangle_{\parallel}$ exist even in regular achiral liquids, whereas terms containing m^a, m^r or $\langle \cdot \rangle_{\perp}$ are specific to chiral fluids. For ordinary achiral liquids, m^a, m^r and $\langle \cdot \rangle_{\perp}$ vanish, and the terms in the stress expression reduce to the usual pressure, bulk viscosity, and shear viscosity. For chiral liquids, however, all these terms are possible. In particular, the odd viscosity coefficient η_a has two contributions, one from the perpendicular force acting on the ordinary distortion of $g(\boldsymbol{x})$, and the other from the ordinary parallel force acting on the anomalous distortion of $g(\boldsymbol{x})$. We also see that the shear viscosity gets modified by $\left\langle r^2 m^a/2 \right\rangle_{\perp}$, which comes from the perpendicular force acting on the anomalous distortion of $g(\boldsymbol{x})$.

We briefly compare our components of stress tensor with the literature. Terms Eq. (4.29)-

(4.35) agree well with Ref. [98], where transport properties were derived starting from hydrodynamic equations. We also obtain two additional terms, Eq. (4.36),(4.37). Including these two terms, we found six coefficients that relate stress tensor and velocity gradients. This result is consistent with Ref. [162], in which there is a derivation of a generalized viscosity tensor that satisfies isotropy condition. Odd viscosity including anisotropic effects is studied in Ref. [163].

4.4 Numerical simulations of a model active rotor system

In this section, we present results from numerical simulation of a model active rotor system. First, we perform numerical simulations in the absence of any imposed gradients in the velocity fields (Sec. 4.4.1), and show that the orientation-averaged inter-rotor forces can contain a perpendicular component. Next, from the simulation of rotors under an imposed shear flow (Sec. 4.4.2), we show the orientation-averaged intermolecular forces do not change under this flow field for our model rotor system. We also show in Sec. 4.4.2 that the distortion of pair correlation function to linear order in $\partial_k u_l$ is well described by the modes Eq. (4.23)-(4.25). Thus, the above described procedure for extracting transport coefficients can be applied to our system. Consequently in Sec. 4.4.2, we obtain numerical estimates of the various transport coefficients using the averaged force and $g(\boldsymbol{x})$-distortions extracted from the simulations.

4.4.1 Perpendicular component of the orientation-averaged force

The rotors in our model chiral active liquid are constructed using nine beads held fixed relative to one another in a set geometry. Beads belonging to different rotors interact via a Gaussian potential $V(r) = \epsilon e^{-r^2/2\sigma^2}, \sigma = 0.25a$, where ϵ sets the energy scale, and a denotes the length-scale of each rotor. In Figure 4.3 we plot the superposition of the Gaussian potential from the nine beads in a rotor. The dynamics of each bead in the rotors are

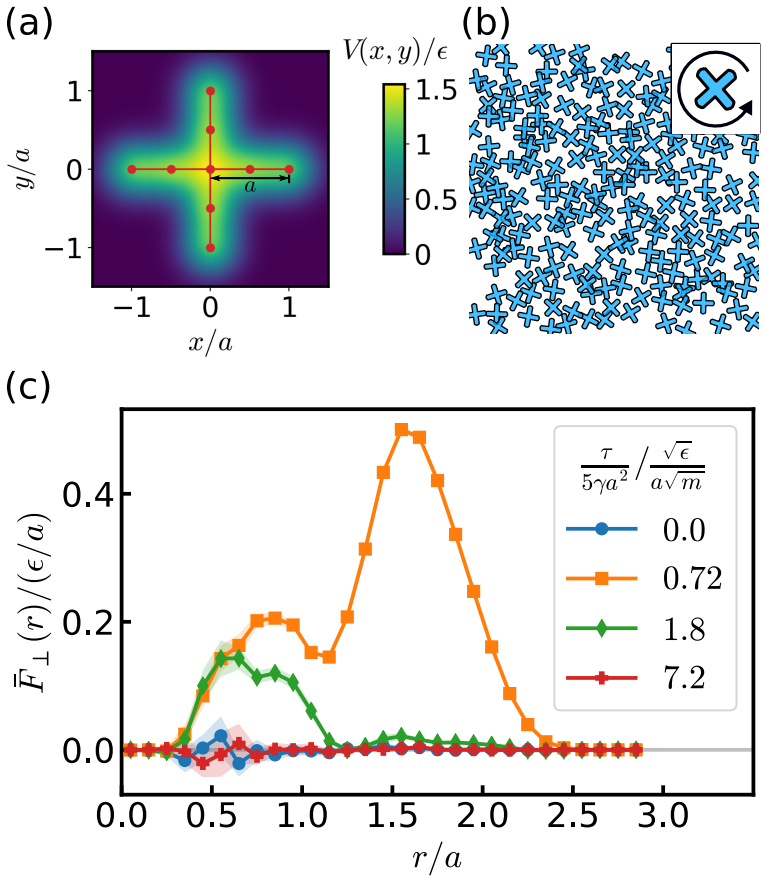

Figure 4.3: Transverse components in the orientation-averaged intermolecular forces. (a) The inter-rotor potential used in our numerical simulations. Each rotor is simulated by nine beads, which are labeled as red dots. Beads belonging to different rotors interact via a Gaussian potential $V(r) = \epsilon e^{-r^2/2\sigma^2}, \sigma = 0.25a$. The figure plots the superposition of the Gaussian potential from the nine beads. (b) A snapshot of a section of the simulation system. Each rotor is driven in a counter-clockwise direction. (c) Perpendicular component of the averaged inter-rotor forces at different torques. Shaded region around each curve represent 95% confidence interval. τ is the external torque, and $\tau/5\gamma a^2$ is the average angular velocity of rotors under the external torque when the rotors are non-interacting.

simulated using underdamped Langevin dynamics. The molecular dynamics simulations were performed using LAMMPS package [164] with Moltemplate toolkit [165] and custom code. The friction of Langevin dynamics γ is set to $\gamma = 0.5\sqrt{m\epsilon}/a$, where m is the mass of each bead, and the temperature is ϵ/k_B. Timestep is set to $0.0004a\sqrt{m/\epsilon}$. The numerical results described below were obtained from simulations performed with $N = 900$ rotors in a simulation box with dimensions $60a \times 60a$ (Figure 4.3b). The simulations were performed with periodic boundary conditions. A constant counter-clockwise torque τ is applied to each rotor. When applied to a single rotor, this torque would cause the rotor to rotate with an averaged angular velocity $\omega_0 = \tau/5\gamma a^2$. We performed simulations with multiple values of applied torque, $\tau/\epsilon = 0, 1.8, 4.5, 18$. For each value of torque, we collected data from 10 steady-state trajectories, each with length $2000a\sqrt{m/\epsilon}$.

The perpendicular component of the orientation-averaged forces computed from simulations are plotted in Figure 4.3c. For this particular rotor model, significant $\bar{F}_\perp(\boldsymbol{x})$ emerges at intermediate torques ($\omega_0/\sqrt{\epsilon/ma^2} = 0.72, 1.8$) before decreasing to vanishingly small values at large torques ($\omega_0/\sqrt{\epsilon/ma^2} = 7.2$).

4.4.2 Simulation of rotors under a flow field

The simulation setup of this subsection is the same as the one in Sec. 4.4.1, except that an additional external force $F_y/\sqrt{\epsilon/m} = 9\gamma\lambda x/a$ is applied to the center of mass of each rotor. This applied external force creates a simple shear in the region around $x = 0$. Rotors' averaged velocity in y-direction satisfies $u_y/\sqrt{\epsilon/m} = F_y/9\gamma = \lambda x/a$ (Figure 4.4a, except for rotors close to the left and right boundaries). The simulation parameters are identical to the ones used in Sec. 4.4.1, except that the torque applied on each rotor is set to $\tau = 1.8\epsilon$, and we vary the value of λ for different set of simulations. We collected data from steady-state trajectories of length $2000a\sqrt{m/\epsilon}$. We computed the averaged inter-rotor forces using 10 trajectories while we used 100 trajectories to compute the $g(\boldsymbol{x})$-distortions. For the purposes of these computations we only include rotors in the middle region of the simulation box in

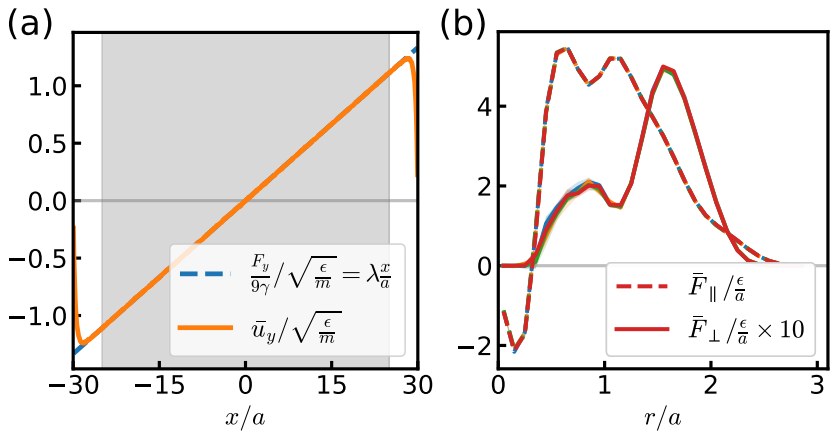

Figure 4.4: Averaged parallel and perpendicular force from simulated rotor systems under a flow field. (a) Profile of applied external force F_y and the measured averaged velocity u_y in y-direction. Data is shown for $\lambda = 0.0444$. Due to periodic boundary condition, u_y close to the boundary $|x| = 30a$ decreases to zero. Calculation of inter-rotor forces only include rotors whose center of masses are inside the shaded region ($|x| < 25a$), where the averaged velocity is linear in x. (b) $\bar{F}_\parallel(r)$ and $\bar{F}_\perp(r)$ for $\lambda = 0, 0.0222, 0.0444, -0.0444$. $\bar{F}_{\parallel/\perp}(r)$ at different λ's basically overlap, which shows that small applied flow fields do not induce significant changes in $\bar{F}_{\parallel/\perp}(r)$. To avoid overcrowding the plot, legends for colors corresponding to different λ's are not shown. Shaded region around each curve represent 95% confidence interval, which is small compared with the line width.

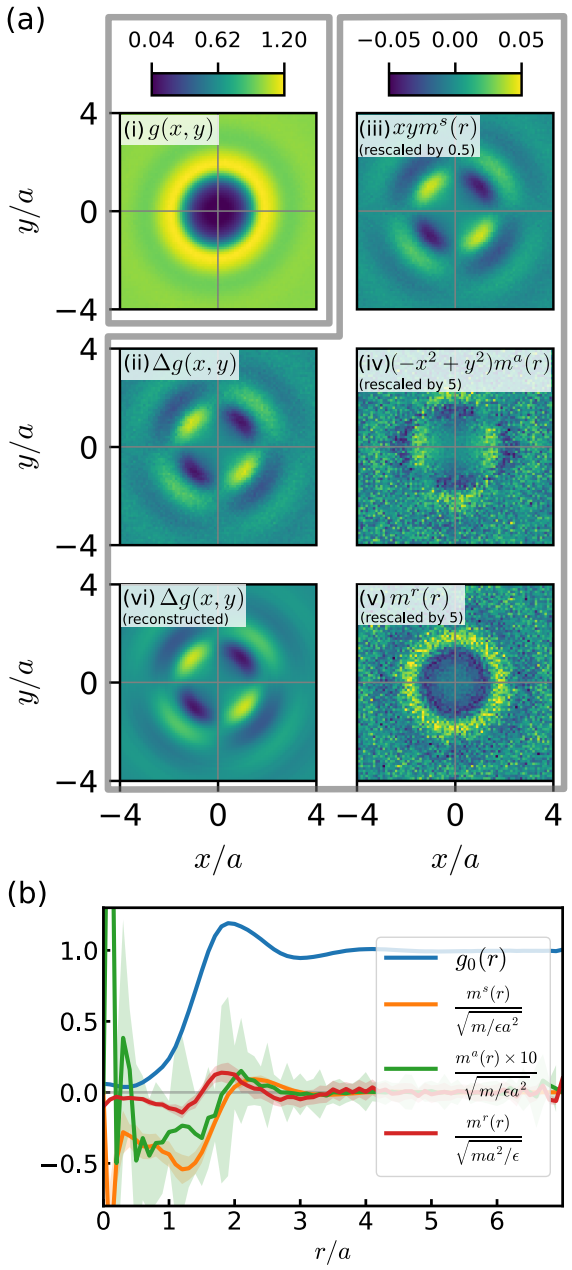

Figure 4.5: Distortion of the pair correlation function induced by a simple shear flow field. (a) $g(x,y)$ under a simple shear flow $\partial_x u_y = 0.0444\sqrt{\epsilon/ma^2}$ is distorted to an elliptical shape (i). Apparently, the distortion $\Delta g(x,y)$ (ii) is slightly rotated counter-clockwisely compared with that in ordinary liquids. (iii) plots the mode $(\Delta g(x,y) - \Delta g(x,-y))$, which is proportional to $xym^s(r)$, and is labeled by $xym^s(r)$ for simplicity. The data is rescaled by a factor of 0.5 to accommodate the scale of the colorbar. The other two modes, $(\Delta g(x,y) - \Delta g(y,x)) \propto (-x^2+y^2)m^a(r)$ and $(\Delta g(x,-y)+\Delta g(y,x)) \propto m^r(r)$ are plotted in (iv) and (v), respectively. The $\Delta g(x,y)$ reconstructed from the fitted $m^{s,a,r}(r)$ (vi) agrees well with $\Delta g(x,y)$ directly computed from simulation (iii). (b) $m^{s,a,r}(r)$ fitted from the data in (a). Shaded region around each curve represent the standard deviation of residues at each r.

Figure 4.4(a), where the velocity gradient $\partial_x u_y = \lambda\sqrt{\epsilon/ma^2}$ is constant. In more detail, the x-coordinate of the center of mass of each rotor considered for our analysis is within $[-25a, 25a]$ for computing inter-rotor forces, and is within $[-20a, 20a]$ for computing $g(\boldsymbol{x})$.

The averaged inter-rotor forces computed from simulations are described in Figure 4.4(b). We see that there is no significant change in the averaged intermolecular forces for various values of λ. Hence, the technique outlined in Sec. 4.3 can be used to obtain estimates of the various transport coefficients.

Extracting deformations in the pair correlation functions due to imposed flow: results from numerical simulations

The distortion of pair correlation function induced by a flow field can be extracted as follows. The simple shear flow we imposed is a superposition of pure shear and vortical flows, $\partial_x u_y = \nu_{xy} + \omega$, and according to Eq. (4.21)-(4.25), the ansatz of $g(\boldsymbol{x})$-distortion reads

$$\Delta g(\boldsymbol{x}) = \partial_x u_y[2xym^s(r) + (-x^2 + y^2)m^a(r) + \frac{1}{2}m^r(r)], \tag{4.38}$$

$$\Delta g(\boldsymbol{x}) = \frac{1}{2}(g(\boldsymbol{x}; \partial_x u_y) - g(\boldsymbol{x}; -\partial u_y)). \tag{4.39}$$

Here $\Delta g(\boldsymbol{x})$ is calculated using $g(\boldsymbol{x})$'s under both $\partial_x u_y$ and $-\partial_x u_y$ in order to eliminate possible quadratic terms ($\propto (\partial_x u_y)^2$). At the flow field magnitude we used in simulation ($\lambda = 0.0444$), these quadratic terms do contribute to the $g(\boldsymbol{x})$-distortion. Smaller flow field magnitudes are not adopted because they produce poor signal-to-noise ratios, and in fact, they are not required because, as we will show below, the linear distortions can already be extracted from $\Delta g(\boldsymbol{x})$. Utilizing symmetries of Eq. (4.38), the distortion modes can be

computed as

$$m^s(r) = \frac{1}{4xy\partial_x u_y}(\Delta g(x,y) - \Delta g(x,-y)), \tag{4.40}$$

$$m^a(r) = \frac{1}{2(-x^2+y^2)\partial_x u_y}(\Delta g(x,y) - \Delta g(y,x)), \tag{4.41}$$

$$m^r(r) = \frac{1}{\partial_x u_y}(\Delta g(x,-y) + \Delta g(y,x)). \tag{4.42}$$

Numerically, division by xy or $(-x^2+y^2)$ is not favored because their values can be zero. Our actual procedure was to first compute $\Delta g(x,y) - \Delta g(x,-y)$, then find $m^s(r)$ such that $xym^s(r)$ best fits this computed data.

Simulated $g(\boldsymbol{x})$-distortion and its modes are shown in Figure 4.5. We see that $\Delta g(x,y)$ reconstructed from fitted $m^{s,a,r}(r)$ agree well with $\Delta g(x,y)$ directly computed from simulated data (Figure 4.5(a-ii,vi)). This agreement justifies the ansatz of $\Delta g(\boldsymbol{x})$ in Eq. (4.38), which means that we can ignore higher order terms like $x_{i1}x_{i2}x_{i3}x_{i4}\partial_k u_l$ (as discussed in Ref. [161]) and $(\partial_k u_l)^3$. Notably, the simulation results show that the anomalous $g(\boldsymbol{x})$-distortions described by $(-x^2+y^2)m^a(r)$ and $m^r(r)$ do exist in our parity symmetry-breaking rotor system.

Numerical estimates of transport coefficients

With the averaged inter-rotor forces $\bar{F}_{\parallel/\perp}(r)$ and the modes of $g(\boldsymbol{x})$-distortion $m^{s,a,r}(r)$, we can compute the transport coefficients according to Eq. (4.29)-(4.36). For our model rotor system, the two contributions to the odd viscosity dictated by Eq. (4.34) are

$$\left\langle m^s r^2/2 \right\rangle_\perp = (0.0220 \pm 0.0005)\sqrt{m\epsilon/a^2}, \tag{4.43}$$

$$\left\langle m^a r^2/2 \right\rangle_\parallel = (0.010 \pm 0.003)\sqrt{m\epsilon/a^2}, \tag{4.44}$$

which produce an odd viscosity of $(0.032 \pm 0.003)\sqrt{m\epsilon/a^2}$. Note that the two terms contributing to odd viscosity are on the same order of magnitude, so we cannot simply ignore

either one. For comparison, the two contributions to the shear viscosity dictated by Eq. (4.32) are

$$\left\langle m^s r^2/2 \right\rangle_{\parallel} = (0.210 \pm 0.004)\sqrt{m\epsilon/a^2}, \tag{4.45}$$

$$\left\langle m^a r^2/2 \right\rangle_{\perp} = (0.0009 \pm 0.0005)\sqrt{m\epsilon/a^2}, \tag{4.46}$$

which produce a shear viscosity of $(0.209 \pm 0.004)\sqrt{m\epsilon/a^2}$. Compared to $\left\langle m^s r^2/2 \right\rangle_{\parallel}$, the term $\left\langle m^a r^2/2 \right\rangle_{\perp}$ is negligible. The ratio of odd viscosity to shear viscosity is 0.15 ± 0.01. Finally another anomalous transport property, the antisymmetric stress (Eq. (4.35)) for our rotor model evaluates to

$$\langle g_0 \rangle_{\perp} = (-0.09327 \pm 0.00007)\epsilon/a^2, \tag{4.47}$$

$$\langle m^r \rangle_{\perp} = (-0.0052 \pm 0.0004)\sqrt{m\epsilon/a^2}. \tag{4.48}$$

4.5 Conclusion

In conclusion, we have provided a mechanism for how anomalous transport coefficients can emerge in chiral active fluids. The central results of our work are formulated in Eq. (4.28)-(4.37). In particular, we introduced an orientation-averaged intermolecular force, derived four allowed distortion modes of the pair correlation function in a flow field, and showed how a perpendicular component in the orientation-averaged force and the anomalous distortions of $g(\boldsymbol{x})$ combine to produce anomalous transport coefficients such as odd viscosity. By decomposing the contribution to transport coefficients in terms of averaged forces and distortions of $g(\boldsymbol{x})$, we have provided a microscopic perspective to understand these transport properties. In future work, we expect to investigate computationally or experimentally how the molecular structure and intermolecular interactions in chiral active liquids affect $\bar{\boldsymbol{F}}(\boldsymbol{x})$ and $g(\boldsymbol{x})$-distortion, thus determining the transport properties.

CHAPTER 5

SUMMARY AND OUTLOOK

In summary, we have studied anomalous transport behaviors in a few classes of chiral nonequilibrium systems. In Chapter 2 we demonstrated energy rectification between nodes in a class of active gyroscopic networks and developed a diagrammatic approach to understand and control the rectification. In Chapter 3 we demonstrated energy rectification between nodes and baths in a class of time-modulated active gyroscopic networks and combined MSR/JDP formalism with our diagrammatic approach to understand the rectification. These two efforts together covered two basic forms of energy transport in network-type systems, i.e. transport between nodes and transport between nodes and baths, thus providing a comprehensive understanding of energy rectification in networks systems. In Chapter 4 we extended the Irving-Kirkwood approach to describe transport properties of chiral active fluids, and found connections between anomalous transport coefficients and molecular properties. Taken together, our studies have contributed to the topic of anomalous transport of energy and momentum. Our analytic theories provide frameworks to understand complex transport behaviors in terms of relatively simple local properties.

Following questions can be asked based on our work described in the previous chapters. (1) For active gyroscopic networks, we have seen in Chapter 3 that a time-modulated B-field induces couplings between different Fourier modes of the response function, which leads to rectification. Another way to induce mode coupling is to introduce nonlinearities. It would be interesting to see whether nonlinearities can indeed generate rectifications. If so, whether the combined MSR/JDP and diagrammatic approach can be practically applied to such conditions. If so, what the diagrams look like and what relations between global network and local properties can be obtained. (2) From numerical calculations of energy fluxes in active gyroscopic networks, both unmodulated and time-modulated, we see that if the characteristic energy scale (strength of the colored noise) is fixed, the magnitude of the energy flux seems to be bounded by some value, no matter how we change the parameters

(data are not presented in this thesis). It could be interesting to ask what this maximum depends on. We have shown in Chapter 2 that the energy flux is not related to the entropy production rate, but it does not exclude the possibility of finding another quantity to bound the energy fluxes. (3) In Chapter 4 we have derived theoretical expressions for transport coefficients, it would be interesting to see how the molecular structure affect the distortion of pair correlation function and the average intermolecular forces. In particular, it is not clear whether the shear viscosity can be tuned to negative values or whether non-active chiral molecules can exhibit odd viscosity.

Looking forward, I expect to see more interesting studies in the field of active matter. I expect opportunities provided by discrete active systems, e.g. networks, where we can potentially utilize the flexible geometric structures to explore physics phenomena [166, 111]. It would also be intriguing to use active matter to realize more exotic functions, such as computing [167] or information processing [168].

APPENDIX A

DERIVATIONS RELATED TO ACTIVE GYROSCOPIC NETWORKS

A.1 Derivation of energy flux formula

In this section, we derive the formula for energy flux, Eq. (2.4) in the main text. The force F in this section is a general conservative force, which does not need to be linear. We use the following strategy to determine the energy flux. First we define the energy E_i of particle i, and then write down an energy balance relation, that expresses the infinitesimal energy change $\mathrm{d}E_i$ using stochastic calculus. Finally, we collect terms in $\mathrm{d}E_i$ that couple neighboring particles together and identify them as the energy transfer between particles.

The energy of particle i is defined as

$$E_i = \frac{1}{2} m_i v_i^T v_i + U_{ii} + \frac{1}{2} \sum_{j \neq i} U_{ij}, \tag{A.1}$$

where the first term is the kinetic energy, the second term denotes the on-site potential, and the last term is the shared spring energy between the particle and its neighbors.

We use Ito's formula to calculate $\mathrm{d}E_i$. Ito calculus provides the advantage that the stochastic terms in $\mathrm{d}E_i$ vanish under time-averaging. For a stochastic differential equation (SDE) of variable X(vector) with drift μ(vector) and diffusion σ(matrix)

$$\mathrm{d}X = \mu \mathrm{d}t + \sigma \mathrm{d}W, \tag{A.2}$$

where $\mathrm{d}W$ is a vector consisting of standard Wiener processes, Ito's formula gives the SDE of function $f(X)$

$$\mathrm{d}f(X) = ((\nabla_X^T f)\mu + \frac{1}{2} \mathrm{tr}\Big[\sigma\sigma^T \nabla_X \nabla_X^T f\Big])\mathrm{d}t + (\nabla_X^T f)\sigma \mathrm{d}W, \tag{A.3}$$

where ∇_X denotes the gradient with respect to X, the superscript T denotes the transpose, and tr denotes the trace.

We begin by writing the equation of motion of our system Eq. (2.1) in the form of a stochastic differential equation Eq. (A.2). We represent N particles' position by a column vector $z = \sum_{i=1}^{N} |i\rangle \otimes z_i$, where $|i\rangle$ denotes the $2D$ subspace of particle i. Similar representations are also applied to v and η. Then we get

$$X = \begin{pmatrix} z & v & \eta \end{pmatrix}^T, \tag{A.4}$$

$$\mu = \begin{pmatrix} v \\ \frac{1}{m}(-\nabla_z U - BAv - \gamma v + \eta) \\ -\frac{1}{\tau}\eta \end{pmatrix}, \tag{A.5}$$

$$\sigma = \mathrm{diag}\begin{pmatrix} 0 & 0 & \frac{\sqrt{2\gamma T_a}}{\tau} I \end{pmatrix}, \tag{A.6}$$

where U is the total energy of the system, A is an antisymmetric matrix $A = \sum_i |i\rangle\langle i| \otimes A_1$, and diag$(\cdot)$ means a block-diagonal matrix.

Now we apply Ito's formula Eq. (A.3) to our system by associating with the function $f(X)$, the energy of particle i, $E_i(X)$. The nonzero terms in the gradient of E_i are

$$\nabla_{z_i} E_i = -(F_{ii} + \frac{1}{2}\sum_j F_{ji}), \tag{A.7}$$

$$\nabla_{z_j} E_i = -\frac{1}{2} F_{ij}, \tag{A.8}$$

$$\nabla_{v_i} E_i = m_i v_i. \tag{A.9}$$

The term $(\nabla_X^T E_i)\mu$ reads

$$(\nabla_X^T E_i)\mu = -\sum_j \frac{1}{2}(v_i + v_j)^T F_{ij} - \gamma v_i^T v_i + v_i^T \eta_i, \tag{A.10}$$

where we used $F_{ji} = -F_{ij}$ and $v_i^T A v_i = 0$ in its derivation. The term $\frac{1}{2}\,\mathrm{tr}\left[\sigma\sigma^T \nabla_X \nabla_X^T f\right]$ and $\nabla_X^T f$ are zero.

Finally, the energy change can be written as

$$\mathrm{d}E_i = -\sum_j J_{ij}\mathrm{d}t + h_i \mathrm{d}t, \tag{A.11}$$

$$J_{ij} = \frac{1}{2}(v_i + v_j)^T F_{ij}, \tag{A.12}$$

$$h_i = -\gamma_i v_i^T v_i + v_i^T \eta_i. \tag{A.13}$$

J_{ij} is identified as the energy transferred per unit time from particle i to j, and h_i is identified as the energy transferred from the bath to particle i.

As for the steady-state average of J_{ij}, we use $\left\langle \mathrm{d}U_{ij}/\mathrm{d}t = 0 \right\rangle$ and the chain rule to simplify Eq. (A.12)

$$0 = v_i^T F_{ji} + v_j^T F_{ij} = -v_i^T F_{ij} + v_j^T F_{ij}, \tag{A.14}$$

and arrive at the expression

$$\left\langle J_{ij} \right\rangle = \left\langle v_j^T F_{ij} \right\rangle. \tag{A.15}$$

One straightforward numerical method to compute the flux J is as follows. Our system is determined by the network geometry and parameters $m, k_g, k, B, \gamma, \tau, T_a$. Given the equation of motion Eq. (A.2),(A.4)-(A.6), one can numerically solve for the covariance $C = \left\langle XX^T \right\rangle$ from the matrix equation $(-\mu)C + C(-\mu^T) = \sigma\sigma^T$ [117, 118]. Finally, the flux Eq. (A.12), which is bilinear in x and v, can be extracted from the covariance C. Numerical calculations of $\langle J \rangle$ are performed using Mathematica with custom code [169].

A.2 Linear response theory for energy flux

Following Ref. [119], we derive the expression of the energy flux (Eq. (2.7) and (2.10) in the main text) using a spectral linear response theory.

A.2.1 Fourier modes for energy flux

We define Fourier transform (FT) of a function $f(t)$ as

$$\tilde{f}(\omega) = \frac{1}{t}\int_0^t dt' \; f(t')e^{-i\omega t'}, \quad \omega = \frac{2\pi n}{t}, \tag{A.16}$$

$$f(t) = \sum_{\omega=-\infty}^{\infty} \tilde{f}(\omega)e^{i\omega t}, \tag{A.17}$$

where $n = -\infty, \ldots, -1, 0, 1, 2, \ldots, \infty$.

The FT of the equation of motion Eq. (A.2),(A.4)-(A.6) reads

$$\tilde{v}(\omega) = i\omega\tilde{z}(\omega), \tag{A.18}$$

$$\tilde{z}(\omega) = G^+(\omega)\tilde{\eta}(\omega), \tag{A.19}$$

$$\tilde{\eta}(\omega) = \frac{\sqrt{2\gamma T_a}}{1+i\omega\tau}\tilde{\xi}(\omega), \tag{A.20}$$

where G^+ is the response function

$$G^{\pm}(\omega) = [K \pm i\omega(\gamma I + BA) - m\omega^2 I]^{-1}. \tag{A.21}$$

To make our results more general, we consider a general noise when possible, and describe it by the noise spectrum

$$\left\langle \tilde{\eta}(\omega)\tilde{\eta}(\omega')^T \right\rangle = \frac{2\gamma T_a}{t} h(\omega) I \delta_{\omega+\omega',0}, \tag{A.22}$$

where $h(\omega)$ is a function that describes the shape of the spectrum. For white noise, $h(\omega) = 1$. For OU colored noise, $h(\omega) = 1/(1+\omega^2\tau^2)$.

The energy flux J_{ij} from Eq. (A.12) can be expressed as a bilinear function in z and v,

by writing the linearized force F in terms of z,

$$J_{ij} = kv^T A^J z \tag{A.23}$$

$$\begin{aligned} A^J \equiv \frac{1}{2}(&|i\rangle\langle i| \otimes e_{ij}e_{ij}^T + |i\rangle\langle j| \otimes e_{ij}e_{ji}^T \\ &+ |j\rangle\langle i| \otimes (-e_{ji}e_{ij}^T) + |j\rangle\langle j| \otimes (-e_{ji}e_{ji}^T)). \end{aligned} \tag{A.24}$$

This bilinear form enables us to write the time integral of energy flux $Q = \int_0^t \mathrm{d}t'\, J(t')$ as a sum of Fourier modes $\tilde{q}_\omega$ using Parseval's theorem,

$$Q = t \sum_{\omega=-\infty}^{\infty} \tilde{q}_\omega, \tag{A.25}$$

$$q_\omega = k\tilde{v}^T A^J \tilde{z}^* = i\omega k \tilde{\eta}^T G^{+T} A^J G^- \tilde{\eta}^*, \tag{A.26}$$

where the superscript $*$ denotes the complex conjugate.

Pairing $\tilde{q}_\omega$ and its conjugate $\tilde{q}_{-\omega}$ gives a real function, which would be beneficial for subsequent derivations.

$$Q = t \sum_{\omega=2\pi/t}^{\infty} (\tilde{q}_\omega + \tilde{q}_{-\omega}), \tag{A.27}$$

$$\tilde{q}_\omega + \tilde{q}_{-\omega} = \tilde{\eta}(\omega)^T A^q_\omega \tilde{\eta}(\omega)^* \tag{A.28}$$

$$A^q_\omega = -i\omega k G^+(\omega)^T A^{as} G^-(\omega), \tag{A.29}$$

$$A^{as} = -(A^J - A^{J^T}) \tag{A.30}$$

$$= -|i\rangle\langle j| \otimes e_{ij}e_{ji}^T + |j\rangle\langle i| \otimes e_{ji}e_{ij}^T. \tag{A.31}$$

Averaging $\tilde{q}_\omega + \tilde{q}_{-\omega}$ over the noise $\tilde{\eta}(\omega)$, we get

$$\langle \tilde{q}_\omega + \tilde{q}_{-\omega} \rangle = \frac{2\gamma T_a}{t} h(\omega)\, \mathrm{tr}\, A^q_\omega. \tag{A.32}$$

A.2.2 Integrating over the Fourier modes

In long time limit, the sum can be approximated by an integral

$$\frac{1}{t}\sum_{\omega=2\pi/t}^{\infty} = \frac{1}{2t}\sum_{\omega=-\infty}^{\infty}\frac{t\Delta\omega}{2\pi} \approx \frac{1}{4\pi}\int_{-\infty}^{\infty}\mathrm{d}\omega\,. \tag{A.33}$$

Eq. (A.27) and (A.32) can then be turned to an integral expression of the flux

$$\langle J\rangle = \lim_{t\to\infty}\frac{\langle Q\rangle}{t} = \frac{\gamma T_a}{2\pi}\int_{-\infty}^{\infty}\mathrm{d}\omega\, h(\omega)\,\mathrm{tr}\,A^q_\omega. \tag{A.34}$$

In the next steps, we simplify this integral with the help of the property from Ref. [119]

$$G^-(\omega) - G^+(\omega)^T = 2i\omega\gamma G^-(\omega)G^+(\omega)^T. \tag{A.35}$$

Using this property, the trace of A^q_ω becomes

$$\begin{aligned}\mathrm{tr}\,A^q_\omega &= -i\omega k\,\mathrm{tr}\,G^{+T}A^{as}G^-\\ &= -i\omega k\frac{1}{2i\omega\gamma}\,\mathrm{tr}\Big(G^- - G^{+T}\Big)A^{as}\\ &= -\frac{k}{\gamma}\,\mathrm{Re}\,\mathrm{tr}\,G^+A^{as}.\end{aligned} \tag{A.36}$$

Plugging this trace into Eq. (A.34), we get the integral form for the flux Eq. (2.7)

$$\langle J\rangle = -\frac{T_a k}{2\pi}\int_{-\infty}^{\infty}\mathrm{d}\omega\, h(\omega)\,\mathrm{Re}\,\mathrm{tr}\,G^+A^{as}. \tag{A.37}$$

Since $\mathrm{Im}\,G^+(-\omega) = -\,\mathrm{Im}\,G^+(\omega)$, $h(\omega)\,\mathrm{Im}\,\mathrm{tr}\,G^+A^{as}$ is an odd function of ω, and its line integral vanishes,

$$\langle J\rangle = -\frac{T_a k}{2\pi}\int_{-\infty}^{\infty}\mathrm{d}\omega\, h(\omega)\,\mathrm{tr}\,G^+A^{as}.. \tag{A.38}$$

The difference between this expression and Eq. (A.37) is that, the integrand of (A.37) is real at all ω's, whereas the integrand of Eq. (A.37) is complex. We adopt Eq. (A.37) in the main

text, so that its integrand can be interpreted as the flux of Fourier modes.

We now consider the specific OU colored noise, $h(\omega) = 1/(1+\omega^2\tau^2)$. In this case, the integral Eq. (A.38) can be calculated using the residue theorem. The integrand vanishes at $\omega \to \infty$, so the line integral can be converted to a contour integral along the counter-clockwise semicircle R in the lower-half plane

$$\langle J \rangle = \frac{T_a k}{2\pi} \oint_R \mathrm{d}\omega \, \frac{\mathrm{tr}\, G^+ A^{as}}{1+\omega^2\tau^2}. \tag{A.39}$$

The $\mathrm{tr}\, G^+ A^{as}$ part in the integrand has no pole in the lower-half plane, because G^+ is a linear response function, and it satisfies causality. However, the noise correlation τ introduces one pole at $\omega = -i/\tau$, thus the contour integral can be evaluated as

$$\langle J \rangle = -\frac{T_a k}{2\tau} \,\mathrm{tr}\, G^+(-\frac{i}{\tau}) A^{as}, \tag{A.40}$$

and the response function at $\omega = -i/\tau$ reads

$$G^+(-\frac{i}{\tau}) = [K + (\frac{\gamma}{\tau} + \frac{m}{\tau^2})I + \frac{B}{\tau}A]^{-1}. \tag{A.41}$$

In theory, Eq. (A.40) provides the analytical solution of the flux, because the inverse matrix Eq. (A.41) can be expressed analytically. In practice, analytical solutions can be easily calculated for small networks, but are impractical for large networks.

Nevertheless, some general properties of the flux can be obtained from Eq. (A.40) after some algebra. For network with only horizontal and vertical bonds (Figure 2.1b), all fluxes are zero. For two networks whose slanted bonds have opposite angles (top and bottom hexagons in Figure 2.1b), their fluxes are opposite. Changing B to $-B$ would change the flux J to $-J$.

A.2.3 Moments of the energy transport

Higher-order moments of the integrated energy flux $Q = \int_0^t \mathrm{d}t'\, J(t')$ can also be calculated following methods in Ref. [119]. We define the moment generating function of Q as $Z(\lambda) = \left\langle e^{\lambda Q} \right\rangle$. In the long time limit, $Z(\lambda)$ can be expressed in the large-deviation form [119], $Z(\lambda) = e^{t\mu(\lambda)}$, where $\mu(\lambda)$ is the so-called rate function. For our system, $Z(\lambda)$ can be calculated through Gaussian integrals. The resulting $\mu(\lambda)$ reads

$$\mu(\lambda) = -\frac{1}{4\pi} \int_{-\infty}^{\infty} \mathrm{d}\omega \ \mathrm{tr} \ln[I + \lambda 2\gamma T_a h(\omega) A^q(\omega)], \tag{A.42}$$

where $A^q(\omega)$ is defined in Eq. (A.29).

The first moment $\langle Q \rangle$ reads

$$\langle Q \rangle = \left. \frac{\partial Z(\lambda)}{\partial(-\lambda)} \right|_{\lambda \to 0} = -t\partial_\lambda \mu(\lambda) \tag{A.43}$$

$$= \frac{t\gamma T_a}{2\pi} \int_{-\infty}^{\infty} \mathrm{d}\omega \ h(\omega) \, \mathrm{tr} \, A^q(\omega), \tag{A.44}$$

which is consistent with the expression in the main text Eq. (2.7).

The fluctuation $\left\langle (\delta Q)^2 \right\rangle = \left\langle Q^2 \right\rangle - \langle Q \rangle^2$ reads

$$\left\langle (\delta Q)^2 \right\rangle = \left. \frac{\partial^2 Z(\lambda)}{\partial(-\lambda)^2} \right|_{\lambda \to 0} - \langle Q \rangle^2 = t\partial_\lambda^2 \mu(\lambda) \tag{A.45}$$

$$= \frac{t(\gamma T_a)^2}{\pi} \int_{-\infty}^{\infty} \mathrm{d}\omega \ h(\omega)^2 \, \mathrm{tr} \Big(A^q(\omega)^2 \Big). \tag{A.46}$$

Plugging in the expression for $A^q(\omega)$ Eq. (A.29), and use the property Eq. (A.35), $\left\langle (\delta Q)^2 \right\rangle$ simplifies to

$$\left\langle (\delta Q)^2 \right\rangle = \frac{t(T_a k)^2}{4\pi} \int_{-\infty}^{\infty} \mathrm{d}\omega \, h(\omega)^2 \, \mathrm{tr} \ (G^- - G^{+T}) A^{as} (G^- - G^{+T}) A^{as} \tag{A.47}$$

In the noninteracting ($k \to 0$) limit, the integrand tends to a nonvanishing constant,

$$\lim_{k\to 0} \frac{\left\langle (\delta Q)^2 \right\rangle}{k^2} = -\frac{tT_a^2}{2\pi} \int_{-\infty}^{\infty} \mathrm{d}\omega \; h(\omega)^2 (g(\omega) - g(-\omega))^2, \tag{A.48}$$

$$g(\omega) = \frac{k_g + i\omega\gamma - m\omega^2}{(k_g + i\omega\gamma - m\omega^2)^2 - (\omega B)^2}. \tag{A.49}$$

This limiting value is independent of the network geometry, thus reflects inherent fluctuations for energy fluxes between two bonded sites regardless of the rest of the network.

A.3 Derivation of Kirchoff's law

The derivation of the Kirchoff's law is similar to the derivation of the energy flux, except that we use the energy from the bath to the particle h_i in Eq. (A.13) instead of J_{ij} in Eq. (A.12).

Following the procedure in the last section from Eq. (A.27) to (A.34), we arrive at an integral expression for the $\langle h_i \rangle$ with a different A_ω^q

$$\langle h_i \rangle = \frac{\gamma T_a}{2\pi} \int_{-\infty}^{\infty} \mathrm{d}\omega \, h(\omega) \operatorname{tr} A_\omega^q, \tag{A.50}$$

$$A_\omega^q = i\omega (G^{+T} \rho_i - \rho_i G^-) - 2\gamma\omega^2 G^{+T} \rho_i G^-, \tag{A.51}$$

$$\rho_i \equiv |i\rangle\langle i| \, . \tag{A.52}$$

Here the noise is kept general.

Using the property of $G^\pm$ Eq. (A.35), we get

$$\begin{aligned} \operatorname{tr}\Big(G^{+T} \rho_i - \rho_i G^- \Big) &= \operatorname{tr} \rho_i (G^{+T} - G^-) \\ &= -\operatorname{tr} \rho_i 2i\omega\gamma G^- G^{+T} \\ &= -2i\omega\gamma \operatorname{tr} G^{+T} \rho_i G^-, \end{aligned} \tag{A.53}$$

so the trace of A^q_ω vanishes

$$\operatorname{tr} A^q_\omega = i\omega \operatorname{tr}\Big(G^{+T}\rho_i - \rho_i G^-\Big) - \operatorname{tr} 2\gamma\omega^2 G^{+T}\rho_i G^- = 0. \tag{A.54}$$

From Eq. (A.50), $\langle h_i\rangle$ is also zero, so on average there is no energy exchange between the particle and the bath. Because the average change of E_i is zero, and $\left\langle \dot{E}_i \right\rangle = -\sum_j \langle J_{ij}\rangle + \langle h_i\rangle$, we obtain the Kirchoff's law

$$-\sum_j \langle J_{ij}\rangle = \sum_j \langle J_{ji}\rangle = 0. \tag{A.55}$$

A.4 A Harada-Sasa relation

We present a Harada-Sasa relation [120] for our active gyroscopic networks, which shows a connection between the fluctuation-response breaking and an entropy production rate. For the calculation of entropy production rate, there has been debates in many literatures on what the reverse process should be, especially for systems in presence of Lorentz-like forces and systems with active particles [170, 171, 172, 173]. Here we simply choose some prescriptions for the reverse process, and show that such choice is consistent with the Harada-Sasa relation.

Within this section, our system is slightly modified by adding an additional white noise ξ_w with correlation $\left\langle \xi_w(t)\xi_w(t')^T \right\rangle = 2\gamma T_a I\delta(t-t')$, and the white noise is uncorrelated with the color noise η. The additional white noise simplifies the discussion of entropy production rate, at the same time it does not affect the energy flux. In order to directly compare our result with Harada-Sasa, we define the Fourier transform as $\tilde{f}(\omega) = \int_{-\infty}^{\infty} \mathrm{d}t\, f(t)e^{-i\omega t}$. This definition is slightly different from the rest of the manuscript, and is restricted within this section. We also keep the colored noise general, $\left\langle \tilde{\eta}(\omega)\tilde{\eta}(\omega')^{*T} \right\rangle = 4\pi\gamma T_a h(\omega)\delta(\omega+\omega')$.

The resulting Harada-Sasa relation reads

$$\dot{s} = \frac{\gamma}{T_a} \int \frac{\mathrm{d}\omega}{2\pi} \operatorname{tr}\Big[\tilde{C}(\omega) - 2T_a \operatorname{Re} \tilde{R}(\omega)\Big], \tag{A.56}$$

where $\dot{s}$ is the entropy production rate, $\tilde{C}(\omega)$ is the velocity correlation, and $\tilde{R}(\omega)$ is the velocity response.

A.4.1 Fluctuation-response breaking

The equation of motion with an additional white noise reads

$$m\dot{v} = -Kz - BAv - \gamma v + \eta + \xi_w. \tag{A.57}$$

The FT of the equation of motion leads to

$$\tilde{v} = i\omega G^+(\omega)(\tilde{\eta} + \tilde{\xi}_w), \tag{A.58}$$

where $G^+(\omega)$ is the same as Eq. (2.6).

The response matrix for velocity reads

$$\tilde{R}(\omega) = i\omega G^+(\omega). \tag{A.59}$$

The velocity correlation in time domain is defined as $C(t) = \Big\langle v(t)v(0)^T \Big\rangle$. To extract a simplified $\tilde{C}$, we use the Fourier transform $\tilde{v}$ (Eq. (A.58)), plug in the noise correlation, and utilize the property of G^+ (Eq. (A.35)), then we get

$$\tilde{C}(\omega) = -2\omega T_a (1 + h(\omega)) \operatorname{Im} G^+. \tag{A.60}$$

Combining Eq. (A.59),(A.60), the breaking of fluctuation-response reads

$$\operatorname{tr}\left[\tilde{C} - 2T_a \operatorname{Re}\tilde{R}\right] = 2i\omega T_a h(\omega) \operatorname{tr} i \operatorname{Im} G^+. \tag{A.61}$$

To simplify its integral, we use the property that $\operatorname{Re} G^+(\omega) = \operatorname{Re} G^+(-\omega)$, and the function $\omega h(\omega) \operatorname{Re} G^+(\omega)$ is odd in ω. So $\int \mathrm{d}\omega\, \omega h(\omega) i \operatorname{Im} G^+ = \int \mathrm{d}\omega\, \omega h(\omega) G^+$, and the result reads

$$\int \frac{\mathrm{d}\omega}{2\pi} \operatorname{tr}\left[\tilde{C} - 2T_a \operatorname{Re}\tilde{R}\right] = \int \frac{\mathrm{d}\omega}{2\pi} 2i\omega T_a h(\omega) \operatorname{tr} G^+. \tag{A.62}$$

A.4.2 Entropy production rate

Following the framework of stochastic thermodynamics [107], the entropy production rate is given by

$$\dot{s} = \lim_{t\to\infty} \frac{1}{t} \log \frac{\mathcal{P}}{\mathcal{P}^\dagger}, \tag{A.63}$$

where $\mathcal{P}$ and $\mathcal{P}^\dagger$ are the probabilities of the forward trajectory and the reverse trajectory.

The propability of the trajectory is given by the Onsager-Machlup path integral [174]

$$\mathcal{P} \propto e^{-\mathcal{A}} \prod_{t'} \delta(\partial_{t'} z - v), \tag{A.64}$$

$$\mathcal{A} = \int_0^t \mathrm{d}t' \, \frac{m^2}{4\gamma T_a} \left| \partial_{t'} v + \frac{\gamma}{m} v - \frac{1}{m} F_p \right|^2, \tag{A.65}$$

$$F_p \equiv -Kz - BAv + \eta. \tag{A.66}$$

For the conjugation trajectory, we choose the prescription that the B-field flips sign, $B^\dagger = -B$ [171], and $\eta^\dagger = \eta$ for the colored noise. With these prescriptions, $\mathcal{P}^\dagger$ and consequently $\dot{s}$ from Eq. (A.63) can be calculated,

$$\dot{s} = -\frac{1}{T_a} \left\langle v^T (m\dot{v} - F_p) \right\rangle. \tag{A.67}$$

We plug in the expression for F_p, find many terms vanish, and get

$$\dot{s} = \frac{1}{T_a} \left\langle v^T \eta \right\rangle = \frac{1}{T_a} \operatorname{tr} \left\langle v \eta^T \right\rangle . \tag{A.68}$$

Expressing v in terms of the response function,

$$\dot{s} = \frac{1}{T_a} \int \frac{\mathrm{d}\omega}{2\pi} \operatorname{tr} i\omega G^+(\omega) 2\gamma T_a h(\omega). \tag{A.69}$$

Compare the entropy production rate Eq. (A.69) and the fluctuation-response breaking Eq. (A.62), we arrive at a Harada-Sasa relation Eq. (A.56).

Note that if we choose the prescription $B^\dagger = B$, the calculated $\dot{s}$ would be different, consequently there would be no Harada-Sasa-like relation. The discrepancy between prescriptions $B^\dagger = -B$ and $B^\dagger = B$ seems to suggest that flipping the B-field should the appropriate prescription from the perspective of relating the fluctuation-response breaking to an entropy production rate.

A.5 Connection of energy flux in active networks to eigenmodes in isolated gyroscopic networks

A.5.1 Presentation of the connection and application to honeycomb lattices

If excluding the active bath, our model is identical to isolated systems studied in Refs. [112, 113, 114, 115]. We would like to build a connection between our energy flux in the active system and eigenmodes in those studies. In this subsection, we show that the flux formula Eq. (2.10) can be decomposed to a weighted sum over eigenmodes Eq. (A.71). Then we apply this result to a honeycomb lattice as an example.

The Fourier analysis from Sec. 2.4 in the main text is not suitable for this connection, because Fourier modes and eigenmodes are related only at small γ's (Figure A.1a and b), but they become dissimilar at larger γ's (Figure A.1a and c). The underlying discrepancy

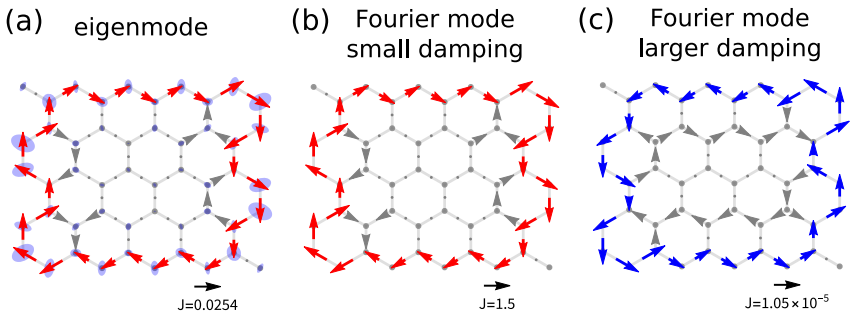

Figure A.1: Comparison between a boundary-localized eigenmode of the undamped isolated network and the Fourier modes of the damped network at the same frequency. First order dynamics (by setting $m = 0$) are used. Numerical calculations are performed with all other parameters set to 1. (a) Eigenmode of undamped gyroscopic system. For the frequency chosen, the eigenmode is localized on the boundary. Blue disks represent the orbit of particles. (b) The Fourier mode of damped variant of our model at small γ ($\gamma = 0.001$) resembles the eigenmode. (c) The Fourier mode at larger γ ($\gamma = 1$) is no longer close to the eigenmode.

between Fourier modes and eigenmodes comes from the fact that eigenmodes are a natural basis for the isolated network, whereas Fourier modes have an extra factor of friction or damping. In addition to this extra factor γ, the active system also has extra factors of m and τ. The factor m comes from the order of dynamics: the active system is second order in time, while the gyroscopic dynamics in Ref. [112] is first order, which corresponds to the $m \to 0$ limit.

Our starting point is Eq. (2.10). The key point is that, in the function $G^+(-i/\tau)$ from the equation, γ, m, τ are not independent factors. Rather, they act collectively through

$$k_{g,\tau} \equiv k_g + \frac{\gamma}{\tau} + \frac{m}{\tau^2}. \tag{A.70}$$

In effect, the extra factors m, γ, τ only add a modification to k_g. Following these ideas, we imagine a reference isolated system with modified on-site spring constant $k_{g,\tau}$. Then after some algebra, the flux $\langle J \rangle$ in active system can be written as a weighted sum of the flux of

each eigenmode $J^{\text{eig}}_{\omega_e}$ in the reference system (see the next section for the derivation),

$$\langle J \rangle = \sum_{\omega_e} \frac{1}{1+\omega_e^2\tau^2} J^{\text{eig}}_{\omega_e}. \tag{A.71}$$

Here ω_e is the discrete eigen-frequency of the reference system, not to be confused with the continuous Fourier frequency ω. The amplitude of eigenmode is set such that its energy is T_a, and $J^{\text{eig}}_{\omega_e}$ is the time-averaged energy flux.

A related result is a so called "sum rule", namely, the unweighted sum of all modes is zero,

$$\sum_{\omega_e} J^{\text{eig}}_{\omega_e} = 0. \tag{A.72}$$

This "sum rule" can be derived from direct calculations (see Appendix A.5.2).

From this eigenmode decomposition, the discussion of time-reversal symmetry in the isolated system [112] immediately carries over to the active system. For network geometries that satisfy time-reversal symmetries, the energy flux of eigenmodes are zero. Thus through Eq. (A.71), the flux in active system is also zero. This result can alternatively be obtained from Eq. (2.10) through some linear algebra.

As an application, we will analyze the flux in the honeycomb network using the eigenmode decomposition Eq. (A.71) and the "sum rule" Eq. (A.72). The flux pattern in the active honeycomb network displays CCW flux localized on the boundary (Figure 2.1b). This localization is reminiscent of the edgemode in Ref. [112] (Figure A.1b), however, their directions are opposite. From the decomposition Eq. (A.71), the edgemodes should contribute a large CW flux in the active system, but somewhat surprisingly, the net flux is CCW. To better analyze the contribution from each eigenmode, we look at a simple honeycomb lattice with only one layer (Figure A.2a). This lattice has four bands (Figure A.2b), two bulk bands (blue, red) and two edge bands (green, yellow). The weighted flux of each band is plotted in Figure A.2c. We see that the CW edge band does contribute a large CW flux (green curve

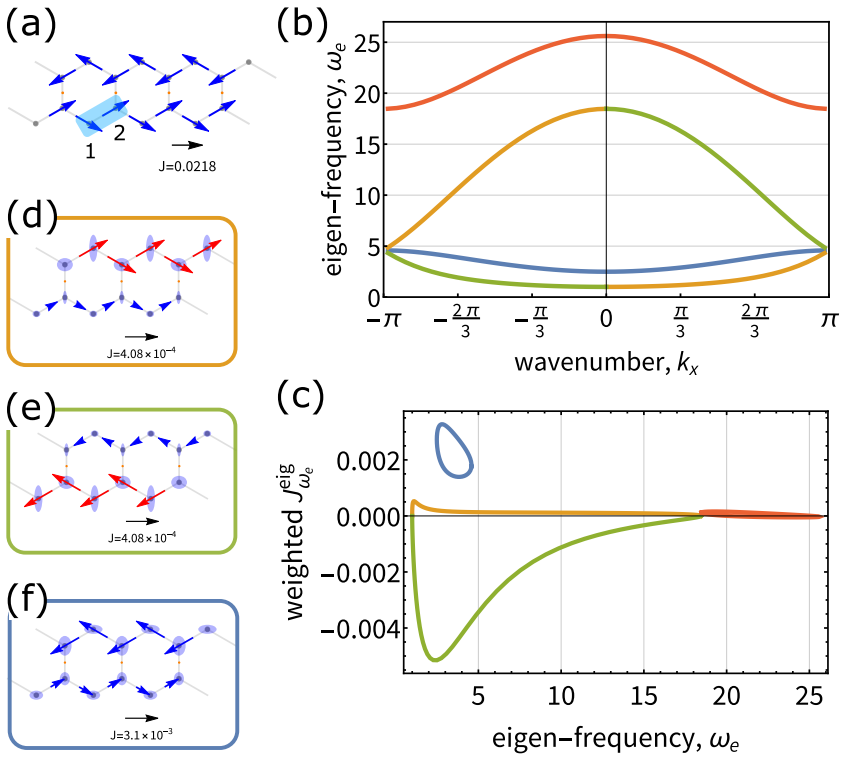

Figure A.2: Using the eigenmode decomposition, we explain how the flux in honeycomb network is CCW, even though its edgemodes contribute to CW fluxes. (a) Network used for calculation, which consists of one row of hexagons (51 unit cells) and has periodic boundary in x direction. Parameters: $k_{g,\tau} = 1, k = 10$, others are 1. (b) Band structure of the network (marked with different colors). The yellow/green band contains CW flux localized on the top/bottom edge (an example mode is shown in (d)/(e)). The blue band contains bulk modes with CCW flux (also see (f)). (c) Weighted flux $J^{eig}_{\omega_e}$ from 1 to 2 (marked in (a)) of the four bands. Total flux in the green band with CW edge modes and the blue band with CCW bulk modes are -0.106 and 0.115, respectively. As a result, the net flux is CCW.

in Figure A.2c), however, due to the "sum rule", the unweighted sum of other bands has to be CCW. In the honeycomb lattice, it happens that many of this CCW fluxes are contained in the lower bulk band (blue curve in Figure A.2c and example mode in Figure A.2f). When the flux gets weighted, the CCW flux from lower bulk band outweighs CW flux from the edgemodes, the other two bands (yellow and red curve in Figure A.2c) also contribute to CCW flux, although relatively small. As a result, the net flux is CCW, which is opposite to the flux of the edgemode.

A.5.2 Derivation of the connection

To derive the eigenmode decomposition Eq. (A.71), we first look at the reference isolated system, write down its eigenmodes and time-averaged energy flux Eq. (A.79). Then we turn to the active system and decompose the flux using the eigenmodes to get Eq. (A.83). Finally we show that the flux from these two sides are actually related in Eq. (A.86). Lastly we also derive the "sum rule" Eq. (A.88).

Energy flux in the reference isolated system

The reference isolated system has first-order gyroscopic dynamics as in Ref. [112]. In the setup with Lorentz force, the dynamical equation can be obtained by setting the mass to zero, and replacing the force matrix K by $K^\tau \equiv K + (\frac{\gamma}{\tau} + \frac{m}{\tau^2})I$

$$\dot{z} = \frac{1}{B} A K^\tau z. \tag{A.73}$$

Following Ref. [112], we convert to complex representation with $z^c \equiv \begin{pmatrix} x+iy & x-iy \end{pmatrix}^T$

$$i\dot{z}^c = \Omega z^c, \quad K^\tau = iBAO^{-1}\Omega O \tag{A.74}$$

where O, O^{-1} are the transformations between z and z^c $z^c = Oz, z = O^{-1}z^c$.

Writing the eigenvalue problem as

$$\Omega u_{\omega_e} = \omega_e u_{\omega_e}, \tag{A.75}$$

the eigenmode with eigen-frequency ω_e reads

$$z^c_{\omega_e}(t) = (u_{\omega_e} e^{-i\omega_e t} + u_{-\omega_e} e^{i\omega_e t}) z_0, \tag{A.76}$$

where z_0 is the amplitude, and it will be specified shortly. The eigenmode needs a combination of ω_e and $-\omega_e$ to ensure that the motion of x and y is real-valued. Mathematically, this combination is possible because of a symmetry in this eigenvalue problem, when there is ω_e, there is also solution $-\omega_e$ with $u_{-\omega_e} = \begin{pmatrix} 0 & I \\ I & 0 \end{pmatrix} u^*_{\omega_e}$.

A related property we need later is that, the left eigenvector v_{ω_e} can be expressed as $v_{\omega_e} = c_{\omega_e} \begin{pmatrix} -I & 0 \\ 0 & I \end{pmatrix} u_{\omega_e}$, where c_{ω_e} is a real prefactor to ensure normalization $v^T_{\omega_e} u_{\omega_e} = 1$. If there are degenerate eigenvectors (like $v^1_{\omega_e}, v^2_{\omega_e}, \dots$), we choose an orthonormal basis set, i.e. $v^{i,T}_{\omega_e} u^j_{\omega_e} = 0$ for $i \neq j$. With the introduction of c_{ω_e}, we now set the amplitude z_0 to $z_0^2 = -2c_{\omega_e} T_a / \omega_e B$, such that the energy of the eigenmode is T_a.

The instantaneous energy flux J_{ω_e} of mode $z^c_{\omega_e}$ writes

$$\begin{aligned} J_{\omega_e} &= (O^{-1} v^c_{\omega_e})^T A^J O^{-1} z^c_{\omega_e} \\ &= \operatorname{tr} O^{-1,T} A^J O^{-1} z^c_{\omega_e} v^{cT}_{\omega_e}, \end{aligned} \tag{A.77}$$

where A^J has been defined in Eq. (A.24). The factor $z^c_{\omega_e} v^{cT}_{\omega_e}$ can be computed using Eq. (A.76). When averaging over periods of oscillation, terms containing $e^{\pm 2i\omega_e t}$ vanish, and we get

$$\overline{z^c_{\omega_e} v^{cT}_{\omega_e}} = i\omega_e (u_{\omega_e} u^T_{-\omega_e} - u_{-\omega_e} u^T_{\omega_e}) z_0^2. \tag{A.78}$$

Plugging in $z_0^2 = -2c_{\omega_e}T_a/\omega_e B$, the time-averaged flux of the eigenmode $J_{\omega_e}^{\text{eig}}$ reads

$$J_{\omega_e}^{\text{eig}} = -\frac{2T_a k}{B} i c_{\omega_e} \operatorname{tr} O^{-1,T} A^J O^{-1} (u_{\omega_e} u_{-\omega_e}^T - u_{-\omega_e} u_{\omega_e}^T). \tag{A.79}$$

Energy flux of the active system

Now we turn to the active system, and the starting point is Eq. (2.10). We need to decompose $G^\tau \equiv G^+(-i/\tau)$ into modes as below. We used u_{ω_e} and v_{ω_e} to denote the right and left eigenvector for matrix Ω at eigen-frequency ω_e, respectively.

$$G^\tau = \frac{i}{B} O^{-1} (\Omega - \frac{i}{\tau} I)^{-1} O A, \tag{A.80}$$

$$\begin{aligned}(\Omega - \frac{i}{\tau} I)^{-1} = &\sum_{\omega_e > 0} \frac{i\tau}{1 + \omega_e^2 \tau^2} (u_{\omega_e} v_{\omega_e}^T + u_{-\omega_e} v_{-\omega_e}^T) \\ &+ \sum_{\omega_e > 0} \frac{\omega_e \tau^2}{1 + \omega_e^2 \tau^2} (u_{\omega_e} v_{\omega_e}^T - u_{-\omega_e} v_{-\omega_e}^T).\end{aligned} \tag{A.81}$$

When plugging G^τ into Eq. (2.10), the contribution from the second term in $(\Omega - \frac{i}{\tau} I)^{-1}$ vanishes, $\operatorname{tr} O A A^{as} O^{-1} (u_{\omega_e} v_{\omega_e}^T - u_{-\omega_e} v_{-\omega_e}^T) = 0$. We arrive at a decomposition of flux in active system into eigenmodes in a reference isolated system,

$$\langle J \rangle = \sum_{\omega_e} \langle J \rangle_{\omega_e}, \tag{A.82}$$

$$\langle J \rangle_{\omega_e} \equiv \frac{T_a k / 2B}{1 + \omega_e^2 \tau^2} \operatorname{tr} O A A^{as} O^{-1} (u_{\omega_e} v_{\omega_e}^T + u_{-\omega_e} v_{-\omega_e}^T). \tag{A.83}$$

Connection between isolated system and active system

Now we need to find the connection between these two fluxes $\langle J \rangle_{\omega_e}$ Eq. (A.83) and $J_{\omega_e}^{\text{eig}}$ Eq. (A.79). We will write $J_{\omega_e}^{\text{eig}}$ in a form that looks similar to $\langle J \rangle_{\omega_e}$. Converting A^J to A^{as} using $A^{as} = -(A^J - A^{J^T})$ (Eq. (A.30)), and u_{ω_e} to v_{ω_e} using $v_{\omega_e} = c_{\omega_e} \begin{pmatrix} -I & 0 \\ 0 & I \end{pmatrix} u_{\omega_e}$, we

get

$$J^{\text{eig}}_{\omega_e} = -\frac{iT_a k}{B} \operatorname{tr} AO^{-1,T} A^{as} O^{-1} (u_{\omega_e} v^T_{\omega_e} + u_{-\omega_e} v^T_{-\omega_e}). \tag{A.84}$$

From direct calculation, $AO^{-1,T} = \frac{i}{2} OA$, and $J^{\text{eig}}_{\omega_e}$ becomes the same as $\langle J \rangle_{\omega_e}$ apart from a factor

$$J^{\text{eig}}_{\omega_e} = \frac{T_a k}{2B} \operatorname{tr} OAA^{as} O^{-1} (u_{\omega_e} v^T_{\omega_e} + u_{-\omega_e} v^T_{-\omega_e}). \tag{A.85}$$

Comparing Eq. (A.85) with (A.83), we arrive at the connection between flux from the active system and from the reference isolated system

$$\langle J \rangle_{\omega_e} = \frac{1}{1 + {\omega_e}^2 \tau^2} J^{\text{eig}}_{\omega_e}. \tag{A.86}$$

Additionally, the unweighted sum reads

$$\sum_{\omega_e} J^{\text{eig}}_{\omega_e} = \frac{T_a k}{2B} \operatorname{tr}\Big[OAA^{as} O^{-1} U V^T \Big], \tag{A.87}$$

where U is the collection of all right eigenvectors $U = \begin{pmatrix} u_{\omega_e,1} & u_{\omega_e,2} & \cdots \end{pmatrix}$, and likewise for V. Since $UV^T = I$ from orthonormality, the unweighted sum vanishes

$$\sum_{\omega_e} J^{\text{eig}}_{\omega_e} = \frac{T_a k}{2B} \operatorname{tr} AA^{as} = 0. \tag{A.88}$$

A.6 Formulation of the diagrammatic approach to calculating the energy flux

To derive the diagrammatic expansion Eq. (2.11) and the path rules, we start from Eq. (A.40), expand around a noninteracting reference system with $k = 0$ to get Eq. (A.95), discuss the convergence radius, then insert resolution of identity to make each term representable by a path as in Eq. (A.100), and arrive at the diagrammatic expansion formula in (A.101). We also provide a convenient way to calculate S_{-l} and a heuristic interpretation of S_l.

A.6.1 Derivation of diagrammatic expansion

Similar to the last section, the central object is G^τ. In the noninteracting case ($k = 0$), G^τ is analytically solvable. We denote $G^\tau\big|_{k=0} = G_0^\tau$. The inverse $(G_0^\tau)^{-1}$ has a block diagonal form,

$$(G_0^\tau)^{-1} = k_{g,\tau} I + \frac{B}{\tau} A \tag{A.89}$$

$$= \sum_i |i\rangle\langle i| \otimes (k_{g,\tau} I + \frac{B}{\tau} A_1). \tag{A.90}$$

where $k_{g,\tau} \equiv k_g + \frac{\gamma}{\tau} + \frac{m}{\tau^2}$. Then G_0^τ is also block diagonal, with each block the inverse of the blocks above,

$$G_0^\tau = \sum_i |i\rangle\langle i| \otimes \frac{1}{(k_{g,\tau})^2 + (B/\tau)^2} (k_{g,\tau} I - \frac{B}{\tau} A_1) \tag{A.91}$$

$$= \sum_i |i\rangle\langle i| \otimes \frac{1}{k_0} R_\alpha, \tag{A.92}$$

where $k_0 \equiv \sqrt{(k_{g,\tau})^2 + (B/\tau)^2}$, and R_α is the rotation matrix with angle $\alpha \equiv \arcsin \frac{B/\tau}{k_0}$, $R_\alpha = \begin{pmatrix} \cos\alpha & -\sin\alpha \\ \sin\alpha & \cos\alpha \end{pmatrix}$.

We now turn on k. We denote the inter-particle part of the force matrix K as kK_s, where the factor k is extracted so that the matrix K_s is dimensionless. The blocks of K_s read

$$\langle i|K_s|i\rangle = \sum_{i' \neq i} e_{ii'} e_{ii'}^T, \quad \langle i|K_s|j\rangle = e_{ij} e_{ji}^T. \tag{A.93}$$

Then G^τ reads

$$G^\tau = \frac{1}{(G_0^\tau)^{-1} + kK_s} = \frac{1}{k_0} [(k_0 G_0^\tau)^{-1} + \frac{k}{k_0} K_s]^{-1} \tag{A.94}$$

In small k/k_0 regime, this matrix inversion can be expanded as

$$\begin{aligned} G^\tau =& \frac{1}{k_0}[(k_0 G_0^\tau) + \frac{k}{k_0}(k_0 G_0^\tau)(-K_s)(k_0 G_0^\tau) \\ &+ (\frac{k}{k_0})^2 (k_0 G_0^\tau)(-K_s)(k_0 G_0^\tau)(-K_s)(k_0 G_0^\tau) + \dots] \\ =& \frac{1}{k_0}(k_0 G_0^\tau) \sum_{n=0}^{\infty} [\frac{k}{k_0}(-K_s)(k_0 G_0^\tau)]^n. \end{aligned} \tag{A.95}$$

To find the convergence radius, we can write the eigen-decomposition of the matrix $(-K_s)(k_0 G_0^\tau)$ as $(-K_s)(k_0 G_0^\tau) = W \Lambda W^{-1}$, where Λ is the diagonal matrix that contains all eigenvalues λ_i's, then the flux becomes

$$\begin{aligned} \langle J \rangle \propto \operatorname{tr} G^\tau A^{as} &\propto \sum_{n=0}^{\infty} \operatorname{tr}(k_0 G_0^\tau)[\frac{k}{k_0} W \Lambda W^{-1}]^n A^{as} \\ &= \sum_i [W^{-1} A^{as} (k_0 G_0^\tau) W]_{ii} \sum_n (\frac{k}{k_0}\lambda_i)^n. \end{aligned} \tag{A.96}$$

For terms in the series to be convergent, k/k_0 should satisfy

$$\frac{k}{k_0} < \frac{1}{\max_i |\lambda_i|}. \tag{A.97}$$

Before inserting resolution of identity to make paths, we note that the matrix A^{as} and K_s have common blocks, $A^{as} = -|i\rangle\langle j| \otimes e_{ij} e_{ji}^T + |j\rangle\langle i| \otimes e_{ji} e_{ij}^T$ and $\langle i|K_s|j\rangle = e_{ij} e_{ji}^T$, so that A^{as} can merge with terms in the expansion of G^τ.

$$\begin{aligned} \frac{\langle J \rangle}{T_a/\tau} &= -\frac{k}{2}(\operatorname{tr} G^\tau A^{as}) \\ &= -\frac{k}{2}(\operatorname{tr} \langle i|G^\tau|j\rangle\, e_{ji} e_{ij}^T - \operatorname{tr} \langle j|G^\tau|i\rangle\, e_{ij} e_{ji}^T) \\ &= \frac{k}{2}(\operatorname{tr} \langle i|G^\tau|j\rangle \langle j|-K_s|i\rangle - \operatorname{tr} \langle j|G^\tau|i\rangle \langle i|-K_s|j\rangle). \end{aligned} \tag{A.98}$$

Now we use the expansion Eq. (A.95), and insert its $(n-1)$'th-order term to the first component in Eq. (A.98), which gives $k \operatorname{tr} \langle i|\frac{1}{k_0}(k_0 G_0^\tau)[\frac{k}{k_0}(-K_s)(k_0 G_0^\tau)]^{n-1}|j\rangle \langle j|-K_s|i\rangle$. If

$n-1=0$, this term vanishes, so we only need to consider $n-1\geq 1$ case. Insert $n-1$ resolution of identity $I=\sum_{l_a=1}^{N}|l_a\rangle\langle l_a|$, and plug in $k_0G_0^\tau$ (Eq. (A.91)), we get

$$\begin{aligned}
&\frac{k}{k_0}\,\mathrm{tr}\,\langle i|(k_0G_0^\tau)[\frac{k}{k_0}(-K_s)(k_0G_0^\tau)]^{n-1}|j\rangle\ \langle j|-K_s|i\rangle\\
=&(\frac{k}{k_0})^n\sum_{l_1,l_2,\ldots,l_{n-1}}\mathrm{tr}\,\langle i|\,(k_0G_0^\tau)\,|l_{n-1}\rangle\,\langle l_{n-1}|\,(-K_s)(k_0G_0^\tau)\cdots|l_1\rangle\,\langle l_1|\,(-K_s)(k_0G_0^\tau)\,|j\rangle\ \langle j|-K_s|i\rangle\\
=&(\frac{k}{k_0})^n\sum_{l_1,l_2,\ldots,l_{n-2}}\mathrm{tr}\,R_\alpha(-K_s)_{il_{n-2}}R_\alpha\cdots(-K_s)_{l_1j}R_\alpha(-K_s)_{ji},
\end{aligned}\tag{A.99}$$

where $(-K_s)_{l_bl_a}\equiv\langle l_b|-K_s|l_a\rangle$. We will denote path $l=i\to j\to l_1\to l_2\to\cdots\to l_{n-2}\to i$, and its corresponding term in the above summation as S_l

$$S_l=(\frac{k}{k_0})^n\,\mathrm{tr}\,R_\alpha(-K_s)_{il_{n-2}}R_\alpha\cdots(-K_s)_{l_1j}R_\alpha(-K_s)_{ji}.\tag{A.100}$$

The second term of the flux in Eq. (A.98) can be treated similarly, and it results in S_{-l}, where $-l$ means path l in its reverse order. Combining Eq. (A.100) and (A.98), we get the diagrammatic expansion of the flux

$$\frac{\langle J\rangle}{T_a/\tau}=\sum_l J_l^{\mathrm{path}}=\sum_l\frac{1}{2}(S_l-S_{-l}).\tag{A.101}$$

A.6.2 Path rules and discussions

The path rules can be extracted from the expression of S_l and J^{path}. From the element $(-K)_{l_bl_a}$ in S_l, we see that either l_a,l_b are bonded, or $l_a=l_b$, otherwise $(-K)_{l_bl_a}=0$. So the path has to be a closed walk along the edges of the network. From J_l^{path} for flux from i to j, we see that if the path contains equal numbers of $i\to j$ and $j\to i$, the net contribution is zero. Because, either $-l=l$, so $J_l^{\mathrm{path}}\propto S_l-S_{-l}=0$, or $-l=l'$ is another path in the summation, and $J_l^{\mathrm{path}}+J_{l'}^{\mathrm{path}}=0$.

To calculate S_{-l}, there is a convenient way given that S_l is known. Based on the transformation below, S_{-l} can be obtained by taking the result of S_l, then replacing α by $-\alpha$.

$$\begin{aligned}\frac{S_{-l}}{(\frac{k}{k_0})^n} &= \mathrm{tr}\Big(R_\alpha(-K_s)_{ij}R_\alpha(-K_s)_{jl_1}\cdots R_\alpha(-K_s)_{l_{n-2}i}\Big)^T \\ &= \mathrm{tr}\, R_{-\alpha}(-K_s)_{il_{n-2}}R_{-\alpha}\cdots(-K_s)_{l_1j}R_{-\alpha}(-K_s)_{ji}.\end{aligned} \tag{A.102}$$

To interpret S_l in a more heuristic way, we insert $I = e_{ij}e_{ij}^T + e_{ij,\perp}e_{ij,\perp}^T$ to the trace in Eq. (A.100), where $e_{ij,\perp}$ denotes the unit direction perpendicular to e_{ij}. Because $(-K_s)_{ji}e_{ij,\perp} = 0$, the trace reduces to a matrix product

$$\frac{S_l}{(\frac{k}{k_0})^n} = e_{ij}^T R_\alpha(-K_s)_{il_{n-2}}R_\alpha\cdots(-K_s)_{l_1j}R_\alpha(-K_s)_{ji}e_{ij}. \tag{A.103}$$

This expression means the following operations: starting from a unit displacement of i along e_{ij}, j would be displaced according to the force $(-K_s)_{ji}e_{ij}$, after which j is rotated by angle α; then start from j and perform similar operations for $(-K_s)_{l_1j}$ and R_α; finally, the transmission goes back to i; we project the displacement onto e_{ij}, and this value is S_l (apart from the pre-factor $(k/k_0)^n$).

A.6.3 Flux of polygon diagrams

Here we write down the flux formula for a polygon path without loops. It is easier to work in local coordinates, where each node has its own coordinate system. Note that now the force F_{ij} in the flux definition Eq. (2.4) does not necessarily equal to $-F_{ji}$, because these two vectors are expressed under different coordinates or bases. However, it can be proved that the expression for energy flux is still given by Eq. (2.10), and diagrammatic technique yield the same result Eq. (2.11).

For each node i in the path, we establish a local coordinate such that the angle from i

to $i-1$ be π, and the angle from i to $i+1$ be θ_i. Then the matrix $(-K_s)_{i+1,i}$ reads

$$(-K_s)_{i+1,i} = -e_{i+1,i}e_{i,i+1}^T = \begin{pmatrix} 1 \\ 0 \end{pmatrix} \begin{pmatrix} \cos\theta_i & \sin\theta_i \end{pmatrix}. \tag{A.104}$$

The trace in S_l becomes

$$\begin{aligned} \frac{S_l}{(\frac{k}{k_0})^n} &= \mathrm{tr} \prod_i (-K_s)_{i+1,i} R_\alpha \\ &= \mathrm{tr} \prod_i \begin{pmatrix} 1 \\ 0 \end{pmatrix} \begin{pmatrix} \cos\theta_i & \sin\theta_i \end{pmatrix} R_\alpha \\ &= \prod_i \begin{pmatrix} \cos\theta_i & \sin\theta_i \end{pmatrix} R_\alpha \begin{pmatrix} 1 \\ 0 \end{pmatrix}. \end{aligned} \tag{A.105}$$

So the flux for this path without loops writes

$$J_{\text{polygon}}^{\text{path}} = \frac{1}{2}(\frac{k}{k_0})^n (\prod_i \cos(\theta_i - \alpha) - \prod_i \cos(\theta_i + \alpha)). \tag{A.106}$$

A.6.4 Contribution from higher-order diagrams

In some situations, the contribution of polygon diagrams vanish, and higher-order paths involving loops become dominant. Unlike the polygon paths, paths with loops are affected by side-chains.

One situation is when the polygon path itself vanishes. In Figure A.3a, the flux of lowest-order path, square (Figure A.3b), is zero, so the main contribution comes from the path with length 5 (Figure A.3b). Through the loop in this path, the orientation of the side-chain controls the flux direction in the main square, without changing the geometry of the main cycle (as seen in Figure 2.1b).

Another situation is that two polygon diagrams cancel each other, which happens in

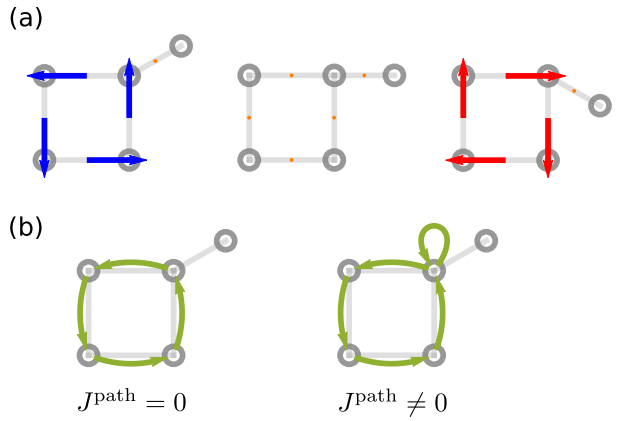

Figure A.3: Higher-order diagrams in a tailed-square network. (a) Direction of flux can be controlled by the orientation of the side-chain. (b) From diagrammatic approach, the flux of the lowest-order diagram (square) vanishes, and the first non-vanishing diagram is affected by the side-chain.

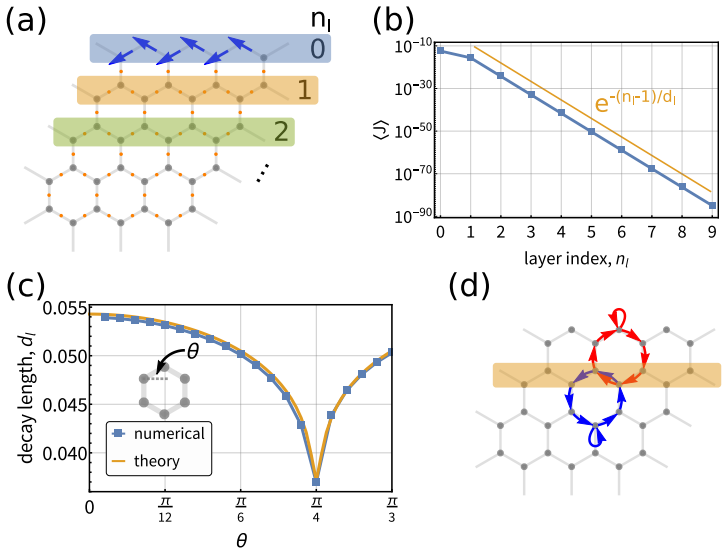

Figure A.4: Decay of fluxes away from the boundary of honeycomb networks, and explanation using the diagrammatic technique. (a) Schematic of a honeycomb network which is periodic in the x direction. Layers from the boundary are indexed as n_l. (b) Semi-log plot of flux $\langle J \rangle$ at layer n_l. The flux starting from layer $n_l = 1$ shows exponential decay, with decay length d_l. Parameters used for numerical calculations are $\theta = \pi/6, k/k_0 = 0.01, \alpha = \pi/4$. (c) Decay length d_l changes with the network angle θ non-monotonically, and the curve has a cusp at $\theta = \alpha = \pi/4$. At small k/k_0, perturbation theory results agree with numerical calculations. (d) The first non-vanishing diagram pair for $n_l = 1$ has length 7. The two diagrams do not cancel, because the loop in the bulk and at the boundary have different values.

honeycomb-like networks away from the boundary (Figure A.4a). With careful calculations, the fluxes for $n_l \geq 1$ are not exactly zero, they rather appear as an exponential decay (Figure A.4b). By changing the geometric angle θ, the decay length varies non-monotonically, and has a cusp at $\theta = \alpha$ (Figure A.4c). This decay and its relationship with θ can be explained by considering the diagrams. While the hexagon path constitutes the lowest-order diagram at the boundary, it vanishes for $n_l \geq 1$ due to cancellations. The first non-vanishing pair of diagrams for $n_l = 1$ is shown in Figure A.4d, in which the loop exploits the asymmetry between the bulk side (with a vertical bond at the blue loop) and the boundary side (with no vertical bonds at the red loop). For every increment of one layer, the length of paths increases by 4. So the flux at layer n_l is on the order of k^{4n_l+3}, which exhibits an exponential decay $e^{-(n_l-1)/d_l}$. Through the calculation of these paths, we get the decay length $d_l = -1/\log[4(k/k_0)^4(\sin(\theta+\alpha)\sin(\theta-\alpha))^2]$. From this result, we see that the cusp at $\theta = \alpha$ in Figure A.4c is due to the term $\sin(\theta - \alpha)$. In fact, at the special point $\theta = \alpha$, paths like Figure A.4d vanish, and we need to consider even higher-order paths.

A.6.5 Exact flux for 1D networks

We show below that the flux of the $1D$ network is exactly zero. For simplicity, we align all sites on the x-axis.

We first consider cases where only nearest neighbor connections are allowed. The $1D$ chain effectively has $C2$-symmetry (bond lengths are irrelevant for the dynamics), so the flux should also obey $C2$-symmetry, which means that the flux can only be zero.

Now we consider more general cases, where bondings between non-neighboring sites are allowed. In such cases, the $1D$ system does not necessarily obey $C2$-symmetry, and the symmetry argument above cannot be applied. However, we can use the diagrammatic approach formulated in Eq. (2.11),(2.12).

For an arbitrary diagram, we look at terms in the expression $S_{\pm l}$,

$$(-K_s)_{l_a l_a} = -\sum_{l_b \neq l_a} \begin{pmatrix} \lambda_{l_a l_b} \\ 0 \end{pmatrix} \begin{pmatrix} \lambda_{l_a l_b} & 0 \end{pmatrix}, \tag{A.107}$$

$$(-K_s)_{l_a l_b,(l_a \neq l_b)} = -\begin{pmatrix} \lambda_{l_a l_b} \\ 0 \end{pmatrix} \begin{pmatrix} \lambda_{l_b l_a} & 0 \end{pmatrix}, \tag{A.108}$$

where $\lambda_{l_a l_b} \equiv \cos\theta_{l_a \to l_b}$ equals 1 if the bond from l_a to l_b lies in $+x$ direction, and equals -1 if the bond lies in $-x$ direction.

We plug $(-K_s)_{l_a l_b}$ into the expression for S_l and get

$$\begin{aligned} S_l = (\frac{-k}{k_0})^n [& \begin{pmatrix} \lambda_{ij} & 0 \end{pmatrix} R_\alpha \begin{pmatrix} \lambda_{i l_n} \\ 0 \end{pmatrix} \begin{pmatrix} \lambda_{l_n i} & 0 \end{pmatrix} \\ & \cdots R_\alpha \begin{pmatrix} \lambda_{l_3 j} \\ 0 \end{pmatrix} \begin{pmatrix} \lambda_{j l_3} & 0 \end{pmatrix} R_\alpha \begin{pmatrix} \lambda_{ji} \\ 0 \end{pmatrix}]. \end{aligned} \tag{A.109}$$

Terms from $(-K_s)_{l_a l_a}$ can be similarly considered.

We see that S_l is a product of terms like $\begin{pmatrix} \lambda_{l_a l_b} & 0 \end{pmatrix} R_\alpha \begin{pmatrix} \lambda_{l_c l_d} \\ 0 \end{pmatrix} = \lambda_{l_a l_b} \lambda_{l_c l_d} \cos\alpha$, which is a even function of α, thus $S_{-l} = S_l(-\alpha) = S_l(\alpha)$. The flux for path l vanish, $J_l^{\text{path}} \propto \sum_l (S_l - S_{-l}) = 0$.

This equality holds for any diagram l, so the exact flux as a sum over all the diagrams vanish. The result is exact beyond small-k regime due to analytic continuation. The brief message extracted from the derivation is that, the effect of B-field has to be projected onto and transmitted through the bonds, but if all bonds are $1D$ colinear, the projection does not distinguish B from $-B$, thus the effect of B-field is nullified.

A.7 Generalization of the diagrammatic approach to a broader range of systems

The system we started with is a class of $2D$ linearized spring-mass networks, where each particle also experiences a Lorentz force, a friction and a OU colored noise. Here we show that the diagrammatic approach originally developed for this class of system can be generalized in its embedding space and in the spectrum of its noise.

A.7.1 Generalization of 2D planar space

The $2D$ space can be generalized to $2D$ curved surface or $3D$ space.

For $2D$ curved surface, we assume linearized dynamics where each site moves on its local tangent plane, and B-field aligns with the normal at each site. The same diagrammatic expansion as formulated in Eq. (2.11)-(2.14) can be readily applied. The reason is that we adopted a local coordinate system (Appendix A.6.3) which holds both for planar surface and for curved surface. Curvature can affect the relation between outer angles θ_i and the number of sides n in a polygon path. For instance, consider a polygon with all $\theta_i = \pi/2$, then Eq. (2.14) dictates $J^{\text{path}}_{\text{polygon}} \propto \sin^n \alpha - \sin^n(-\alpha)$. On a planar surface, such polygon is a rectangle ($n = 4$), $J^{\text{path}}_{\text{polygon}} = 0$, whereas for a curved surface, such polygon can be a spherical triangle ($n = 3$), $J^{\text{path}}_{\text{polygon}} \propto \sin^3 \alpha \neq 0$.

For $3D$ space, we assume that B-field remains the same as in the $2D$ planar case. The same diagrammatic approach applies, but the expressions get modified by the additional spatial dimension. We use local spherical coordinate, and denote the angle with z-axis as ϕ. The noninteracting part of the response matrix, Eq. (A.92), is modified to

$$(G_0^\tau)_{3D} = \sum_i |i\rangle\langle i| \otimes \frac{1}{k_0} \begin{pmatrix} \cos\alpha & -\sin\alpha & 0 \\ \sin\alpha & \cos\alpha & 0 \\ 0 & 0 & \frac{1}{\cos\alpha} \end{pmatrix}. \tag{A.110}$$

For a polygon path, the bond vectors read

$$(e_{i+1,i})_{3D} = \begin{pmatrix} -1 & 0 & 0 \end{pmatrix}^T, \tag{A.111}$$

$$(e_{i,i+1})_{3D} = \begin{pmatrix} \sin\phi_i \cos\theta_i & \sin\phi_i \sin\theta_i & \cos\phi_i \end{pmatrix}^T. \tag{A.112}$$

Plugging these modified expressions into S_l Eq. (2.12), we get the flux for $3D$

$$\begin{aligned} \frac{(J^{\text{path}}_{\text{polygon}})_{3D}}{T_a/\tau} = \frac{1}{2}(\frac{k}{k_0})^n [\prod_i \cos(\theta_i - \alpha)\sin\phi_i \\ - \prod_i \cos(\theta_i + \alpha)\sin\phi_i], \end{aligned} \tag{A.113}$$

which effectively calculates a projection onto the xy-plane.

A.7.2 Generalization of OU color noise

The OU colored noise can be generalize to any noise with spectrum $\left\langle \tilde{\eta}(\omega)\tilde{\eta}(\omega')^T \right\rangle = 2\gamma T_a h(\omega) I \delta_{\omega+\omega',0}/t$. The procedure in deriving the diagrammatic expansion in Appendix A.6.1 still applies, except now the noninteracting part of $G^+(\omega = -i/\tau)$ is replaced by $G^+(\omega)$ at the general ω. As a result, the path rules remain unchanged, but the mathematical expression for the diagrams are modified.

We first define an auxiliary function $J^{\text{aux}}(\omega)$,

$$J^{\text{aux}}(\omega) = -k \,\text{tr}\, G^+(\omega) A^{as}. \tag{A.114}$$

Following Appendix A.6.1, we apply diagrammatic expansion to $J^{\text{aux}}(\omega)$, and get

$$J^{\text{aux}}(\omega) = \sum_l J_l^{\text{aux,path}}(\omega) = \sum_l (S_{\omega,l} - S_{\omega,-l}), \tag{A.115}$$

$$\begin{aligned} S_{\omega,l} = (\frac{k}{k_{0,\omega}})^n \Big\{ & \text{tr}\, R_{\alpha_\omega}(-K_s)_{il_{n-2}} R_{\alpha_\omega} \\ & \cdots (-K_s)_{l_1 j} R_{\alpha_\omega}(-K_s)_{ji} \Big\}, \end{aligned} \tag{A.116}$$

where the symbols are defined as

$$k_{0,\omega} = \sqrt{(k_g + i\omega\gamma - m\omega^2)^2 - (\omega B)^2}, \tag{A.117}$$

$$R_{\alpha_\omega} = \begin{pmatrix} \cos\alpha_\omega & -\sin\alpha_\omega \\ \sin\alpha_\omega & \cos\alpha_\omega \end{pmatrix}, \tag{A.118}$$

$$\cos\alpha_\omega = \frac{1}{k_{0,\omega}}(k_g + i\omega\gamma - m\omega^2), \tag{A.119}$$

$$\sin\alpha_\omega = \frac{1}{k_{0,\omega}} i\omega B. \tag{A.120}$$

Note that the condensed parameters $k_{0,\omega}, \alpha_\omega$ are complex, as opposed to the real k_0, α for the case with OU noise (Eq. (2.13)).

For polygon paths with outer angles θ_i's, $S_{\omega,\pm l}$ simplifies to

$$S_{\omega,\pm l} = (\frac{k}{k_{0,\omega}})^n \prod_i \cos(\theta_i \mp \alpha_\omega), \tag{A.121}$$

which is formally similar to S_l for the OU noise case (Eq. (2.14)).

Based on the spectral expression Eq. (2.7), the flux $\langle J \rangle$ can be calculated in two ways. One way is to write $J^{FT}(\omega)$ in terms of $J^{\text{aux}}(\omega)$,

$$J^{FT}(\omega) = \frac{T_a}{4\pi}(J^{\text{aux}}(\omega) + J^{\text{aux}}(-\omega)), \tag{A.122}$$

then express $\langle J \rangle$ as an integral $\langle J \rangle = \int \mathrm{d}\omega\, h(\omega) J^{FT}(\omega)$.

Another way is to first integrate Eq. (2.7) using the residue theorem, then express $\langle J \rangle$ in terms of $J^{\text{aux}}(\omega)$ evaluated at the poles,

$$\langle J \rangle = -T_a i \sum_i \text{Res}_{\omega=\omega_i}[h(\omega) J^{\text{aux}}(\omega)]. \tag{A.123}$$

A.8 Simulation of active gyroscopic network coupled with a passive segment

A simulation is shown in the Supplemental Video, which presents both the motion of particles and the energy flux through the color-labelled bonds. The energy fluxes are in general random. During the period when J is large, J appears as successive peaks, indicating a large energy flow from left to right. The interval between the peaks matches the sound speed of the elastic chain ($\sqrt{k/m}$). Although the averaged direction of energy flux is from left to right, the instantaneous flux can also transport from right to left, shown as negative peaks.

The simulation is performed using LAMMPS [164] with Moltemplate toolkit [165] and custom code. We used a Trotter splitting method [175, 176] to simulate the underdamped Langevin dynamics. The integrator combines the integrator for colored noise [118] and that for Lorentz force [177]. We did not simulate the commonly-used overdamped Langevin dynamics, because some intricacy arises when the system also experiences a Lorentz force [178]. Below, we first define each step in the integrator, then present the combined result.

The velocity-Verlet step U_{vv} is the integrator when both Lorentz force and the colored noise are absent. It is defined as

$$U_{vv}(\Delta t): \quad v \leftarrow v + F(x)\Delta t/(2m) \tag{A.124}$$

$$x \leftarrow x + v\Delta t \tag{A.125}$$

$$v \leftarrow v + F(x)\Delta t/(2m), \tag{A.126}$$

where $F(x)$ is the conservative force, including on-site and inter-particle potentials.

Writing the Lorentz force part as

$$\dot{v} = -\begin{pmatrix} 0 & B/m \\ -B/m & 0 \end{pmatrix} \begin{pmatrix} v_x \\ v_y \end{pmatrix} \equiv -a_p v, \tag{A.127}$$

then its integrator U_L is a rotation of the velocity

$$U_L(\Delta t): \quad v \leftarrow e^{-\Delta t a_p} v. \tag{A.128}$$

Writing the colored noise part as

$$\frac{d}{dt}\begin{pmatrix} v \\ \eta \end{pmatrix} = -A_p \begin{pmatrix} v \\ \eta \end{pmatrix} + B_p \begin{pmatrix} \xi_w \\ \xi_a \end{pmatrix}, \tag{A.129}$$

$$A_p = \begin{pmatrix} \frac{\gamma}{m} & -\frac{1}{m} \\ 0 & \frac{1}{\tau} \end{pmatrix}, \quad B_p = \begin{pmatrix} 0 & 0 \\ 0 & \frac{\sqrt{2\gamma T_a}}{\tau} \end{pmatrix}, \tag{A.130}$$

then its integrator U_{OUP} reads

$$U_{OUP}(\Delta t): \quad \begin{pmatrix} v \\ \eta \end{pmatrix} \leftarrow T(\Delta t) \begin{pmatrix} v \\ \eta \end{pmatrix} + S(\Delta t) \begin{pmatrix} 0 \\ N_a \end{pmatrix}, \tag{A.131}$$

where N_a is the standard Gaussian random variable, and

$$T(\Delta t) = e^{-\Delta t A_p}, \tag{A.132}$$

$$S(\Delta t) S(\Delta t)^T = C_p - T(\Delta t) C_p T(\Delta t)^T. \tag{A.133}$$

C_p is the solution of $A_p C_p + C_p A_p^T = B_p B_p^T$. $S(\Delta t)$ can be solved as an upper-triangle matrix.

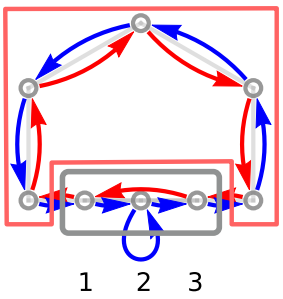

Figure A.5: One example of $\left\langle J_{31}^{s}\right\rangle$ diagram (red) and $\left\langle J_{12}^{s}\right\rangle$ diagram (blue). Passive particles are boxed in gray, and the active ones are boxed in red.

Combining these steps together, the integrator for one time step Δt reads

$$U(\Delta t)=U_{OUP}(\frac{\Delta t}{2})U_{L}(\frac{\Delta t}{2})U_{vv}(\Delta t)U_{L}(\frac{\Delta t}{2})U_{OUP}(\frac{\Delta t}{2}), \tag{A.134}$$

where the order of operations is right-to-left.

A.9 Relationship between swimmer's speed and energy flux

To understand the proportionality between V_s and $\langle J\rangle$, we turn to the diagrammatic technique. Different from previous cases, this path sum can be computed exactly, so the result holds beyond small k regime.

First we rewrite V_s as the following

$$\frac{V_s}{7a/24L^2}=\langle J_{12}^{s}\rangle+\langle J_{23}^{s}\rangle+\langle J_{31}^{s}\rangle\,, \tag{A.135}$$

where we have defined $\left\langle J_{ij}^{s}\right\rangle\equiv\langle(x_i-x_j)(v_i+v_j)\rangle$. $\left\langle J_{ij}^{s}\right\rangle$ is proportional to the energy flux via $\left\langle J_{ij}\right\rangle=k_{ij}\left\langle J_{ij}^{s}\right\rangle/2$, where $k_{12}=k_{23}=k$, and $k_{31}=0$ (because $\langle J_{31}\rangle=0$, there is no energy flux from 3 to 1). We see that both $\left\langle J_{12}^{s}\right\rangle$ and $\left\langle J_{23}^{s}\right\rangle$ are proportional to the flux $\langle J\rangle$ apart from a factor k, so the remaining task is to find the relationship between $\left\langle J_{31}^{s}\right\rangle$ and $\langle J\rangle$ or $\left\langle J_{12}^{s}\right\rangle$.

We use a diagrammatic technique with the modification that the paths should contain

only one $3 \to 1$ segment. This modification is a consequence of the fact that particle 3 and 1 are not bonded. We now illustrate the correspondence between the diagrams for $\left\langle J_{31}^s \right\rangle$ and for $\left\langle J_{12}^s \right\rangle$. For each path l for $\left\langle J_{31}^s \right\rangle$, we can construct n paths for $\left\langle J_{12}^s \right\rangle$ by reversing l then replacing $1 \to 3$ by $1 \to 2(\to 2)^n \to 3$, where $n = 0, 1, \ldots$. An example construction of paths is shown in Figure A.5. For $\left\langle J_{12}^s \right\rangle$, all its paths can be constructed in this way. As a result, there is a 1 to n correspondence between the paths for $\left\langle J_{31}^s \right\rangle$ and for $\left\langle J_{12}^s \right\rangle$, which leads to the relationship

$$\langle J_{12}^s \rangle = \frac{k}{k_0} \sum_{n=0}^{\infty} (-2\frac{k}{k_0})^n (-\langle J_{31}^s \rangle) \tag{A.136}$$

$$= \frac{k/k_0}{1-(-2k/k_0)} (-\langle J_{31}^s \rangle), \tag{A.137}$$

where $k_0 = k_g + m/\tau^2$ ($B, \gamma = 0$ for the passive part), and the factor $-2\frac{k}{k_0}$ comes from the loop $2 \to 2$. Plugging Eq. (A.137) to the expression of V_s Eq. (A.135), we obtain the proportionality

$$\frac{V_s}{7a/24L^2} = -\frac{k_0}{k} \frac{\langle J \rangle}{k/2}, \tag{A.138}$$

which is Eq. (2.16) in the main text. Since we have considered all the diagrams, this result can be analytically continued to arbitrarily large k.

From this diagrammatic technique we also see that, the proportionality constant is independent of the geometry of the active part of the network. This is because the paths through the active part for $\left\langle J_{31}^s \right\rangle$ and for $\left\langle J_{12}^s \right\rangle$ are identical.

APPENDIX B

DERIVATIONS RELATED TO TIME-MODULATED ACTIVE GYROSCOPIC NETWORKS

B.1 Numerical calculation of energy flux from time-dependent covariance matrix

For a general linear stochastic equation with time-independent drift μ and diffusion factor σ,

$$\mathrm{d}X = \mu \mathrm{d}t + \sigma \mathrm{d}W, \tag{B.1}$$

its steady-state covariance matrix $C = \left\langle XX^T \right\rangle$ can be numerically solved from the matrix equation $\mu C + C\mu^T = \sigma\sigma^T$ [117, 118]. The time-dependent covariance $C(t)$ starting from an initial state C_0 reads

$$C(t) = C + e^{\mu t}(C_0 - C)e^{\mu^T t}. \tag{B.2}$$

From $C(t)$ we can extract the energy flux at time t, $-\gamma v_i^T v_i + v_i^T \eta_i$, and subsequently calculate its time integral.

Our numerical procedure to calculate Q_i is as follows. Given a protocol $B(t)$, we discretize it into short segments in time. In each segment the B-field is constant and is evaluated at the starting time of that segment. Consequently, the covariance matrix in each segment can be calculated using Eq. (B.2). The time-dependent $C(t)$ for protocol $B(t)$ can thus be solved by combining results from all segments. We choose a starting C_0 to be the steady state under constant $B(0)$, evolve $C(t)$ for many periods until $C(nT) - C(nT + T)$ is smaller than a target numerical precision, which indicates that the time-periodic steady state is achieved. Then evolve $C(t)$ from this steady state and calculate the pumped energy Q_i. The source of numerical error mainly comes from discretization. Numerical calculations are performed using Mathematica with custom code [169].

B.2 No pumping in the adiabatic limit

The system we consider is the active gyroscopic network with time-modulated parameters, e.g. setting $B = B(t)$. In the adiabatic limit, the time-modulation could endow interested quantities a geometric term [62, 61]. Such term requires a time-modulation of at least two parameters. Here we show that the geometric phase formalism also applies to our system. Since we only modulate one parameter, the B-field, our energy pumping vanishes in the adiabatic limit.

B.2.1 Review of geometric phase and its application to energy flux

The two main points of techniques involved [62, 61] are as follows, which we review in the next two sections.

- The first technique derives the geometric phase of the eigenfunction of a general linear system. For a linear system, $\partial_t f = L(t)f$ with "adiabatic" time-periodic modulation $L(t+T) = L(t)$, after a period T, f can gain a phase factor $f(t+T) = e^{i\phi} f(t)$, which can contain a geometric part.

- The second technique adapts the geometric phase to the context of heat flux. For classical systems, we are usually interested in some quantities, e.g. accumulated heat Q. To apply the above technique, one makes Q to be a phase factor, by looking at the cumulant generating function (CGF) $f = \left\langle e^{isQ} \right\rangle$. If the evolution of CGF is also linear, $\partial_t f = L(t)f$, then f can also gain a phase factor after a period, which means that Q can gain an extra term.

Geometric phase formulation

This section summarizes the derivation of the geometric phase, which can be found in tutorials of the Berry phase or Ref.[62].

Consider a time-modulated linear system,

$$\partial_t f = L(t) f. \tag{B.3}$$

In the adiabatic limit, $f(t)$ always stays in the ground state of instantaneous $L(t)$, apart from a phase factor. After a period, $f(t+T)$ can differ from $f(t)$ by a phase factor,

$$f(t+T) = e^{i\phi} f(t). \tag{B.4}$$

We review the steps to derive this factor $e^{-\phi}$.

The evolution of f can be discretized as

$$f(T) = \lim_{\Delta t \to 0} e^{L_{N-1}\Delta t} e^{L_{N-2}\Delta t} \cdots e^{L_1 \Delta t} e^{L_0 \Delta t} f(0), \tag{B.5}$$

where $\Delta t = T/N, L_i = L(t_i), t_i = i\Delta t$.

We express the above equation in terms of the ground state of $L(t)$. Denote the ground-state eigenvalue problem of the instantaneous operator $L(t)$ as

$$L(t) \left|u(t)\right\rangle = \lambda(t) \left|u(t)\right\rangle, \tag{B.6}$$

with left eigenvector $\langle u(t)|$ and normalization $\langle u(t)|u(t)\rangle = 1$. The operator $e^{L_i \Delta t}$ in the adiabatic limit can be expressed in terms of the ground-state, ignoring all excited states

$$e^{L_i \Delta t} \approx \left|u_i\right\rangle e^{\lambda_i \Delta t} \left\langle u_i\right|. \tag{B.7}$$

Also set the initial state $f(0) = |u(0)\rangle$, then the final state $f(T) = e^{i\phi} |u(0)\rangle$.

Then the phase can be expressed as follows

$$e^{i\phi} = \langle u(0)|\, f(T) \tag{B.8}$$

$$= \lim_{\Delta t\to 0} \langle u_0|u_{N-1}\rangle\, e^{\lambda_{N-1}\Delta t}\, \langle u_{N-1}|\cdots|u_1\rangle\, e^{\lambda_1\Delta t}\, \langle u_1|u_0\rangle\, e^{\lambda_0\Delta t}\, \langle u_0|u_0\rangle \tag{B.9}$$

$$= \lim_{\Delta t\to 0} \prod_{i=0}^{N-1} e^{\lambda_i\Delta t}\, \langle u_{i+1}|u_i\rangle\,, \tag{B.10}$$

where $ketu_N \equiv |u_0\rangle$.

We elevate the term $\langle u_{i+1}|u_i\rangle$ to the exponent, so as to derive an expression for ϕ.

$$\langle u_{i+1}|u_i\rangle = 1 - \langle u_{i+1}|\, \frac{|u_{i+1}\rangle - |u_i\rangle}{\Delta t}\Delta t \tag{B.11}$$

$$\approx 1 - \Delta t\, \langle u_{i+1}|\, \partial_t\, |u_i\rangle \tag{B.12}$$

$$= e^{\ln(1-\Delta t\langle u_{i+1}|\partial_t|u_i\rangle)} \tag{B.13}$$

$$\approx e^{-\Delta t\langle u_{i+1}|\partial_t|u_i\rangle}. \tag{B.14}$$

Back to the phase,

$$e^{i\phi} \approx \lim_{\Delta t\to 0} \prod_{i=0}^{N-1} e^{\lambda_i\Delta t} e^{-\Delta t\langle u_{i+1}|\partial_t|u_i\rangle} \tag{B.15}$$

$$= \lim_{\Delta t\to 0} e^{\sum_{i=0}^{N-1}\Delta t(\lambda_i - \langle u_{i+1}|\partial_t|u_i\rangle)} \tag{B.16}$$

$$i\phi = \oint_T \mathrm{d}t\, \lambda(t) - \oint_T \mathrm{d}t\, \langle u(t)|\, \partial_t\, |u(t)\rangle\,. \tag{B.17}$$

The second term can be shown to be time-independent, or geometric. Write the time-modulation as one through changing some parameters in time $\boldsymbol{R} = \boldsymbol{R}(t)$,

$$\oint \mathrm{d}t\, \langle u(t)|\, \partial_t\, |u(t)\rangle = \oint \mathrm{d}t\, \langle u(\boldsymbol{R})|\, \frac{\mathrm{d}\boldsymbol{R}}{\mathrm{d}t}\cdot\nabla_{\boldsymbol{R}}\, |u(\boldsymbol{R})\rangle \tag{B.18}$$

$$= \oint \mathrm{d}\boldsymbol{R}\cdot \langle u(\boldsymbol{R})|\, \nabla_{\boldsymbol{R}}\, |u(\boldsymbol{R})\rangle\,. \tag{B.19}$$

Finally, the phase reads

$$i\phi = \oint_T \mathrm{d}t\, \lambda(t) - \oint \mathrm{d}\boldsymbol{R} \cdot \langle u(\boldsymbol{R})|\, \nabla_{\boldsymbol{R}}\, |u(\boldsymbol{R})\rangle\,, \tag{B.20}$$

where the first term is dynamics, and the second term is geometric. The second term can be non-zero when the dimension of $\boldsymbol{R}$ is greater than one.

Geometric phase applied to energy flux

This section summarizes how the idea of geometric phase can be applied to calculate physical quantities such as the energy flux [62, 61]. For classical systems, one needs to elevate interested physical quantities to a phase factor, so as to accommodate the geometric phase formalism. As a comparison, for quantum systems, a phase in the wave function itself is already an interesting quantity to study.

Consider a general stochastic dynamics equation (SDE)

$$\dot{X} = \mu + \sigma\xi, \tag{B.21}$$

where X denotes all variables, ξ denotes the noise, μ is the drift and σ is the noise correlation. The corresponding Fokker-Planck equation (FPE) formally reads

$$\partial_t p(X;t) = L_{X;t} p(X;t). \tag{B.22}$$

The quantity of interest, the accumulated heat reads

$$Q(t) = \int_0^t \mathrm{d}t'\, q(t'), \tag{B.23}$$

where $q(t)$ is a function of $X(t), \xi(t)$. We review the procedure to express $Q(T)$ as a phase.

From this setup, one could try to write down the evolution of the CGF $f(s;t) = \left\langle e^{isQ(t)} \right\rangle$,

but it seems that $\partial_t f(s;t)$ cannot be expressed in forms like Lf, probably because $\langle\cdot\rangle$ averages out too much information, such that the remaining information alone is not enough for the evolution. So the trick in Ref.[61] is to look at $f(X,s;t) = \int \mathrm{d}Q\, e^{isQ} p(x,Q;t)$, which now contains all information, so that its evolution can (possibly) be expressed in a closed form.

The extended SDE for X, Q reads

$$\dot{X} = \mu + \sigma\xi, \tag{B.24}$$

$$\dot{Q} = q. \tag{B.25}$$

Its FPE formally reads

$$\partial_t p(X,Q;t) = L_{X,Q;t} p(X,Q;t). \tag{B.26}$$

The CGF for the extended probability is defined as

$$f(X,s;t) = \int_{-\infty}^{\infty} \mathrm{d}Q\, e^{isQ(t)} p(X,Q;t). \tag{B.27}$$

Now we assume that $f(X,s;t)$ obeys a linear evolution, based on which we derive the expression for Q. In the next section, we show that this condition is true for our active gyro system. The linear evolution reads

$$\partial_t f(X,s;t) = L_{X,s;t} f(X,s;t). \tag{B.28}$$

In the rest of this section, we derive $Q(T)$ from the linear evolution of $f(X,s;t)$.

We write the phase as

$$f(X,s;t) = e^{i\phi(s;t)} f(X,s;t=0). \tag{B.29}$$

At $t = 0$, $Q(t = 0) = 0$, so

$$p(X, Q; t = 0) = p(X; t = 0)\delta(Q), \tag{B.30}$$

$$f(X, s; t = 0) = \int \mathrm{d}Q\, e^{isQ(t=0)}\delta(Q)p(X; t = 0) = p(X; t = 0), \tag{B.31}$$

$$f(X, s; t) = e^{i\phi(s;t)}p(X; t = 0). \tag{B.32}$$

The full CGF

$$f(s; t) = \int \mathrm{d}X\, f(X, s; t) = \left\langle e^{isQ(t)} \right\rangle \tag{B.33}$$

$$= \int \mathrm{d}X\, e^{i\phi(s;t)}p(X; t = 0). \tag{B.34}$$

From the CGF, the heat flux can be calculated

$$\langle Q(T)\rangle = \frac{\partial}{\partial is} \left\langle e^{isQ(T)} \right\rangle \Big|_{s\to 0} \tag{B.35}$$

$$= \frac{\partial}{\partial is} \int \mathrm{d}X\, e^{i\phi(s;T)}p(X; 0) \Big|_{s\to 0} \tag{B.36}$$

$$= \int \mathrm{d}X\, p(X; 0)\frac{\partial i\phi(s; T)}{\partial is}e^{i\phi(s;T)} \Big|_{s\to 0}. \tag{B.37}$$

As $s \to 0$,

$$f(X, s \to 0; T) = \int \mathrm{d}Q\, p(X, Q; T) = p(X; T) = p(X; 0), \tag{B.38}$$

since $f(X, s \to 0; T) = e^{i\phi(s\to 0;T)}p(X; 0)$, we conclude that $e^{i\phi(s\to 0;T)} = 1$. Also, since $i\phi(s \to 0; T)$ does not depend on X (see Eq. (B.20) or later Eq. (B.41)), the integral over X can be carried out, $\int \mathrm{d}X\, p(X; t = 0) = 1$. The heat flux

$$\langle Q(T)\rangle = \frac{\partial i\phi(s, T)}{\partial is} \Big|_{s\to 0}. \tag{B.39}$$

Now we further express the heat in terms of the eigenfunction. Write the eigenfunction of $L_{X,s;t}$ and its adjoint as $u(X,s;t)$ and $u^+(X,s;t)$,

$$L_{X,s;t}u(X,s;t) = \lambda(s;t)u(X,s;t), \quad L^+_{X,s;t}u^+(X,s;t) = \lambda(s;t)^* u^+(X,s;t). \tag{B.40}$$

Here the scalar product is defined for complex functions as $(f_1(x), f_2(x)) = \int \mathrm{d}x\, f_1(x)^* f_2(x)$. Applying the expression for phase Eq. (B.20),

$$i\phi(s,T) = \oint_T \mathrm{d}t\, \lambda(s;t) - \oint \mathrm{d}\boldsymbol{R} \cdot \int \mathrm{d}X\, u^{+,*}(X,s;\boldsymbol{R}) \nabla_{\boldsymbol{R}} u(X,s;\boldsymbol{R}). \tag{B.41}$$

Taking these terms together, we express the energy flux as a sum of a dynamic term and a geometric term,

$$\langle Q(T) \rangle = \oint_T \mathrm{d}t\, \frac{\partial}{\partial is} \lambda(s;t)\bigg|_{s\to 0} - \oint \mathrm{d}\boldsymbol{R} \cdot \frac{\partial}{\partial is} \int \mathrm{d}X\, u^{+,*}(X,s;\boldsymbol{R}) \nabla_{\boldsymbol{R}} u(X,s;\boldsymbol{R})\bigg|_{s\to 0}. \tag{B.42}$$

B.2.2 Application to time-modulated active gyro system

To apply the above techniques to our active gyro system, the only task is to show whether the linear evolution of extended CGF Eq. (B.28) holds. In this section, we show that it does hold.

The SDE of our system reads

$$\dot{X} = \mu + \sigma\xi, \tag{B.43}$$

$$\dot{Q} = q, \tag{B.44}$$

where

$$X = \begin{pmatrix} z \\ v \\ \eta \end{pmatrix}, \quad \mu = \begin{pmatrix} v \\ (-Kz - \gamma v - BAv + \eta)/m \\ -\eta/\tau \end{pmatrix}, \quad \sigma = \begin{pmatrix} 0 & & \\ & 0 & \\ & & \sqrt{2\gamma T_a}/\tau \end{pmatrix}, \tag{B.45}$$

$$q = -\gamma v_i^T v_i + v_i^T \eta_i. \tag{B.46}$$

Note that our q does not contain the noise ξ, which simplifies later derivation compared with Ref.[61].

The FPE for X reads

$$\partial_t p(X;t) = L_{X;t} p(X;t), \tag{B.47}$$

where the FP-operator is

$$L_{X;t} f = -\nabla_X^T \mu f + \frac{1}{2} \operatorname{tr}\Big[\nabla_X \nabla_X^T \sigma\sigma^T f\Big]. \tag{B.48}$$

The FPE for $\{X, Q\}$ reads

$$\partial_t p(X,Q;t) = L_{X,Q;t} p(X,Q;t), \tag{B.49}$$

$$L_{X,Q;t} f = -\nabla_X^T \mu f - \partial_Q (qf) + \frac{1}{2} \operatorname{tr}\Big[\nabla_X \nabla_X^T \sigma\sigma^T f\Big] \tag{B.50}$$

$$= L_{X;t} f - \partial_Q (qf). \tag{B.51}$$

The extended CGF is defined the same way as the last section,

$$f(X,s;t) = \int \mathrm{d}Q \, e^{isQ} p(X,Q;t). \tag{B.52}$$

It evolution is calculated as

$$\partial_t f(X,s;t) = \int \mathrm{d}Q\, e^{isQ} \frac{\partial p(X,Q;t)}{\partial t} \tag{B.53}$$

$$= \int \mathrm{d}Q\, e^{isQ} L_{X,Q;t} p(X,Q;t) \tag{B.54}$$

$$= \int \mathrm{d}Q\, e^{isQ} L_{X;t} p(X,Q;t) - \int \mathrm{d}Q\, e^{isQ} \partial_Q (qp(X,Q;t)) \tag{B.55}$$

$$= L_{X;t} f(X,s;t) - (e^{isQ} qp(X,Q;t)\Big|_{Q=-\infty}^{+\infty} - \int \mathrm{d}Q\, qp(X,Q;t) ise^{isQ}) \tag{B.56}$$

$$= L_{X;t} f(X,s;t) + isqf(X,s;t), \tag{B.57}$$

where $e^{isQ} qp(X,Q;t)\big|_{Q=-\infty}^{+\infty}$ because $p(X, Q \to \pm\infty; t) \to 0$. We get the evolution of the extended CGF,

$$\partial_t f(X,s;t) = (L_{X;t} + isq) f(X,s;t). \tag{B.58}$$

We see that the evolution of the extended CGF is indeed linear, so the formalism in the last subsection apply. We conclude that there is a geometric pumping, but for the geometric term to take effect, it requires time-modulation of at least two variables. Since we only modulate one parameter, the B-field, in our time-periodic active gyroscopic system, the adiabatic limit of energy pumping is zero.

B.3 Perturbative expansion in modulated B-field

B.3.1 Correlators that involve the response field

Consider a dynamics that is perturbed by an external force $f(t)$,

$$m\dot{v} = -Kz - \gamma v - BAv + \eta + f. \tag{B.59}$$

The MSR/JDP result can be obtained by simply replacing $-\Delta BAv$ in Eq. (3.9) with f, which reads

$$\langle O \rangle_f = \left\langle O e^{\int \mathrm{d}t i u^T f} \right\rangle . \tag{B.60}$$

The correlators can then be related to the response,

$$\left\langle O i u_{i,s} \right\rangle = \left. \frac{\delta}{\delta f_{i,s}} \langle O \rangle \right|_{f \to 0}, \tag{B.61}$$

$$\left\langle O i u_{i,s} i u_{i',s'} \right\rangle = \left. \frac{\delta}{\delta f_{i,s} \delta f_{i',s'}} \langle O \rangle \right|_{f_s \to 0}, \tag{B.62}$$

where we have expressed the component of the vector f, iu explicitly. From these expressions we see that iu is called a response field because its correlators are equal to responses to an external perturbation.

In the Fourier space, the equation of motion reads

$$\tilde{v} = i\omega G^+ \tilde{\eta} + i\omega G^+ \tilde{f}. \tag{B.63}$$

The response field can be expressed with the help of Parseval's theorem,

$$\langle O \rangle_f = \left\langle O e^{\int \frac{\mathrm{d}\omega}{2\pi} i\tilde{u}(\omega)^T \tilde{f}(-\omega)} \right\rangle, \tag{B.64}$$

$$\left\langle O i \tilde{u}_{i,\omega} \right\rangle = 2\pi \left. \frac{\delta}{\delta \tilde{f}_{i,-\omega}} \langle O \rangle \right|_{\tilde{f} \to 0}. \tag{B.65}$$

$$\tag{B.66}$$

B.3.2 Two-point correlators in unmodulated reference system

The correlator $\left\langle v_t \eta_s^T \right\rangle$ reads

$$\left\langle v_t \eta_s^T \right\rangle = \int \frac{\mathrm{d}\omega}{2\pi} \frac{\mathrm{d}\omega'}{2\pi} e^{i\omega t + i\omega' s} (i\omega) G^+(\omega) \left\langle \tilde{\eta}(\omega) \tilde{\eta}(\omega')^T \right\rangle, \tag{B.67}$$

$$= \int \frac{\mathrm{d}\omega}{2\pi} e^{i\omega(t-s)} 2i\omega\gamma T_a h(\omega) G^+(\omega). \tag{B.68}$$

For the case $t < s$, if η is a white noise $h(\omega) = 1$, then $\left\langle v_t \eta_s^T \right\rangle = 0$ due to causality. If η is OU colored noise, then $\left\langle v_t \eta_s^T \right\rangle \neq 0$ due to correlations between η_s and η_t.

The correlator $\left\langle v_t v_s^T \right\rangle$ reads

$$\left\langle v_t v_s^T \right\rangle = \int \frac{\mathrm{d}\omega}{2\pi} e^{i\omega(t-s)} (i\omega)(-i\omega) 2\gamma T_a h(\omega) G^+(\omega) G^-(\omega)^T \tag{B.69}$$

$$= \int \frac{\mathrm{d}\omega}{2\pi} e^{i\omega(t-s)} i\omega T_a h(\omega) (G^+(\omega) - G^{-T}(\omega)) \tag{B.70}$$

$$= \left\langle v_t v_s^T \right\rangle = \int \frac{\mathrm{d}\omega}{2\pi} i\omega T_a h(\omega) (e^{i\omega(t-s)} G^+(\omega) + e^{i\omega(s-t)} G^{+T}(\omega)) \tag{B.71}$$

$$= \frac{1}{2\gamma} (\left\langle v_t \eta_s^T \right\rangle + \left\langle v_s \eta_t^T \right\rangle^T), \tag{B.72}$$

where to reach the second line we have used $G^{-T} - G^+ = 2i\omega\gamma G^+ G^{-T}$ [119].

The correlator $\left\langle \eta_t \eta_s^T \right\rangle$ reads

$$\left\langle \eta_t \eta_s^T \right\rangle = \int \frac{\mathrm{d}\omega}{2\pi} e^{i\omega(t-s)} 2\gamma T_a h(\omega). \tag{B.73}$$

The correlator $\left\langle v_t i u_s^T \right\rangle$ reads

$$\left\langle v_{i,t} i u_{j,s} \right\rangle = \int \frac{\mathrm{d}\omega}{2\pi} \frac{\mathrm{d}\omega'}{2\pi} e^{i\omega t + i\omega' s} \left\langle \tilde{v}_{i,\omega} i \tilde{u}_{j,\omega'} \right\rangle \tag{B.74}$$

$$= \int \frac{\mathrm{d}\omega}{2\pi} \frac{\mathrm{d}\omega'}{2\pi} e^{i\omega t + i\omega' s} 2\pi \left. \frac{\delta}{\delta \tilde{f}_{j,-\omega'}} \left\langle \tilde{v}_{i,\omega} \right\rangle \right|_{\tilde{f} \to 0} \tag{B.75}$$

$$= \int \frac{\mathrm{d}\omega}{2\pi} \frac{\mathrm{d}\omega'}{2\pi} e^{i\omega t + i\omega' s} i\omega G^+(\omega)_{ij} 2\pi \delta(\omega + \omega') \tag{B.76}$$

$$= \int \frac{\mathrm{d}\omega}{2\pi} e^{i\omega(t-s)} i\omega G^+(\omega)_{ij}. \tag{B.77}$$

If $t < s$, $\left\langle v_t i u_s^T \right\rangle = 0$ due to causality.

The correlator $\left\langle \eta_t i u_s^T \right\rangle$ reads

$$\left\langle \eta_{i,t} i u_{j,s} \right\rangle = \left. \frac{\delta}{\delta f_{j,s}} \left\langle \eta_{i,t} \right\rangle \right|_{f \to 0} = 0 \tag{B.78}$$

The correlator $\left\langle i u_t i u_s^T \right\rangle$ reads (by setting $O = 1$)

$$\left\langle i u_{i,t} i u_{j,s} \right\rangle = \left. \frac{\delta}{\delta f_{i,t} \delta f_{j,s}} \left\langle 1 \right\rangle \right|_{f_s \to 0} \tag{B.79}$$

The two-point correlators needed to calculate $\left\langle Q_i^{(1)} \right\rangle_{B_t}$ and $\left\langle Q_i^{(2)} \right\rangle_{B_t}$ are summarized

as follows

$$\left\langle v_t v_s^T \right\rangle = \frac{1}{2\gamma}(\left\langle v_t \eta_s^T \right\rangle + \left\langle v_s \eta_t^T \right\rangle^T), \tag{B.80}$$

$$\left\langle v_t \eta_s^T \right\rangle = 2\gamma T_a \int \frac{\mathrm{d}\omega}{2\pi} e^{i\omega(t-s)} i\omega h(\omega) G^+(\omega), \tag{B.81}$$

$$\left\langle \eta_t \eta_s^T \right\rangle = 2\gamma T_a \int \frac{\mathrm{d}\omega}{2\pi} e^{i\omega(t-s)} h(\omega), \tag{B.82}$$

$$\left\langle v_t i u_s^T \right\rangle = \int \frac{\mathrm{d}\omega}{2\pi} e^{i\omega(t-s)} i\omega G^+(\omega), \tag{B.83}$$

$$\left\langle \eta_t i u_s^T \right\rangle = 0, \tag{B.84}$$

$$\left\langle i u_t i u_s^T \right\rangle = 0. \tag{B.85}$$

B.3.3 First order perturbation

From Eq. (3.14),(3.12), the first order energy flux reads

$$\left\langle q_i(t)^{(1)} \right\rangle_{B_t} = -\int \mathrm{d}s \, \Delta B_s \left\langle (-\gamma (P_i v_t)^T P_i v_t + (P_i v_t)^T P_i \eta_t) i u_s^T A v_s \right\rangle. \tag{B.86}$$

Using the Wick's theorem Eq. (3.17) and Eq. (B.84), the first and the second term are reduced to,

$$-\gamma \left\langle (P_i v_t)^T P_i v_t i u_s^T A v_s \right\rangle = -\gamma (\operatorname{tr} P_i \left\langle v_t v_t^T \right\rangle \operatorname{tr} A \left\langle v_s i u_s^T \right\rangle + 2 \operatorname{tr} P_i \left\langle v_t i u_s^T \right\rangle A \left\langle v_s v_t^T \right\rangle), \tag{B.87}$$

$$\left\langle (P_i v_t)^T P_i \eta_t i u_s^T A v_s \right\rangle = \operatorname{tr} P_i \left\langle v_t \eta_t^T \right\rangle \operatorname{tr} A \left\langle v_s i u_s^T \right\rangle + \operatorname{tr} P_i \left\langle v_t i u_s^T \right\rangle A \left\langle v_s \eta_t^T \right\rangle. \tag{B.88}$$

The sum of the first term on both RHS vanishes due to

$$(-\gamma \operatorname{tr} P_i \left\langle v_t v_t^T \right\rangle + \operatorname{tr} P_i \left\langle v_t \eta_t^T \right\rangle) = \langle q_i(t) \rangle = 0. \tag{B.89}$$

The sum of the second term on both RHS can be simplified to $-\operatorname{tr} P_i \left\langle v_t i u_s^T \right\rangle A \left\langle v_s \eta_t^T \right\rangle^T$,

where Eq. (B.80) has been used. Plugging in expressions for correlators presented in Appendix B.3.2, we get

$$\left\langle q_i(t)^{(1)} \right\rangle_{B_t} = 2\gamma T_a \int \frac{\mathrm{d}\omega}{2\pi}\frac{\mathrm{d}\omega'}{2\pi}\,\mathrm{d}s\,\Delta B_s e^{i(\omega-\omega')(t-s)}(i\omega)(i\omega')h(\omega')\,\mathrm{tr}\Big[P_i G^+(\omega)AG^+(\omega')^T\Big]. \tag{B.90}$$

Integration over s can be written with the Fourier transform of ΔB,

$$\int \mathrm{d}s\,\Delta B_s e^{i(\omega-\omega')(t-s)} = \Delta\tilde{B}(\omega-\omega')e^{i(\omega-\omega')t}. \tag{B.91}$$

We then integrate over t. Since $\Delta B(t)$ is a periodic function with period T, it can be expanded in discrete Fourier modes,

$$\Delta B(t) = \sum_{n=-\infty}^{\infty} \Delta\tilde{B}_n e^{i\omega_n t}, \quad \omega_n = \frac{2\pi n}{T}, \tag{B.92}$$

$$\Delta\tilde{B}(\omega) = \sum_n \Delta\tilde{B}_n 2\pi\delta(\omega-\omega_n), \tag{B.93}$$

$$\Delta\tilde{B}_n = \Delta\tilde{B}^*_{-n}, \tag{B.94}$$

where the last line follows from $\Delta B(t) = \Delta B(t)^*$.

Then the integration

$$\int_0^T \mathrm{d}t\, e^{i\omega_n t} = \begin{cases} T, & \text{if } \omega_n = 0 \\ \frac{1}{i\omega_n}(e^{i\omega_n T}-1) = 0, & \text{if } \omega_n \neq 0 \end{cases} \tag{B.95}$$

$$= T\delta_{n,0}. \tag{B.96}$$

With these properties, we have

$$f_1(\omega,\omega') = 2\gamma T_a (i\omega)(i\omega') h(\omega') \operatorname{tr}\Big[P_i G^+(\omega) A G^+(\omega')^T\Big], \tag{B.97}$$

$$\Big\langle q_i(t)^{(1)} \Big\rangle_{B_t} = \int \frac{\mathrm{d}\omega}{2\pi}\frac{\mathrm{d}\omega'}{2\pi} \Delta\tilde{B}(\omega-\omega') e^{i(\omega-\omega')t} f_1(\omega,\omega') \tag{B.98}$$

$$= \sum_n \int \frac{\mathrm{d}\omega}{2\pi}\frac{\mathrm{d}\omega'}{2\pi} \Delta\tilde{B}_n 2\pi\delta(\omega-\omega'-\omega_n) e^{i(\omega-\omega')t} f_1(\omega,\omega') \tag{B.99}$$

$$= \sum_n \int \frac{\mathrm{d}\omega}{2\pi} \Delta\tilde{B}_n e^{i\omega_n t} f_1(\omega,\omega-\omega_n), \tag{B.100}$$

$$\int_0^T \mathrm{d}t \Big\langle q_i(t)^{(1)} \Big\rangle_{B_t} = \sum_n \int \frac{\mathrm{d}\omega}{2\pi} \Delta\tilde{B}_n f_1(\omega,\omega-\omega_n) \int_0^T \mathrm{d}t\, e^{i\omega_n t} \tag{B.101}$$

$$= T \int \frac{\mathrm{d}\omega}{2\pi} \Delta\tilde{B}_0 f_1(\omega,\omega). \tag{B.102}$$

So we get

$$\Big\langle Q_i^{(1)} \Big\rangle_{B_t} = 2\gamma T_a T \int \frac{\mathrm{d}\omega}{2\pi} \Delta\tilde{B}_0 h(\omega)(i\omega)^2 \operatorname{tr}\Big[P_i G^+(\omega) A G^+(\omega)^T\Big]. \tag{B.103}$$

Since $(G^+(\omega)^T P_i G^+(\omega))$ is a symmetric matrix and A is an antisymmetric matrix, the trace vanishes,

$$\operatorname{tr}\Big[P_i G^+(\omega) A G^+(\omega)^T\Big] = \operatorname{tr}\Big[A(G^+(\omega)^T P_i G^+(\omega))\Big] = 0. \tag{B.104}$$

We conclude

$$\Big\langle Q_i^{(1)} \Big\rangle_{B_t} = 0. \tag{B.105}$$

B.3.4 Second order perturbation

From Eq. (3.15),(3.12), the second order reads

$$\left\langle q_i(t)^{(2)} \right\rangle_{B_t} = \left\langle q_i(t) \frac{1}{2} \int \mathrm{d}s\, \mathrm{d}s'\, (\Delta B_s i u_s^T A v_s)(\Delta B_{s'} i u_{s'}^T A v_{s'}) \right\rangle . \tag{B.106}$$

In this expression we encounter six-point correlators, which emits 15 terms using the Wick's theorem,

$$\begin{aligned}
&\left\langle a^T b c^T d e^T f \right\rangle = \\
&\mathrm{tr}\left\langle ab^T \right\rangle \mathrm{tr}\left\langle cd^T \right\rangle \mathrm{tr}\left\langle ef^T \right\rangle + \mathrm{tr}\left\langle ab^T \right\rangle \mathrm{tr}\left\langle ce^T \right\rangle \left\langle fd^T \right\rangle + \mathrm{tr}\left\langle ab^T \right\rangle \mathrm{tr}\left\langle cf^T \right\rangle \left\langle ed^T \right\rangle \\
&+ \mathrm{tr}\left\langle ac^T \right\rangle \left\langle db^T \right\rangle \mathrm{tr}\left\langle ef^T \right\rangle + \mathrm{tr}\left\langle ac^T \right\rangle \left\langle df^T \right\rangle \left\langle eb^T \right\rangle + \mathrm{tr}\left\langle ac^T \right\rangle \left\langle de^T \right\rangle \left\langle fb^T \right\rangle \\
&+ \mathrm{tr}\left\langle ad^T \right\rangle \left\langle cb^T \right\rangle \mathrm{tr}\left\langle ef^T \right\rangle + \mathrm{tr}\left\langle ad^T \right\rangle \left\langle cf^T \right\rangle \left\langle eb^T \right\rangle + \mathrm{tr}\left\langle ad^T \right\rangle \left\langle ce^T \right\rangle \left\langle fb^T \right\rangle \\
&+ \mathrm{tr}\left\langle ae^T \right\rangle \left\langle fd^T \right\rangle \left\langle cb^T \right\rangle + \mathrm{tr}\left\langle ae^T \right\rangle \left\langle fc^T \right\rangle \left\langle db^T \right\rangle + \mathrm{tr}\left\langle ae^T \right\rangle \left\langle fb^T \right\rangle \mathrm{tr}\left\langle cd^T \right\rangle \\
&+ \mathrm{tr}\left\langle af^T \right\rangle \left\langle ed^T \right\rangle \left\langle cb^T \right\rangle + \mathrm{tr}\left\langle af^T \right\rangle \left\langle ec^T \right\rangle \left\langle db^T \right\rangle + \mathrm{tr}\left\langle af^T \right\rangle \left\langle eb^T \right\rangle \mathrm{tr}\left\langle cd^T \right\rangle .
\end{aligned} \tag{B.107}$$

Many of these terms will turn out to vanish, which greatly simplifies the calculation. Our first task is to identify these vanishing terms.

The second order perturbation can be expanded as

$$\begin{aligned}
\int \mathrm{d}t \left\langle q_i(t)^{(2)} \right\rangle_{B_t} = \frac{1}{2}[&\int \mathrm{d}t \left\langle q_i(t) \right\rangle \int \mathrm{d}s\, \Delta B_s \left\langle i u_s^T A v_s \right\rangle \int \mathrm{d}s'\, \Delta B_{s'} \left\langle i u_{s'}^T A v_{s'} \right\rangle \\
&+ \int \mathrm{d}t\, \mathrm{d}s\, \Delta B_s \left\langle q_i(t) i u_s^T A v_s \right\rangle_c \int \mathrm{d}s'\, \Delta B_{s'} \left\langle i u_{s'}^T A v_{s'} \right\rangle \\
&+ \int \mathrm{d}s\, \Delta B_s \left\langle i u_s^T A v_s \right\rangle \int \mathrm{d}t\, \mathrm{d}s'\, \Delta B_{s'} \left\langle q_i(t) i u_{s'}^T A v_{s'} \right\rangle_c \\
&+ \int \mathrm{d}t\, \mathrm{d}s\, \mathrm{d}s'\, \Delta B_s \Delta B_{s'} \left\langle q_i(t) i u_s^T A v_s i u_{s'}^T A v_{s'} \right\rangle_c],
\end{aligned} \tag{B.108}$$

where subscript "c" means the terms are "connected" inside the same trace. The 1st term

vanish due to $\langle q_i \rangle = 0$. The 2nd and 3rd term vanish due to

$$\int \mathrm{d}t \left\langle q_i(t)^{(1)} \right\rangle_{B_t} = -\int \mathrm{d}t\, \mathrm{d}s\, \Delta B_s \left\langle q_i i u_s^T A v_s \right\rangle = 0. \tag{B.109}$$

So we only need to consider the last term that involves trace connecting all 6 points.

From Eq. (B.107), these terms are

$$\begin{aligned}\left\langle a^T b c^T d e^T f \right\rangle_c = &\operatorname{tr}\left\langle a c^T \right\rangle \left\langle d f^T \right\rangle \left\langle e b^T \right\rangle + \operatorname{tr}\left\langle a c^T \right\rangle \left\langle d e^T \right\rangle \left\langle f b^T \right\rangle + \operatorname{tr}\left\langle a d^T \right\rangle \left\langle c f^T \right\rangle \left\langle e b^T \right\rangle \\ &+ \operatorname{tr}\left\langle a d^T \right\rangle \left\langle c e^T \right\rangle \left\langle f b^T \right\rangle + \operatorname{tr}\left\langle a e^T \right\rangle \left\langle f d^T \right\rangle \left\langle c b^T \right\rangle + \operatorname{tr}\left\langle a e^T \right\rangle \left\langle f c^T \right\rangle \left\langle d b^T \right\rangle \\ &+ \operatorname{tr}\left\langle a f^T \right\rangle \left\langle e d^T \right\rangle \left\langle c b^T \right\rangle + \operatorname{tr}\left\langle a f^T \right\rangle \left\langle e c^T \right\rangle \left\langle d b^T \right\rangle .\end{aligned} \tag{B.110}$$

We now plug in the expression $q_i(t) = -\gamma (P_i v_t)^T P_i v_t + (P_i v_t)^T P_i \eta_t$ (Eq. (3.12)).

To calculate the dissipation part, we apply Eq. (B.110) with $a = b = P_i v_t, c = i u_s, d = A v_s, e = i u_{s'}, f = A v_{s'}$, and noticing $\left\langle c e^T \right\rangle = 0, A^T = -A$,

$$\begin{aligned}-\gamma \left\langle (P_i v_t)^T P_i v_t i u_s^T A v_s i u_{s'}^T A v_{s'} \right\rangle_c = -2\gamma (&- \operatorname{tr} P_i \left\langle v_t i u_s^T \right\rangle A \left\langle v_s v_{s'}^T \right\rangle A \left\langle i u_{s'} v_t^T \right\rangle \\ &+ \operatorname{tr} P_i \left\langle v_t i u_s^T \right\rangle A \left\langle v_s i u_{s'}^T \right\rangle A \left\langle v_{s'} v_t^T \right\rangle \\ &+ \operatorname{tr} P_i \left\langle v_t v_s^T \right\rangle A \left\langle i u_s v_{s'}^T \right\rangle A \left\langle i u_{s'} v_t^T \right\rangle).\end{aligned} \tag{B.111}$$

Similarly, the fluctuation part can be written with $a = P_i v_t, b = P_i \eta_t, c = i u_s, d = A v_s, e = i u_{s'}, f = A v_{s'}$, and notice that $\left\langle b c^T \right\rangle = \left\langle b e^T \right\rangle = \left\langle c e^T \right\rangle = 0$,

$$\left\langle (P_i v_t)^T P_i \eta_t i u_s^T A v_s i u_{s'}^T A v_{s'} \right\rangle_c = \operatorname{tr} P_i \left\langle v_t i u_s^T \right\rangle A \left\langle v_s i u_{s'}^T \right\rangle A \left\langle v_{s'} \eta_t^T \right\rangle \tag{B.112}$$

$$+ \operatorname{tr} P_i \left\langle v_t i u_{s'}^T \right\rangle A \left\langle v_{s'} i u_s^T \right\rangle A \left\langle v_s \eta_t^T \right\rangle . \tag{B.113}$$

The sum of the 2nd term in Eq. (B.111) and the 1st term in Eq. (B.113) gives

$$-2\gamma \operatorname{tr} P_i \left\langle v_t i u_s^T \right\rangle A \left\langle v_s i u_{s'}^T \right\rangle A \left\langle v_{s'} v_t^T \right\rangle + \operatorname{tr} P_i \left\langle v_t i u_s^T \right\rangle A \left\langle v_s i u_{s'}^T \right\rangle A \left\langle v_{s'} \eta_t^T \right\rangle \quad \text{(B.114)}$$

$$= \operatorname{tr} P_i \left\langle v_t i u_s^T \right\rangle A \left\langle v_s i u_{s'}^T \right\rangle A(-2\gamma \frac{\left\langle v_{s'} \eta_t^T \right\rangle + \left\langle v_t \eta_{s'}^T \right\rangle^T}{2\gamma} + \left\langle v_{s'} \eta_t^T \right\rangle) \quad \text{(B.115)}$$

$$= -\operatorname{tr} P_i \left\langle v_t i u_s^T \right\rangle A \left\langle v_s i u_{s'}^T \right\rangle A \left\langle v_t \eta_{s'}^T \right\rangle^T . \quad \text{(B.116)}$$

The sum of the 3rd term in Eq. (B.111) and the 2nd term in Eq. (B.113) gives

$$-2\gamma \operatorname{tr} P_i \left\langle v_t v_s^T \right\rangle A \left\langle i u_s v_{s'}^T \right\rangle A \left\langle i u_{s'} v_t^T \right\rangle + \operatorname{tr} P_i \left\langle v_t i u_{s'}^T \right\rangle A \left\langle v_{s'} i u_s^T \right\rangle A \left\langle v_s \eta_t^T \right\rangle \quad \text{(B.117)}$$

$$= -\operatorname{tr} P_i \left\langle v_t i u_{s'}^T \right\rangle A \left\langle v_{s'} i u_s^T \right\rangle A \left\langle v_t \eta_s^T \right\rangle^T . \quad \text{(B.118)}$$

The remaining 1st term in Eq. (B.111) reads

$$-2\gamma(-\operatorname{tr} P_i \left\langle v_t i u_s^T \right\rangle A \left\langle v_s v_{s'}^T \right\rangle A \left\langle i u_{s'} v_t^T \right\rangle) \quad \text{(B.119)}$$

$$= \operatorname{tr} P_i \left\langle v_t i u_s^T \right\rangle A \left\langle v_s \eta_{s'}^T \right\rangle A \left\langle i u_{s'} v_t^T \right\rangle + \operatorname{tr} P_i \left\langle v_t i u_s^T \right\rangle A \left\langle v_{s'} \eta_s^T \right\rangle^T A \left\langle i u_{s'} v_t^T \right\rangle . \quad \text{(B.120)}$$

Now we return to the quantity $\left\langle q_i(t)^{(2)} \right\rangle_{B_t}$. Under integration over s, s', the two terms on RHS of Eq. (B.120) are equal. RHS of Eq. (B.116) and that of Eq. (B.118) are also equal. Combining with Eq. (B.111), we get

$$\begin{aligned} \left\langle q_i(t)^{(2)} \right\rangle_{B_t} = \int \mathrm{d}s\, \mathrm{d}s'\, \Delta B_s \Delta B_{s'} (&\operatorname{tr} P_i \left\langle v_t i u_s^T \right\rangle A \left\langle v_s \eta_{s'}^T \right\rangle A \left\langle i u_{s'} v_t^T \right\rangle \\ &- \operatorname{tr} P_i \left\langle v_t i u_s^T \right\rangle A \left\langle v_s i u_{s'}^T \right\rangle A \left\langle v_t \eta_{s'}^T \right\rangle^T). \end{aligned}$$

This expression only contains two term, which is a much simplified compared with the original 15×2 terms.

We first look at the first term on RHS of Eq. (B.121),

$$\left\langle q_i(t)^{(2)} \right\rangle_{B_t,1} = \int \mathrm{d}s\, \mathrm{d}s'\, \Delta B_s \Delta B_{s'}\, \mathrm{tr}\, P_i \left\langle v_t i u_s^T \right\rangle A \left\langle v_s \eta_{s'}^T \right\rangle A \left\langle i u_{s'} v_t^T \right\rangle \tag{B.121}$$

$$= \int \frac{\mathrm{d}\omega}{2\pi} \frac{\mathrm{d}\omega'}{2\pi} \frac{\mathrm{d}\omega''}{2\pi}\, \mathrm{d}s\, \mathrm{d}s'\, \Delta B_s \Delta B_{s'} e^{i\omega(t-s)} e^{i\omega'(s-s')} e^{i\omega''(t-s')} f_{21}(\omega, \omega', \omega''), \tag{B.122}$$

$$f_{21}(\omega, \omega', \omega'') = 2\gamma T_a (i\omega)(i\omega')(i\omega'') h(\omega')\, \mathrm{tr}\, P_i G^+(\omega) A G^+(\omega') A G^+(\omega'')^T. \tag{B.123}$$

Integrating over s, s'

$$\int \mathrm{d}s\, \mathrm{d}s'\, \Delta B_s \Delta B_{s'} e^{i\omega(t-s)} e^{i\omega'(s-s')} e^{i\omega''(t-s')} = e^{i(\omega+\omega'')t} \Delta\tilde{B}(\omega - \omega') \Delta\tilde{B}(\omega' + \omega''), \tag{B.124}$$

we get

$$\left\langle q_i(t)^{(2)} \right\rangle_{B_t,1} = \int \frac{\mathrm{d}\omega}{2\pi} \frac{\mathrm{d}\omega'}{2\pi} \frac{\mathrm{d}\omega''}{2\pi} e^{i(\omega+\omega'')t} \Delta\tilde{B}(\omega - \omega') \Delta\tilde{B}(\omega' + \omega'') f_{21}(\omega, \omega', \omega'') \tag{B.125}$$

$$= \sum_{n,n'} \int \frac{\mathrm{d}\omega}{2\pi} e^{i(\omega_n + \omega_{n'})t} \Delta\tilde{B}_n \Delta\tilde{B}_{n'} f_{21}(\omega, \omega - \omega_n, -\omega + \omega_n + \omega_{n'}), \tag{B.126}$$

where we have expressed $\Delta\tilde{B}(\omega)$ in terms of discrete Fourier modes Eq. (B.93).

Integrate over t and using Eq. (B.96),

$$\int_0^T \mathrm{d}t \left\langle q_i(t)^{(2)} \right\rangle_{B_t,1} = \sum_{n,n'} \int \frac{\mathrm{d}\omega}{2\pi} \int_0^T \mathrm{d}t\, e^{i(\omega_n + \omega_{n'})t} \Delta\tilde{B}_n \Delta\tilde{B}_{n'} f_{21}(\omega, \omega - \omega_n, -\omega + \omega_n + \omega_{n'}) \tag{B.127}$$

$$= T \sum_n \int \frac{\mathrm{d}\omega}{2\pi} |\Delta\tilde{B}_n|^2 f_{21}(\omega, \omega - \omega_n, -\omega) \tag{B.128}$$

$$= 2\gamma T_a T \sum_n \int \frac{\mathrm{d}\omega}{2\pi} |\Delta\tilde{B}_n|^2 \Big\{ i\omega^2 (\omega - \omega_n) h(\omega - \omega_n) \tag{B.129}$$

$$\mathrm{tr}\, P_i G^+(\omega) A G^+(\omega - \omega_n) A G^+(-\omega)^T \Big\}. \tag{B.130}$$

The second term in Eq. (B.121) can be simplified similarly,

$$\left\langle q_i(t)^{(2)} \right\rangle_{B_t,2} = \int \mathrm{d}s\, \mathrm{d}s'\, \Delta B_s \Delta B_{s'}\, \mathrm{tr}\, P_i \left\langle v_t i u_s^T \right\rangle A \left\langle v_s i u_{s'}^T \right\rangle A \left\langle v_t \eta_{s'}^T \right\rangle^T \tag{B.131}$$

$$= 2\gamma T_a T \sum_n \int \frac{\mathrm{d}\omega}{2\pi} |\Delta \tilde{B}_n|^2 \Big\{ i\omega^2(\omega - \omega_n) h(\omega) \mathrm{tr}\, P_i G^+(\omega) A G^+(\omega - \omega_n) A G^+(-\omega)^T \Big\}, \tag{B.132}$$

where we have used $h(-\omega) = h(\omega)$.

Combining Eq. (B.130),(B.132) with $\left\langle Q_i^{(2)} \right\rangle_{B_t} = \int_0^T \mathrm{d}t\, (\left\langle q_i(t)^2 \right\rangle_{B_t,1} - \left\langle q_i(t)^2 \right\rangle_{B_t,2})$, we arrive at

$$\left\langle Q_i^{(2)} \right\rangle_{B_t} = 2\gamma T_a T \sum_{n=-\infty}^{\infty} |\Delta \tilde{B}_n|^2 \int \frac{\mathrm{d}\omega}{2\pi} \Big\{ i\omega^2(\omega - \omega_n)(h(\omega - \omega_n) - h(\omega)) \mathrm{tr}\, P_i G^+(\omega) A G^+(\omega - \omega_n) A G^+(-\omega)^T \Big\}. \tag{B.133}$$

The ω_n and $-\omega_n$ terms are actually conjugate pairs,

$$[i\omega^2(\omega - \omega_n)(h(\omega - \omega_n) - h(\omega))\, \mathrm{tr}\, P_i G^+(\omega) A G^+(\omega - \omega_n) A G^+(-\omega)^T]^* \tag{B.134}$$

$$= \int \mathrm{d}\omega\, (-i)\omega^2(\omega - \omega_n)(h(\omega - \omega_n) - h(\omega))\, \mathrm{tr}\, P_i G^+(-\omega) A G^+(-\omega + \omega_n) A G^+(\omega)^T \tag{B.135}$$

$$= \int \mathrm{d}\omega\, i\omega^2(\omega + \omega_n)(h(\omega + \omega_n) - h(\omega))\, \mathrm{tr}\, P_i G^+(\omega) A G^+(\omega + \omega_n) A G^+(-\omega)^T, \tag{B.136}$$

where in the second equality we have changed the dummy variable $\omega \to -\omega$ and used $h(-\omega) = h(\omega)$. From this relation, we see that $\left\langle Q_i^{(2)} \right\rangle_{B_t}$ is real for any pair $\{n, -n\}$. We arrive at the central result for this section,

$$\left\langle Q_i^{(2)} \right\rangle_{B_t} = 4\gamma T_a T \sum_{n=1}^{\infty} |\Delta \tilde{B}_n|^2 \int \frac{\mathrm{d}\omega}{2\pi} \Big\{ \omega^2(\omega + \omega_n)(h(\omega + \omega_n) - h(\omega)) \mathrm{Re}[i\, \mathrm{tr}\, P_i G^+(\omega) A G^+(\omega + \omega_n) A G^+(-\omega)^T] \Big\}. \tag{B.137}$$

From this expression, we see couplings between $G^+(\omega)$ at different ω's, but no couplings between $\Delta\tilde{B}_n$ at different $|n|$'s.

As a sanity check, we now demonstrate the energy balance, $\sum_i \left\langle Q_i^{(2)} \right\rangle_{B_t} = 0$. We use $\sum_i P_i = I$, and denote

$$f_{Q,n} = 2\gamma \int \frac{\mathrm{d}\omega}{2\pi} i\omega^2(\omega-\omega_n)(h(\omega-\omega_n)-h(\omega)) \operatorname{tr} G^+(\omega)AG^+(\omega-\omega_n)AG^+(-\omega)^T. \tag{B.138}$$

Using $G^{-T} - G^+ = 2i\omega\gamma G^+G^{-T} = 2i\omega\gamma G^{-T}G^+$,

$$f_{Q,n} = \int \frac{\mathrm{d}\omega}{2\pi} \omega(\omega-\omega_n)(h(\omega-\omega_n)-h(\omega)) \operatorname{tr} AG^+(\omega-\omega_n)A(G^{-T}(\omega)-G^+(\omega)). \tag{B.139}$$

Similarly, $f_{Q,-n}$ reads

$$\begin{aligned} f_{Q,-n} = -\int \frac{\mathrm{d}\omega}{2\pi} \omega(\omega-\omega_n)(h(\omega-\omega_n)-h(\omega))(&\operatorname{tr} AG^+(\omega)AG^{-T}(\omega-\omega_n) \\ &- \operatorname{tr} AG^+(\omega)AG^+(\omega-\omega_n)). \end{aligned} \tag{B.140}$$

Comparing $f_{Q,n}$ and $f_{Q,-n}$,

$$\operatorname{tr} AG^+(\omega)AG^+(\omega-\omega_n) = \operatorname{tr} AG^+(\omega-\omega_n)AG^+(\omega), \tag{B.141}$$

$$\operatorname{Re}\operatorname{tr} AG^+(\omega)AG^{-T}(\omega-\omega_n) = \operatorname{Re}\operatorname{tr} AG^-(\omega-\omega_n)AG^+(\omega)^T \tag{B.142}$$

$$= \operatorname{Re}\operatorname{tr} AG^+(\omega-\omega_n)AG^+(-\omega)^T. \tag{B.143}$$

We see that the real part of $f_{Q,n}$ and $f_{Q,-n}$ are opposite, $\operatorname{Re} f_{Q,-n} = -\operatorname{Re} f_{Q,n}$. The energy balance follows,

$$\sum_i \left\langle Q_i^{(2)} \right\rangle \propto f_{Q,n} + f_{Q,-n} = \operatorname{Re}(f_{Q,n} + f_{Q,-n}) = 0. \tag{B.144}$$

B.4 Diagrams that consist of only loops

In this section, we try to show analytically that diagrams with only loops ($i \to i \to \cdots \to i$) vanish.

For diagrams with only loops, the expression $M[\cdot]$ simplifies to multiplication of the same matrix. Denoting $(-K_s)_{ii} = M_i$, $f_{i,n;l;|l|_1,|l|_2,|l|_3}$ reads

$$f_{i,n;l;|l|_1,|l|_2,|l|_3} = f_{M_i,1}(|l|_1,|l|_2,|l|_3) - f_{M_i,2}(|l|_1,|l|_2,|l|_3), \tag{B.145}$$

$$\begin{aligned} f_{M_i,1}(|l|_1,|l|_2,|l|_3) = 2\,\mathrm{Re}\int \frac{\mathrm{d}\omega}{2\pi}\omega(\omega+\omega_n)(h(\omega+\omega_n)-h(\omega))\,\mathrm{tr}\Big\{ & (M_i g^+(\omega))^{|l|_3} A \\ & (g^+(\omega+\omega_n)M_i)^{|l|_2} g^+(\omega+\omega_n) A (g^+(-\omega)^T M_i)^{|l|_1} g^+(-\omega)^T \Big\}, \end{aligned} \tag{B.146}$$

$$\begin{aligned} f_{M_i,2}(|l|_1,|l|_2,|l|_3) = 2\,\mathrm{Re}\int \frac{\mathrm{d}\omega}{2\pi}\omega(\omega+\omega_n)(h(\omega+\omega_n)-h(\omega))\,\mathrm{tr}\Big\{ & (M_i g^+(\omega))^{|l|_3} A \\ & (g^+(\omega+\omega_n)M_i)^{|l|_2} g^+(\omega+\omega_n) A (g^+(-\omega)^T M_i)^{|l|_1} g^+(\omega) \Big\}, \end{aligned} \tag{B.147}$$

where we have splited into two terms.

We find the following three relations,

$$f_{M_i,1}(|l|_1,|l|_2,|l|_3) = f_{M_i,2}(|l|_1+1,|l|_2,|l|_3-1), \tag{B.148}$$

$$f_{M_i,1}(|l|_1,|l|_2,0) = -f_{M_i,1}(|l|_2,|l|_1,0), \tag{B.149}$$

$$f_{M_i,2}(0,|l|_2,|l|_3) = -f_{M_i,2}(0,|l|_3,|l|_2). \tag{B.150}$$

With these relations, $f_{i,n;l}$ can be prove to be zero.

$$f_{i,n;l} = \sum_{|l|_1+|l|_2+|l|_3=l} f_{M_i,1}(|l|_1,|l|_2,|l|_3) - f_{M_i,2}(|l|_1,|l|_2,|l|_3) \tag{B.151}$$

$$= \sum_{|l|_1=0}^{l-1} \sum_{|l|_2=0}^{l-1-|l|_1} f_{M_i,1}(|l|_1,|l|_2,l-|l|_1-|l|_2) + \sum_{|l|_1=0}^{l} f_{M_i,1}(|l|_1,l-|l|_1,0)$$

$$- \sum_{|l|_1=1}^{l} \sum_{|l|_2=0}^{l-|l|_1} f_{M_i,2}(|l|_1,|l|_2,l-|l|_1-|l|_2) - \sum_{|l|_2=0}^{l} f_{M_i,2}(0,|l|_2,l-|l|_2) \tag{B.152}$$

$$= 0. \tag{B.153}$$

Next we prove the above three relations.

To prove the first relation,

$$f_{M_i,2}(|l|_1+1,|l|_2,|l|_3-1)$$

$$= 2\,\mathrm{Re}\int \frac{\mathrm{d}\omega}{2\pi}\omega(\omega+\omega_n)(h(\omega+\omega_n)-h(\omega))\,\mathrm{tr}\Big\{(M_i g^+(\omega))^{|l|_3-1}A$$

$$(g^+(\omega+\omega_n)M_i)^{|l|_2}g^+(\omega+\omega_n)A(g^+(-\omega)^T M_i)^{|l|_1}g^+(-\omega)^T M_i g^+(\omega)\Big\} \tag{B.154}$$

$$= 2\,\mathrm{Re}\int \frac{\mathrm{d}\omega}{2\pi}\omega(\omega+\omega_n)(h(\omega+\omega_n)-h(\omega))\,\mathrm{tr}\Big\{M_i g^+(\omega)(M_i g^+(\omega))^{|l|_3-1}A$$

$$(g^+(\omega+\omega_n)M_i)^{|l|_2}g^+(\omega+\omega_n)A(g^+(-\omega)^T M_i)^{|l|_1}g^+(-\omega)^T\Big\} \tag{B.155}$$

$$= f_{M_i,1}(|l|_1,|l|_2,|l|_3). \tag{B.156}$$

To prove the second relation,

$$
\begin{aligned}
&f_{M_i,1}(|l|_1,|l|_2,0)\\
&=2\,\mathrm{Re}\int\frac{\mathrm{d}\omega}{2\pi}\omega(\omega+\omega_n)(h(\omega+\omega_n)-h(\omega))\,\mathrm{tr}\Big\{Ag^+(-\omega)(M_ig^+(-\omega))^{|l|_1}A\\
&(g^+(\omega+\omega_n)^TM_i)^{|l|_2}g^+(\omega+\omega_n)^T\Big\} \qquad \text{(B.157)}\\
&=2\,\mathrm{Re}\int\frac{\mathrm{d}\omega'}{2\pi}(\omega'+\omega_n)\omega'(h(\omega')-h(\omega'+\omega_n))\,\mathrm{tr}\Big\{Ag^+(\omega'+\omega_n)(M_ig^+(\omega'+\omega_n))^{|l|_1}A\\
&(g^+(-\omega')^TM_i)^{|l|_2}g^+(-\omega')^T\Big\} \qquad \text{(B.158)}\\
&=-f_{M_i,1}(|l|_2,|l|_1,0). \qquad \text{(B.159)}
\end{aligned}
$$

To prove the third relation,

$$
\begin{aligned}
&f_{M_i,2}(0,|l|_2,|l|_3)\\
&=2\,\mathrm{Re}\int\frac{\mathrm{d}\omega}{2\pi}\omega(\omega+\omega_n)(h(\omega+\omega_n)-h(\omega))\,\mathrm{tr}\Big\{(g^+(\omega+\omega_n)M_i)^{|l|_2}\\
&g^+(\omega+\omega_n)Ag^+(\omega)(M_ig^+(\omega))^{|l|_3}A\Big\} \qquad \text{(B.160)}\\
&=2\,\mathrm{Re}\int\frac{\mathrm{d}\omega}{2\pi}\omega(\omega+\omega_n)(h(\omega+\omega_n)-h(\omega))\,\mathrm{tr}\Big\{g^+(-\omega)(M_ig^+(-\omega))^{|l|_3}\\
&A(g^+(-\omega-\omega_n)M_i)^{|l|_2}g^+(-\omega-\omega_n)A\Big\} \qquad \text{(B.161)}\\
&=-f_{M_i,2}(0,|l|_3,|l|_2). \qquad \text{(B.162)}
\end{aligned}
$$

REFERENCES

[1] Thermal conduction. *Wikipedia*, January 2020. Page Version ID: 933513381.

[2] Adolph Fick. V. *On liquid diffusion. The London, Edinburgh, and Dublin Philosophical Magazine and Journal of Science*, 10(63):30–39, July 1855.

[3] Ralf Metzler, Jae-Hyung Jeon, Andrey G. Cherstvy, and Eli Barkai. Anomalous diffusion models and their properties: Non-stationarity, non-ergodicity, and ageing at the centenary of single particle tracking. *Phys. Chem. Chem. Phys.*, 16(44):24128–24164, 2014.

[4] Stefano Lepri, Roberto Livi, and Antonio Politi. Thermal conduction in classical low-dimensional lattices. *Physics Reports*, 377(1):1–80, April 2003.

[5] A. Einstein. Über die von der molekularkinetischen Theorie der Wärme geforderte Bewegung von in ruhenden Flüssigkeiten suspendierten Teilchen. *Annalen der Physik*, 322(8):549–560, 1905.

[6] R. Kubo. The fluctuation-dissipation theorem. *Reports on Progress in Physics*, 29(1):255–284, January 1966.

[7] Umberto Marini Bettolo Marconi, Andrea Puglisi, Lamberto Rondoni, and Angelo Vulpiani. Fluctuation-dissipation: Response theory in statistical physics. *Physics Reports*, 461(4-6):111–195, 2008.

[8] Lars Onsager. Reciprocal Relations in Irreversible Processes. II. *Physical Review*, 38(12):2265–2279, December 1931.

[9] Lars Onsager. Reciprocal Relations in Irreversible Processes. I. *Physical Review*, 37(4):405–426, February 1931.

[10] S.R. de Groot and P. Mazur. *Non-Equilibrium Thermodynamics*. Dover Books on Physics. Dover Publications, 1984.

[11] Francis J. DiSalvo. Thermoelectric Cooling and Power Generation. *Science*, 285(5428):703–706, July 1999.

[12] Jennifer L Ross, M Yusuf Ali, and David M Warshaw. Cargo transport: Molecular motors navigate a complex cytoskeleton. *Current Opinion in Cell Biology*, 20(1):41–47, February 2008.

[13] Frank Jülicher, Armand Ajdari, and Jacques Prost. Modeling molecular motors. *Reviews of Modern Physics*, 69(4):1269–1282, October 1997.

[14] Peter Reimann. Brownian motors: Noisy transport far from equilibrium. *Physics Reports*, 361(2):57–265, April 2002.

[15] Jan A. Freund and Thorsten Pöschel. *Stochastic Processes in Physics, Chemistry, and Biology*. Springer Science & Business Media, October 2000.

[16] Brownian ratchet. *Wikipedia*, January 2020. Page Version ID: 933570305.

[17] Richard P. Feynman, Robert B. Leighton, and Matthew Sands. *The Feynman Lectures on Physics: The New Millennium Edition: Mainly Mechanics, Radiation, and Heat*. Basic Books, September 2015.

[18] C. Jarzynski and O. Mazonka. Feynman's ratchet and pawl: An exactly solvable model. *Physical Review E*, 59(6):6448–6459, June 1999.

[19] Jaehoon Bang, Rui Pan, Thai M Hoang, Jonghoon Ahn, Christopher Jarzynski, H T Quan, and Tongcang Li. Experimental realization of Feynman's ratchet. *New Journal of Physics*, 20(10):103032, October 2018.

[20] A. Mogilner and G. Oster. Cell motility driven by actin polymerization. *Biophysical Journal*, 71(6):3030–3045, December 1996.

[21] H. Wang and G. Oster. Ratchets, power strokes, and molecular motors. *Applied Physics A*, 75(2):315–323, August 2002.

[22] Wonmuk Hwang and Martin Karplus. Structural basis for power stroke vs. Brownian ratchet mechanisms of motor proteins. *Proceedings of the National Academy of Sciences*, 116(40):19777–19785, October 2019.

[23] Marcelo O. Magnasco. Forced thermal ratchets. *Physical Review Letters*, 71(10):1477–1481, September 1993.

[24] Laura Ibarra-Bracamontes and Víctor Romero-Rochín. Stochastic ratchets with colored thermal noise. *Physical Review E*, 56(4):4048–4051, October 1997.

[25] T. E. Dialynas, Katja Lindenberg, and G. P. Tsironis. Ratchet motion induced by deterministic and correlated stochastic forces. *Physical Review E*, 56(4):3976–3985, October 1997.

[26] Peter Hanggi and Peter Jung. Colored Noise in Dynamical Systems. In *Advances in Chemical Physics*, pages 239–326. John Wiley & Sons, Ltd, 1994.

[27] Étienne Fodor, Cesare Nardini, Michael E. Cates, Julien Tailleur, Paolo Visco, and Frédéric van Wijland. How Far from Equilibrium Is Active Matter? *Physical Review Letters*, 117(3):038103, July 2016.

[28] N. Koumakis, A. Lepore, C. Maggi, and R. Di Leonardo. Targeted delivery of colloids by swimming bacteria. *Nature Communications*, 4(1):1–6, October 2013.

[29] Peter Jung and Peter Hänggi. Dynamical systems: A unified colored-noise approximation. *Physical Review A*, 35(10):4464–4466, 1987.

[30] Li Cao, Da-jin Wu, and Xue-li Luo. Effects of saturation in the transient process of a dye laser. III. The case of colored noise with large and small correlation time. *Physical Review A*, 47(1):57–70, January 1993.

[31] Claudio Maggi, Umberto Marini Bettolo Marconi, Nicoletta Gnan, and Roberto Di Leonardo. Multidimensional stationary probability distribution for interacting active particles. *Scientific Reports*, 5:1–7, 2015.

[32] Nn Koumakis, C Maggi, and R Di Leonardo. Directed transport of active particles over asymmetric energy barriers. *Soft Matter*, 10:5695–5701, 2014.

[33] Cato Sandford, Alexander Y Grosberg, and Jean-François Joanny. Pressure and flow of exponentially self-correlated active particles. *Physical Review E*, 96(5):052605, November 2017.

[34] Xiao-Lun Wu and Albert Libchaber. Particle Diffusion in a Quasi-Two-Dimensional Bacterial Bath. *Physical Review Letters*, 84(13):3017–3020, March 2000.

[35] Claudio Maggi, Matteo Paoluzzi, Nicola Pellicciotta, Alessia Lepore, Luca Angelani, and Roberto Di Leonardo. Generalized Energy Equipartition in Harmonic Oscillators Driven by Active Baths. *Physical Review Letters*, 113(23):238303, December 2014.

[36] M. Büttiker. Transport as a consequence of state-dependent diffusion. *Zeitschrift für Physik B Condensed Matter*, 68(2-3):161–167, 1987.

[37] Rolf Landauer. Motion out of noisy states. *Journal of Statistical Physics*, 53(1-2):233–248, October 1988.

[38] Benjamin Lindner and Lutz Schimansky-Geier. Noise-Induced Transport with Low Randomness. *Physical Review Letters*, 89(23):6–9, 2002.

[39] A. Gomez-Marin and J. M. Sancho. Symmetric Brownian motor. *Physical Review E*, 71(2):021101, February 2005.

[40] Li Cao and Da-jin Wu. Fluctuation-induced transport in a spatially symmetric periodic potential. *Physical Review E*, 62(5):7478–7481, November 2000.

[41] S. Flach, O. Yevtushenko, and Y. Zolotaryuk. Directed Current due to Broken Time-Space Symmetry. *Physical Review Letters*, 84(11):2358–2361, March 2000.

[42] Thomas Guérin, Jacques Prost, Pascal Martin, and Jean-François Joanny. Coordination and collective properties of molecular motors: Theory. *Current Opinion in Cell Biology*, 22(1):14–20, February 2010.

[43] Peter Hänggi and Fabio Marchesoni. Artificial Brownian motors: Controlling transport on the nanoscale. *Reviews of Modern Physics*, 81(1):387–442, 2009.

[44] M E Cates. Diffusive transport without detailed balance in motile bacteria: Does microbiology need statistical physics? *Reports on Progress in Physics*, 75(4):042601, April 2012.

[45] Clemens Bechinger, Roberto Di Leonardo, Hartmut Löwen, Charles Reichhardt, Giorgio Volpe, and Giovanni Volpe. Active particles in complex and crowded environments. *Reviews of Modern Physics*, 88(4):045006, November 2016.

[46] C.J. Olson Reichhardt and C. Reichhardt. Ratchet Effects in Active Matter Systems. *Annual Review of Condensed Matter Physics*, 8(1):51–75, March 2017.

[47] J Elgeti, R G Winkler, and G Gompper. Physics of microswimmers—single particle motion and collective behavior: A review. *Reports on Progress in Physics*, 78(5):056601, May 2015.

[48] Samuel Sánchez, Lluís Soler, and Jaideep Katuri. Chemically Powered Micro- and Nanomotors. *Angewandte Chemie International Edition*, 54(5):1414–1444, 2015.

[49] P. Galajda, J. Keymer, P. Chaikin, and R. Austin. A Wall of Funnels Concentrates Swimming Bacteria. *Journal of Bacteriology*, 189(23):8704–8707, December 2007.

[50] R. Di Leonardo, L. Angelani, D. Dell'Arciprete, G. Ruocco, V. Iebba, S. Schippa, M. P. Conte, F. Mecarini, F. De Angelis, and E. Di Fabrizio. Bacterial ratchet motors. *Proceedings of the National Academy of Sciences*, 107(21):9541–9545, May 2010.

[51] S. Flach, Y. Zolotaryuk, A. E. Miroshnichenko, and M. V. Fistul. Broken Symmetries and Directed Collective Energy Transport in Spatially Extended Systems. *Physical Review Letters*, 88(18):184101, April 2002.

[52] Souvik Das, Onuttom Narayan, and Sriram Ramaswamy. Ratchet for energy transport between identical reservoirs. *Physical Review E*, 66(5):050103, November 2002.

[53] M. Terraneo, M. Peyrard, and G. Casati. Controlling the Energy Flow in Nonlinear Lattices: A Model for a Thermal Rectifier. *Physical Review Letters*, 88(9):094302, February 2002.

[54] Baowen Li, Lei Wang, and Giulio Casati. Thermal Diode: Rectification of Heat Flux. *Physical Review Letters*, 93(18):184301, October 2004.

[55] Nianbei Li, Jie Ren, Lei Wang, Gang Zhang, Peter Hänggi, and Baowen Li. Colloquium: Phononics: Manipulating heat flow with electronic analogs and beyond. *Reviews of Modern Physics*, 84(3):1045–1066, July 2012.

[56] N. Li, P. Hänggi, and B. Li. Ratcheting heat flux against a thermal bias. *EPL (Europhysics Letters)*, 84(4):40009, November 2008.

[57] Jie Ren and Baowen Li. Emergence and control of heat current from strict zero thermal bias. *Physical Review E*, 81(2):021111, February 2010.

[58] Kiyoshi Kanazawa, Takahiro Sagawa, and Hisao Hayakawa. Heat conduction induced by non-Gaussian athermal fluctuations. *Physical Review E*, 87(5):052124, May 2013.

[59] Michael M. Cândido, Welles A. M. Morgado, and Sílvio M. Duarte Queirós. Macroscopic violation of the law of heat conduction. *Physical Review E*, 96(3):032143, September 2017.

[60] E. H. Colombo, L. A. C. A. Defaveri, and C. Anteneodo. Heat flux direction controlled by power-law oscillators under non-Gaussian fluctuations. *Physical Review E*, 100(3):032118, September 2019.

[61] Jie Ren, Sha Liu, and Baowen Li. Geometric Heat Flux for Classical Thermal Transport in Interacting Open Systems. *Physical Review Letters*, 108(21):210603, May 2012.

[62] N. A Sinitsyn and I Nemenman. The Berry phase and the pump flux in stochastic chemical kinetics. *Europhysics Letters (EPL)*, 77(5):58001, March 2007.

[63] N. A. Sinitsyn and Ilya Nemenman. Universal Geometric Theory of Mesoscopic Stochastic Pumps and Reversible Ratchets. *Physical Review Letters*, 99(22):220408, November 2007.

[64] N. a. Sinitsyn. Stochastic pump effect and geometric phases in dissipative and stochastic systems. *Journal of Physics A: Mathematical and Theoretical*, 42:193001, 2009.

[65] Linxiao Zhu and Shanhui Fan. Persistent Directional Current at Equilibrium in Nonreciprocal Many-Body Near Field Electromagnetic Heat Transfer. *Physical Review Letters*, 117(13):134303, September 2016.

[66] Linxiao Zhu, Yu Guo, and Shanhui Fan. Theory of many-body radiative heat transfer without the constraint of reciprocity. *Physical Review B*, 97(9):094302, March 2018.

[67] Yonatan Dubi and Massimiliano Di Ventra. Colloquium: Heat flow and thermoelectricity in atomic and molecular junctions. *Reviews of Modern Physics*, 83(1):131–155, March 2011.

[68] Grzegorz Szamel. Self-propelled particle in an external potential: Existence of an effective temperature. *Physical Review E - Statistical, Nonlinear, and Soft Matter Physics*, 90(1):1–7, 2014.

[69] Ludovic Berthier and Jorge Kurchan. Lectures on non-equilibrium active systems. *arXiv:1906.04039 [cond-mat]*, June 2019.

[70] M. C. Marchetti, J. F. Joanny, S. Ramaswamy, T. B. Liverpool, J. Prost, Madan Rao, and R. Aditi Simha. Hydrodynamics of soft active matter. *Reviews of Modern Physics*, 85(3):1143–1189, July 2013.

[71] Craig W. Reynolds. Flocks, herds and schools: A distributed behavioral model. In *Proceedings of the 14th Annual Conference on Computer Graphics and Interactive Techniques*, SIGGRAPH '87, pages 25–34, New York, NY, USA, August 1987. Association for Computing Machinery.

[72] Tamás Vicsek, András Czirók, Eshel Ben-Jacob, Inon Cohen, and Ofer Shochet. Novel Type of Phase Transition in a System of Self-Driven Particles. *Physical Review Letters*, 75(6):1226–1229, August 1995.

[73] John Toner and Yuhai Tu. Long-Range Order in a Two-Dimensional Dynamical XY Model: How Birds Fly Together. *Physical Review Letters*, 75(23):4326–4329, December 1995.

[74] John Toner and Yuhai Tu. Flocks, herds, and schools: A quantitative theory of flocking. *Physical Review E*, 58(4):4828–4858, October 1998.

[75] Eric Bertin, Michel Droz, and Guillaume Grégoire. Boltzmann and hydrodynamic description for self-propelled particles. *Physical Review E*, 74(2):022101, August 2006.

[76] N. D. Mermin and H. Wagner. Absence of Ferromagnetism or Antiferromagnetism in One- or Two-Dimensional Isotropic Heisenberg Models. *Physical Review Letters*, 17(22):1133–1136, November 1966.

[77] Kenneth G. Wilson. The renormalization group: Critical phenomena and the Kondo problem. *Reviews of Modern Physics*, 47(4):773–840, October 1975.

[78] Michael E. Fisher. Renormalization group theory: Its basis and formulation in statistical physics. *Reviews of Modern Physics*, 70(2):653–681, April 1998.

[79] Efi Efrati, Zhe Wang, Amy Kolan, and Leo P. Kadanoff. Real-space renormalization in statistical mechanics. *Reviews of Modern Physics*, 86(2):647–667, May 2014.

[80] Tamás Vicsek and Anna Zafeiris. Collective motion. *Physics Reports*, 517(3-4):71–140, August 2012.

[81] Michael E. Cates. Active Field Theories. April 2019.

[82] John Toner, Yuhai Tu, and Sriram Ramaswamy. Hydrodynamics and phases of flocks. *Annals of Physics*, 318(1):170–244, July 2005.

[83] Sriram Ramaswamy. The Mechanics and Statistics of Active Matter. *Annual Review of Condensed Matter Physics*, 1(1):323–345, July 2010.

[84] Sriram Ramaswamy. Active matter. *Journal of Statistical Mechanics: Theory and Experiment*, 2017(5):054002, May 2017.

[85] Gerhard Gompper, Roland G. Winkler, Thomas Speck, Alexandre Solon, Cesare Nardini, Fernando Peruani, Hartmut Loewen, Ramin Golestanian, U. Benjamin Kaupp, Luis Alvarez, Thomas Kioerboe, Eric Lauga, Wilson Poon, Antonio De Simone, Frank Cichos, Alexander Fischer, Santiago Muinos Landin, Nicola Soeker, Raymond Kapral, Pierre Gaspard, Marisol Ripoll, Francesc Sagues, Julia Yeomans, Amin Doostmohammadi, Igor Aronson, Clemens Bechinger, Holger Stark, Charlotte Hemelrijk, Francois Nedelec, Trinish Sarkar, Thibault Aryaksama, Mathilde Lacroix, Guillaume Duclos, Victor Yashunsky, Pascal Silberzan, Marino Arroyo, and Sohan Kale. The 2019 Motile Active Matter Roadmap. *arXiv:1912.06710 [cond-mat, physics:physics]*, December 2019.

[86] Gabriel S. Redner, Michael F. Hagan, and Aparna Baskaran. Structure and dynamics of a phase-separating active colloidal fluid. *Physical Review Letters*, 110(5):1–5, 2013.

[87] Michael E. Cates and Julien Tailleur. Motility-Induced Phase Separation. *Annual Review of Condensed Matter Physics*, 6(1):219–244, 2015.

[88] Benno Liebchen and Hartmut Löwen. Synthetic Chemotaxis and Collective Behavior in Active Matter. *Accounts of Chemical Research*, 51(12):2982–2990, December 2018.

[89] J Prost, Frank Jülicher, and J-f Joanny. Active gel physics. *Nature physics*, 11(February):131–139, 2015.

[90] Wang Xi, Thuan Beng Saw, Delphine Delacour, Chwee Teck Lim, and Benoit Ladoux. Material approaches to active tissue mechanics. *Nature Reviews Materials*, 4(1):23–44, January 2019.

[91] Xavier Trepat and Erik Sahai. Mesoscale physical principles of collective cell organization. *Nature Physics*, 14(7):671–682, July 2018.

[92] Daniel Needleman and Zvonimir Dogic. Active matter at the interface between materials science and cell biology. *Nature Reviews Materials*, 2(9):17048, September 2017.

[93] Amin Doostmohammadi, Jordi Ignés-Mullol, Julia M. Yeomans, and Francesc Sagués. Active nematics. *Nature Communications*, 9(1):3246, December 2018.

[94] J.-C. Tsai, Fangfu Ye, Juan Rodriguez, J. P. Gollub, and T. C. Lubensky. A Chiral Granular Gas. *Physical Review Letters*, 94(21):214301, May 2005.

[95] Benjamin C. van Zuiden, Jayson Paulose, William T. M. Irvine, Denis Bartolo, and Vincenzo Vitelli. Spatiotemporal order and emergent edge currents in active spinner materials. *Proceedings of the National Academy of Sciences*, 113(46):12919–12924, November 2016.

[96] Nguyen H. P. Nguyen, Daphne Klotsa, Michael Engel, and Sharon C. Glotzer. Emergent Collective Phenomena in a Mixture of Hard Shapes through Active Rotation. *Physical Review Letters*, 112(7):075701, February 2014.

[97] J. S. Dahler and L. E. Scriven. Angular Momentum of Continua. *Nature*, 192(4797):36, October 1961.

[98] Debarghya Banerjee, Anton Souslov, Alexander G. Abanov, and Vincenzo Vitelli. Odd viscosity in chiral active fluids. *Nature Communications*, 8(1):1–12, November 2017.

[99] J. E. Avron. Odd Viscosity. *Journal of Statistical Physics*, 92(3):543–557, August 1998.

[100] Vishal Soni, Ephraim S. Bililign, Sofia Magkiriadou, Stefano Sacanna, Denis Bartolo, Michael J. Shelley, and William T. M. Irvine. The odd free surface flows of a colloidal chiral fluid. *Nature Physics*, 15(11):1188–1194, November 2019.

[101] Kinjal Dasbiswas, Kranthi K. Mandadapu, and Suriyanarayanan Vaikuntanathan. Topological localization in out-of-equilibrium dissipative systems. *Proceedings of the National Academy of Sciences*, 115(39):E9031–E9040, September 2018.

[102] Anton Souslov, Kinjal Dasbiswas, Michel Fruchart, Suriyanarayanan Vaikuntanathan, and Vincenzo Vitelli. Topological Waves in Fluids with Odd Viscosity. *Physical Review Letters*, 122(12):128001, March 2019. [and see references therein].

[103] Katherine Klymko, Dibyendu Mandal, and Kranthi K. Mandadapu. Statistical mechanics of transport processes in active fluids: Equations of hydrodynamics. *The Journal of Chemical Physics*, 147(19):194109, November 2017.

[104] Jeffrey M. Epstein and Kranthi K. Mandadapu. Time reversal symmetry breaking in two-dimensional non-equilibrium viscous fluids. July 2019.

[105] J. H. Irving and John G. Kirkwood. The Statistical Mechanical Theory of Transport Processes. IV. The Equations of Hydrodynamics. *The Journal of Chemical Physics*, 18(6):817–829, June 1950.

[106] Zhenghan Liao, William T. M. Irvine, and Suriyanarayanan Vaikuntanathan. Rectification of energy and motion in non-equilibrium parity violating metamaterials. *arXiv:1907.05938 [cond-mat]*, July 2019.

[107] Udo Seifert. Stochastic thermodynamics, fluctuation theorems and molecular machines. *Reports on Progress in Physics. Physical Society (Great Britain)*, 75(12):126001, December 2012.

[108] Ali Coskun, Michal Banaszak, R. Dean Astumian, J. Fraser Stoddart, and Bartosz A. Grzybowski. Great expectations: Can artificial molecular machines deliver on their promise? *Chemical Society Reviews*, 41(1):19–30, December 2011.

[109] Ignacio A. Martínez, Édgar Roldán, Luis Dinis, and Raúl A. Rica. Colloidal heat engines: A review. *Soft Matter*, 13(1):22–36, 2017.

[110] Benedikt Sabass. Fluctuating, Lorentz-force-like coupling of Langevin equations and heat flux rectification. *Physical Review E*, 96(2):022109, August 2017.

[111] Francis G. Woodhouse, Henrik Ronellenfitsch, and Jörn Dunkel. Autonomous Actuation of Zero Modes in Mechanical Networks Far from Equilibrium. *Physical Review Letters*, 121(17):178001, October 2018.

[112] Lisa M. Nash, Dustin Kleckner, Alismari Read, Vincenzo Vitelli, Ari M. Turner, and William T. M. Irvine. Topological mechanics of gyroscopic metamaterials. *Proceedings of the National Academy of Sciences*, 112(47):14495–14500, November 2015.

[113] Roman Süsstrunk and Sebastian D. Huber. Classification of topological phonons in linear mechanical metamaterials. *Proceedings of the National Academy of Sciences*, 113(33):E4767–E4775, August 2016.

[114] Noah P. Mitchell, Lisa M. Nash, Daniel Hexner, Ari M. Turner, and William T. M. Irvine. Amorphous topological insulators constructed from random point sets. *Nature Physics*, 14(4):380–385, April 2018.

[115] Ching Hua Lee, Guangjie Li, Guliuxin Jin, Yuhan Liu, and Xiao Zhang. Topological dynamics of gyroscopic and Floquet lattices from Newton's laws. *Physical Review B*, 97(8):085110, February 2018.

[116] Ken Sekimoto. Langevin Equation and Thermodynamics. *Progress of Theoretical Physics Supplement*, 130:17–27, January 1998.

[117] Crispin Gardiner. The Ito Calculus and Stochastic Differential Equations. In *Stochastic Methods*, chapter 4, page 107. Springer-Verlag Berlin Heidelberg, 4 edition, 2009.

[118] Michele Ceriotti, Giovanni Bussi, and Michele Parrinello. Colored-Noise Thermostats à la Carte. *Journal of Chemical Theory and Computation*, 6(4):1170–1180, April 2010.

[119] Anupam Kundu, Sanjib Sabhapandit, and Abhishek Dhar. Large deviations of heat flow in harmonic chains. *Journal of Statistical Mechanics: Theory and Experiment*, 2011(03):P03007, March 2011.

[120] Takahiro Harada and Shin-ichi Sasa. Equality Connecting Energy Dissipation with a Violation of the Fluctuation-Response Relation. *Physical Review Letters*, 95(13):130602, September 2005.

[121] P. Pradhan and U. Seifert. Nonexistence of classical diamagnetism and nonequilibrium fluctuation theorems for charged particles on a curved surface. *EPL (Europhysics Letters)*, 89(3):37001, February 2010.

[122] Geoffrey Ingram Taylor. Analysis of the swimming of microscopic organisms. *Proceedings of the Royal Society of London. Series A. Mathematical and Physical Sciences*, 209(1099):447–461, November 1951.

[123] E. M. Purcell. Life at low Reynolds number. *American Journal of Physics*, 45(1):3–11, January 1977.

[124] Ramin Golestanian and Armand Ajdari. Analytic results for the three-sphere swimmer at low Reynolds number. *Physical Review E*, 77(3):036308, March 2008.

[125] R. Golestanian. Three-sphere low-Reynolds-number swimmer with a cargo container. *The European Physical Journal E*, 25(1):1–4, January 2008.

[126] Ramin Golestanian and Armand Ajdari. Stochastic low Reynolds number swimmers. *Journal of Physics: Condensed Matter*, 21(20):204104, April 2009.

[127] Marco Leoni, Jurij Kotar, Bruno Bassetti, Pietro Cicuta, and Marco Cosentino Lagomarsino. A basic swimmer at low Reynolds number. *Soft Matter*, 5(2):472–476, January 2009.

[128] H. Kählert, J. Carstensen, M. Bonitz, H. Löwen, F. Greiner, and A. Piel. Magnetizing a Complex Plasma without a Magnetic Field. *Physical Review Letters*, 109(15):155003, October 2012.

[129] P. C. Martin, E. D. Siggia, and H. A. Rose. Statistical Dynamics of Classical Systems. *Physical Review A*, 8(1):423–437, July 1973.

[130] Hans-Karl Janssen. On a Lagrangean for classical field dynamics and renormalization group calculations of dynamical critical properties. *Zeitschrift für Physik B Condensed Matter*, 23(4):377–380, December 1976.

[131] C. De Dominicis and L. Peliti. Field-theory renormalization and critical dynamics above ${T}_{c}$: Helium, antiferromagnets, and liquid-gas systems. *Physical Review B*, 18(1):353–376, July 1978.

[132] Ken Sekimoto. Kinetic Characterization of Heat Bath and the Energetics of Thermal Ratchet Models. *Journal of the Physics Society Japan*, 66(5):1234–1237, 1997.

[133] Jie Ren, Peter Hänggi, and Baowen Li. Berry-Phase-Induced Heat Pumping and Its Impact on the Fluctuation Theorem. *Physical Review Letters*, 104(17):170601, April 2010.

[134] Peter Jung. Periodically driven stochastic systems. *Physics Reports*, 234(4):175–295, November 1993.

[135] Takashi Oka and Sota Kitamura. Floquet Engineering of Quantum Materials. *Annual Review of Condensed Matter Physics*, 10(1):387–408, March 2019.

[136] Sho Higashikawa, Hiroyuki Fujita, and Masahiro Sato. Floquet engineering of classical systems. pages 1–20, 2018.

[137] G. C. Wick. The Evaluation of the Collision Matrix. *Physical Review*, 80(2):268–272, October 1950.

[138] Zhenghan Liao, Ming Han, Michel Fruchart, Vincenzo Vitelli, and Suriyanarayanan Vaikuntanathan. A mechanism for anomalous transport in chiral active liquids. *The Journal of Chemical Physics*, 151(19):194108, November 2019.

[139] M. Cristina Marchetti, Yaouen Fily, Silke Henkes, Adam Patch, and David Yllanes. Minimal model of active colloids highlights the role of mechanical interactions in controlling the emergent behavior of active matter. *Current Opinion in Colloid & Interface Science*, 21:34–43, February 2016.

[140] S. Fürthauer, M. Strempel, S. W. Grill, and F. Jülicher. Active chiral fluids. *The European Physical Journal E*, 35(9):89, September 2012.

[141] Frank Jülicher, Stephan W. Grill, and Guillaume Salbreux. Hydrodynamic theory of active matter. *Reports on Progress in Physics*, 81(7):076601, June 2018.

[142] Christian Scholz, Michael Engel, and Thorsten Pöschel. Rotating robots move collectively and self-organize. *Nature Communications*, 9(1):931, March 2018.

[143] Alexey Snezhko. Complex collective dynamics of active torque-driven colloids at interfaces. *Current Opinion in Colloid & Interface Science*, 21:65–75, February 2016.

[144] Jing Yan, Ming Han, Jie Zhang, Cong Xu, Erik Luijten, and Steve Granick. Reconfiguring active particles by electrostatic imbalance. *Nature Materials*, 15(10):1095–1099, October 2016.

[145] Antoine Aubret, Mena Youssef, Stefano Sacanna, and Jérémie Palacci. Targeted assembly and synchronization of self-spinning microgears. *Nature Physics*, 14(11):1114, November 2018.

[146] Ananyo Maitra and Martin Lenz. Spontaneous rotation can stabilise ordered chiral active fluids. *Nature Communications*, 10(1):920, February 2019.

[147] Sydney Chapman, T. G. Cowling, and D. Burnett. *The Mathematical Theory of Non-Uniform Gases: An Account of the Kinetic Theory of Viscosity, Thermal Conduction and Diffusion in Gases*. Cambridge University Press, 1990.

[148] John G. Kirkwood. The Statistical Mechanical Theory of Transport Processes I. General Theory. *The Journal of Chemical Physics*, 14(3):180–201, March 1946.

[149] John G. Kirkwood, Frank P. Buff, and Melvin S. Green. The Statistical Mechanical Theory of Transport Processes. III. The Coefficients of Shear and Bulk Viscosity of Liquids. *The Journal of Chemical Physics*, 17(10):988–994, October 1949.

[150] John S. Dahler. Transport Phenomena in a Fluid Composed of Diatomic Molecules. *The Journal of Chemical Physics*, 30(6):1447–1475, June 1959.

[151] Denis J. Evans. On the generalized hydrodynamics of polyatomic fluids. *Molecular Physics*, 32(4):1171–1176, October 1976.

[152] Denis J. Evans and William B. Streett. Transport properties of homonuclear diatomics. *Molecular Physics*, 36(1):161–176, July 1978.

[153] Stephen G. Brush. Theories of Liquid Viscosity. *Chemical Reviews*, 62(6):513–548, December 1962.

[154] Schofield P., Henderson James R., and Rowlinson John Shipley. Statistical mechanics of inhomogeneous fluids. *Proceedings of the Royal Society of London. A. Mathematical and Physical Sciences*, 379(1776):231–246, January 1982.

[155] Eligiusz Wajnryb, Andrzej R. Altenberger, and John S. Dahler. Uniqueness of the microscopic stress tensor. *The Journal of Chemical Physics*, 103(22):9782–9787, December 1995.

[156] Isaac Goldhirsch. Stress, stress asymmetry and couple stress: From discrete particles to continuous fields. *Granular Matter*, 12(3):239–252, May 2010.

[157] Nikhil Chandra Admal and E. B. Tadmor. A Unified Interpretation of Stress in Molecular Systems. *Journal of Elasticity*, 100(1):63–143, June 2010.

[158] Noel A. Clark and Bruce J. Ackerson. Observation of the Coupling of Concentration Fluctuations to Steady-State Shear Flow. *Physical Review Letters*, 44(15):1005–1008, April 1980.

[159] Siegfried Hess. Shear-flow-induced distortion of the pair-correlation function. *Physical Review A*, 22(6):2844–2848, December 1980.

[160] S. Hess and H. J. M. Hanley. Distortion of the structure of a simple fluid. *Physical Review A*, 25(3):1801–1804, March 1982.

[161] H. J. M. Hanley, J. C. Rainwater, and S. Hess. Shear-induced angular dependence of the liquid pair correlation function. *Physical Review A*, 36(4):1795–1802, August 1987.

[162] Colin Scheibner, Anton Souslov, Debarghya Banerjee, Piotr Surowka, William T. M. Irvine, and Vincenzo Vitelli. Odd elasticity. February 2019.

[163] Anton Souslov, Andrey Gromov, and Vincenzo Vitelli. Anisotropic odd viscosity via time-modulated drive. September 2019.

[164] Steve Plimpton. Fast Parallel Algorithms for Short-Range Molecular Dynamics. *Journal of Computational Physics*, 117(1):1–19, March 1995.

[165] Andrew I. Jewett, Zhuoyun Zhuang, and Joan-Emma Shea. Moltemplate a Coarse-Grained Model Assembly Tool. *Biophysical Journal*, 104(2, Supplement 1):169a, January 2013.

[166] Francis G. Woodhouse, Aden Forrow, Joanna B. Fawcett, and Jörn Dunkel. Stochastic cycle selection in active flow networks. *Proceedings of the National Academy of Sciences*, 113(29):8200–8205, July 2016.

[167] Francis G. Woodhouse and Jörn Dunkel. Active matter logic for autonomous microfluidics. *Nature Communications*, 8(1):1–7, April 2017.

[168] Francis G. Woodhouse, Joanna B. Fawcett, and Jörn Dunkel. Information transmission and signal permutation in active flow networks. *New Journal of Physics*, 20(3):035003, March 2018.

[169] Mathematica, Version 11.3. Wolfram Research, Inc., 2018.

[170] Hyun Keun Lee, Sourabh Lahiri, and Hyunggyu Park. Nonequilibrium steady states in Langevin thermal systems. *Physical Review E*, 96(2):022134, 2017.

[171] Hyun-Myung Chun and Jae Dong Noh. Microscopic theory for the time irreversibility and the entropy production. *Journal of Statistical Mechanics: Theory and Experiment*, 2018(2):023208, February 2018.

[172] Suraj Shankar and M. Cristina Marchetti. Hidden entropy production and work fluctuations in an ideal active gas. *Physical Review E*, 98(2):020604, August 2018.

[173] Lorenzo Caprini, Umberto Marini Bettolo Marconi, Andrea Puglisi, and Angelo Vulpiani. The entropy production of Ornstein–Uhlenbeck active particles: A path integral method for correlations. *Journal of Statistical Mechanics: Theory and Experiment*, 2019(5):053203, May 2019.

[174] L. Onsager and S. Machlup. Fluctuations and Irreversible Processes. *Physical Review*, 91(6):1505–1512, September 1953.

[175] M. Tuckerman, B. J. Berne, and G. J. Martyna. Reversible multiple time scale molecular dynamics. *The Journal of Chemical Physics*, 97(3):1990–2001, August 1992.

[176] Giovanni Bussi and Michele Parrinello. Accurate sampling using Langevin dynamics. *Physical Review E*, 75(5):056707, May 2007.

[177] Siu A. Chin. Symplectic and energy-conserving algorithms for solving magnetic field trajectories. *Physical Review E*, 77(6):066401, June 2008.

[178] Hyun-Myung Chun, Xavier Durang, and Jae Dong Noh. Emergence of nonwhite noise in Langevin dynamics with magnetic Lorentz force. *Physical Review E*, 97(3):032117, March 2018.